

METHODS FOR DESIGN, METROLOGY, AND ALIGNMENT
OF SCALABLE LARGE OPTICAL SYSTEMS

by

Joel David Berkson

Copyright © Joel David Berkson 2023

A Dissertation Submitted to the Faculty of the
JAMES C WYANT COLLEGE OF OPTICAL SCIENCES

In Partial Fulfillment of the Requirements
For the Degree of

DOCTOR OF PHILOSOPHY
WITH A MAJOR IN OPTICAL SCIENCES

In the Graduate College

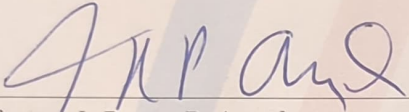
THE UNIVERSITY OF ARIZONA

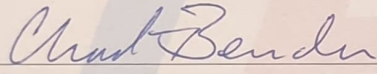
2023

THE UNIVERSITY OF ARIZONA
GRADUATE COLLEGE

As members of the Dissertation Committee, we certify that we have read the dissertation prepared by **Joel David Berkson**, titled *Methods for Design, Metrology, and Alignment of Scalable Large Optical Systems* and recommend that it be accepted as fulfilling the dissertation requirement for the Degree of Doctor of Philosophy.


Date: Jan 8th, 2024
Professor Daewook Kim


Date: Jan 8th 2024
Professor J. Roger P. Angel


Date: Jan 4, 2024
Professor Chad Bender

Final approval and acceptance of this dissertation is contingent upon the candidate's submission of the final copies of the dissertation to the Graduate College.

I hereby certify that I have read this dissertation prepared under my direction and recommend that it be accepted as fulfilling the dissertation requirement.


Date: Jan 8th, 2024
Professor Daewook Kim
Dissertation Committee Co-Chair
Wyant College of Optical Sciences

ACKNOWLEDGEMENTS

There are so many people I would like to thank in my life and education. First and foremost, I would like to thank my family, Mom, Dad, Kacie and Barrie, for always supporting me in whatever I want to do. I'd also like to thank my partner and love Paulina for all of her support, and our dog Banjo and cat Levi.

The support system at the University of Arizona has been unmatched for me. Daewook has been my advisor for the better part of 7 years now, from undergraduate studies through now. It all started with a project he gave me in 2016 to design a 3D printed telescope for attachment to an iPhone. I had no idea how a telescope even worked at the time, but he had so much patience. I'd like to sincerely thank him for always making sure I had an interesting project to work on all these years. I'd also like to thank Roger Angel. Roger found me in the hallway of Steward Observatory in 2021. Without knowing who he was or who I was he asked me: "Do you know how to use Zemax?" Ultimately this turned into the design of the LFAST unit telescope (Chapter 2 of this dissertation), and we worked together on a number of interesting projects related to astronomy and solar energy, many not including in this dissertation. I'd like to thank Roger for teaching me the importance of 'napkin' calculations to check for feasibility. I'd like to thank Chad Bender. While working on telescope projects, one thing I was always missing was an understanding of astronomy and instrumentation. Chad was always willing to educate me on these topics, so that I could be more effective in my work. I thank him for being a very supportive mentor. I'd like to thank Justin Hyatt. Justin leads the thermoforming group. Being placed on that project led to Chapters 3 and 4 of this dissertation. I'd like to thank Justin for giving me the funding to try lots of different metrology systems to solve the problem, and he continued to do so even when some methods failed. I am also very grateful to Tech Launch Arizona and the McGuire Center for Entrepreneurship. Without them, I would not be pursuing entrepreneurship upon graduation. I'd like to to sincerely thank everyone involved in those programs for their tireless efforts to support entrepreneurship within the university community, and for helping me navigate technology licensing and business plans.

I'd like to thank both the business and academic offices at the College of Optical Sciences and Steward Observatory. These are amazing people that have helped me get through this program at every step of the way. I'd like to especially thank the Steward Observatory Business Office for handling all of my travel documents from participating in the NSF I-Corps program. There are countless other friends, colleagues, and mentors that I cannot explicitly name in these short acknowledgements, but I'd like to thank anyone that I have interacted with since my studies began in optical sciences. Lastly, I'd like to thank the National Science Foundation and the

Schmidt Foundation for their funding support for all of this work.

DEDICATION

To the relentless exploration of knowledge, with the understanding that learning is the key to unlocking new horizons and finding creative and practical solutions to the world's ever-evolving challenges.

TABLE OF CONTENTS

LIST OF FIGURES	9
LIST OF TABLES	16
ABSTRACT	17
CHAPTER 1 Introduction	18
CHAPTER 2 Large Fiber Array Spectroscopic Telescope: Optical Design for a Scalable Unit Telescope	27
2.1 Background	27
2.1.1 Why we want larger telescopes and why we can not build them.	27
2.1.2 A larger collecting area without building a larger telescope: The Large Fiber Array Spectroscopic Telescope	28
2.2 Requirements for each unit telescope	30
2.3 Optical Design	33
2.3.1 Primary Mirror	33
2.3.2 Prime Focus Corrector	36
2.3.3 Atmospheric Compensation	38
2.3.4 Atmospheric jitter compensation	41
2.3.5 Fiber feed and relay optics	42
2.4 Tolerancing	43
2.4.1 Prime Focus Corrector	44
2.4.2 Primary Mirror	47
2.4.3 Testing	49
2.5 Results from first unit telescope testing	51
2.5.1 30" Mirror	51
2.5.2 PFC Mechanical Design and Alignment	53
2.5.3 Unit Telescope Frame and Azimuth/Elevation Drive	54
2.5.4 On-Sky Testing	56
CHAPTER 3 Binocular Fringe Projection Profilometry for Metrology of Meter- Scale Optical Surfaces	58
3.1 Motivation	58
3.2 Technical Background	62
3.2.1 Stereo Vision	62

TABLE OF CONTENTS – *Continued*

3.2.2	Fringe Projection Profilometry	63
3.2.3	Stereo Camera FPP	64
3.3	Binocular FPP with sub-pixel phase matching	66
3.3.1	Subpixel Matching Process	66
3.3.2	Calibration	69
3.3.3	Data Acquisition and Processing	71
3.4	Demonstrations	71
3.4.1	Flatness Accuracy	71
3.4.2	Highly Specular Machined Surfaces	73
3.4.3	Laser Tracker Comparison to LFAST mold	75
3.4.4	Large-Scale Surfaces	76
3.4.5	Repeatability	78
3.5	Discussion	79
3.6	Comments on limitations and paths for future developments	81
3.6.1	Calibration	81
3.6.2	Measurement Speed	82
3.6.3	Robustness to the environment	83
3.6.4	Summary	83
CHAPTER 4 Systematic Radio Telescope Alignment using Portable Fringe Projection Profilometry 85		
4.1	Motivation	85
4.2	Other methods for dish alignment	86
4.3	Methods	88
4.3.1	Binocular Fringe Projection Profilometry with Hierarchical Unwrapping	88
4.3.2	Dish Measurement with Global Reference Frame	89
4.4	Experimental Setup, Calibration, and Configuration	92
4.4.1	Hardware	92
4.4.2	Calibration	93
4.4.3	Measurement Setup	93
4.5	Results	95
4.6	Discussions and Future Work	100
CHAPTER 5 Concluding Remarks 102		
APPENDIX A Large Fiber Array Spectroscopic Telescope: Optical Design for a Scalable Unit Telescope 105		

TABLE OF CONTENTS – *Continued*

APPENDIX B Binocular fringe projection profilometry for the metrology of meter-scale optical surfaces	116
APPENDIX C Systematic Radio Telescope Alignment using Portable Fringe Projection Profilometry	132

LIST OF FIGURES

1.1	Cost versus aperture for a variety of large telescopes. Van Belle covered all telescopes pre-2004, and found that the trend was $D \propto 2.45$ post-1980 versus $D \propto 2.77$ pre-1980, showing a slight improvement over time. GMT, TMT, and E-ELT appear to be on a similar trend or slightly better.	19
1.2	Black hole images released by EHT in 2019. The diameter of the colorized donut is roughly $50 \mu\text{as}$. It is formed with a combination of 8 radio telescopes around the globe.	21
1.3	Plotting the percent gain dictated by the Ruze Equation as a function of surface RMS to wavelength ratio. At $\lambda/15$, 3 dB loss, or 50%, is achieved.	22
1.4	Shown on the left is the concept for a flexible mold; a surface with linear actuators that control the position of tiles that are interconnected with springs. Shown on the right is the actual implementation of the flexible mold surface.	24
2.1	Rendering of 20-unit telescopes mounted on a single alt-az bearing. An array of 132 of these is equivalent in collecting area to E-ELT. . .	29
2.2	Requirements for an LFAST unit telescope.	31
2.3	The paraxial model here is shown with a ± 4 arcminute field. The guide camera needs a significantly larger FOV than at the fiber in order to ensure that there will be stars with enough brightness to guide with. The chosen field gives a 97% chance of at least one 16th magnitude star in the field of view, which we found can be captured with a signal to noise ratio of ~ 30 with a 10 second exposure[1, 2]. .	32
2.4	2D optical layout of the final designed unit telescope for the 20-unit prototype (top). Zoomed in view of the 2D layout of the prime focus corrector assembly, including corrector lenses, fiber puck, relay system, and guide camera (bottom).	34
2.5	Optical prescription for each unit telescope in the first 20-unit LFAST telescope.	35

LIST OF FIGURES – *Continued*

2.6	Conceptual design to create high quality images on-axis, for two-octaves of bandpass. If the optimizer is weighted toward the on-axis field, diffraction limited imaging is achieved in the vicinity of the on-axis field, and degrades for the rest of the field. Black circle in the spot diagrams is the airy disk for $1.1 \mu\text{m}$ wavelength. Alternatively, the imaging performance can be balanced if weighted equally. While this simple telescope design works in theory, the addition of atmospheric dispersion compensation and better performance near the on-axis field is needed for the as-built telescope.	37
2.7	RMS spot size at the fiber image plane as a function of field position. Diffraction limit is shown for 900 nm. The telescope is diffraction limited at this wavelength up to ~ 0.03 degrees.	39
2.8	Optimization of L4 decenter to correct for atmospheric dispersion. Upper left shows the primary atmospheric dispersion (for 400-1700 nm) as a function of elevation and induced primary dispersion from L4 as a function of decenter. These curves can be mapped to the required L4 decenter to correct for primary atmospheric dispersion as a function of elevation angle (bottom left). The decenter required to correct for primary atmospheric dispersion correction, however, does not produce the best encircled energy, thus a numerical analysis was performed to find the optimal L4 decenter as a function of elevation (right).	41
2.9	Spot diagram at the lowest elevation uncorrected (left) and corrected with L4 lateral translation (right). The corrected focus is shown after recentering the image on the fiber using tilt of the primary mirror. Also shown is the $18 \mu\text{m}$ fiber core in gray.	42
2.10	Simulated images of the 'black hole' at the guide camera due to the fiber. Shown is the off-axis image, and image given 0.2 arcseconds of image motion.	43
2.11	Polychromatic PSFs for 3 field points at the guide camera image plane. All field points are better than 1 arcsecond FWHM.	44
2.12	Sensitivity curves and best fit lines shown for decenter and tilt of each corrector lens. Sensitivity values are shown as $\mu\text{m}/\text{mm}$ for decenter or $\mu\text{m}/\text{deg}$ for tilt. These values indicate the increase in radius to 80% encircled energy per unit perturbation.	45

LIST OF FIGURES – *Continued*

2.13	Final tolerances for the prime focus corrector (a). L1 and L3 have slightly more sensitivity than L2 and L4, thus the decenter tolerance is tighter for L1 and L3. Irregularity, wedge, radius error, center thickness, and material properties are all within standard tolerances for a variety of manufacturers. Mechanical tolerances are within achievable tolerances for a lens barrel. The yield curve and histogram (b) are shown for 2640 Monte Carlo trials using these tolerances with uniform statistics. The average performance is 84.2% encircled energy, and the number of telescopes is shown in 2.5% bin widths.	46
2.14	Point Spread Function as a function of seeing. Loss of encircled energy increases rapidly as the FWHM approaches the fiber diameter.	48
2.15	Structure function requirement for LFAST. 1 arcsec is the expected atmospheric seeing conditions, and 0.5 arcsec is the mirror requirement goal.	49
2.16	Null Lens, Prime Focus Corrector, and return mirror set up in a double-pass configuration. The returning beam has only 0.0033 waves of wavefront error.	50
2.17	Optical prescription for the null lens.	50
2.18	Precision polished steel mold (left), lifting the 32" BORO FLOAT® mirror into the oven (center), and the slumped glass blank on the mold surface in the oven (right).	52
2.19	Grinding station (left) and polishing station (right).	53
2.20	First LFAST primary mirror assembly.	54
2.21	Shown here is the CAD layout cross-section of the mechanical mounts for L1-L4 and the relay lenses (top). The barrel was centered on the lens centering station (bottom left), and the optics were stacked in order from L1 to L4 (bottom center). Final assembled L1-L4 is shown on the bottom right.	55
2.22	CAD drawing of the PFC barrel (left), the barrel attached to its mounting structure (center), and the final PFC barrel populated with the lens assembly with graduate student Sonja Choi and Dr. Andrew Monson. (right)	55
2.23	The final painted frame for the single unit telescope. It uses the same azimuth and elevation drives and the same pier that the 20-unit telescope will use.	56
2.24	Final unit telescope on-aky at the UArizona Tech Park.	57

LIST OF FIGURES – *Continued*

3.1	The concept of deflectometry, If the positions of a source, a camera, and a point on the unit under test is known, simple law of reflection can be applied to extract the surface slope at that point. Scanning the source to cover all points on the unit under test builds a slope maps of the surface, which can be integrated to reconstruct the surface depth map.	60
3.2	Actual implementation of infrared deflectometry. I used two nichrome ribbons on two separate encoded linear stages, one for X scanning and one for Y scanning. Current was allowed to flow through the nichrome ribbons as they were scanned using the linear stages, and a thermal camera was used to capture the reflected images.	61
3.3	Phase-shifted sinusoidal patterns encodes contours of equal phase. Only four steps are shown for simplicity. Using Eq. 3.3 produces the wrapped phase maps. The reliability sorting method by noncontinuous path[3] is used to unwrap the phase. The result is a continuous phase distribution. Using this phase shifted pattern in two orthogonal directions produces two phase distributions, which encodes every point with a unique phase pair combination.	65
3.4	Precision stereo matching process shown for the horizontal phase only, for simplicity. For each pixel on camera 1, the closest matching phase pixel on camera 2 is found. A local window around the closest match is made and interpolated, and a new closest match is found. Repeating this process converges on a best matched 'location' on the camera 2 detector to each pixel on camera 1. Actual algorithm uses vertical and horizontal phase pair. With the vertical direction included in the matching process, there is a small window where the best matched phase pair must exist.	67
3.5	Actual system layout of cameras, projector, computer and unit under test (UUT). Note the rough placement of the projector. The only requirement is that the projector completely covers the UUT with fringes. The measurement is only made by stereo matching, so only the cameras require a stable mounting scheme. This configuration produces an expected depth resolution of $80 \mu\text{m}$ assuming one pixel of disparity error, but we expect the interpolated phase matching method to significantly reduce this.	70
3.6	Layout of extrinsic parameters and calibration target locations (left) and their corresponding reprojection errors for each camera (right).	70

LIST OF FIGURES – *Continued*

3.7	Shown are images of the first phase step for horizontal and vertical fringes, seen from both cameras (top). Also shown is a masked image of just the granite surface, with the wrapped phase shown (bottom left) and the unwrapped phase (bottom right). Shown is only the wrapped and unwrapped phase for one fringe direction and for one camera, for simplicity.	72
3.8	Grade B granite surface flat (left) and the measured flat top surface (right). RMS fit error to a plane is $5.1 \mu\text{m}$	73
3.9	Image of hexagonal prototype panel (left), its measurement (middle) and 5th order XY polynomial residuals (right). After subtracting low order shape up to 5th order, errors due to surface machining and support structure are revealed.	74
3.10	Shown is a screenshot of the laser tracker measurement report. The black circle represents the outer boundary of the steel mold surface. The table in the top left shows a summary of the measurement results compared to the ideal 5.275 m radius sphere. The red and blue spikes show the measured points with the largest deviation from the ideal sphere, blue being too low and red being too high. Best fit radius reported was $R = 5.281 \text{ m}$. The blue and red spikes indicate astigmatism in the surface of about $0.007''$, or $175 \mu\text{m}$, peak to valley.	75
3.11	Measurements of 863.6 mm steel mold. Shown above is the original measurement (upper left), the sphere fit error (upper middle), the 2nd order XY polynomial fit error (upper right), and images of the measured surface (lower left), projected fringe pattern, and the support structure underneath the surface (lower right). After subtracting low order shape, the underlying rib structure is seen 'printing through' the surface.	76
3.12	Layout of measurement system for 1.8 x 1.8 m adjustable mold (left) and an image of the projected fringes on the surface (right). Camera baseline is 2 m, and distance to the surface is 2.5 m.	77
3.13	Example image used to mask camera images taken of the mold surface (top left) using a modulation threshold to identify pixels that are on the mold surface. 3D map of the raw data with 4.6 million measured points (top right) and a 3D map of the residual with the ideal shape subtracted. Bottom right image is a zoomed in view of the measurement to demonstrate the point density over each 25 x 25 mm square tile.	78
3.14	Residual surface error from a 5th order XY polynomial fit for each of the five measurements.	79

LIST OF FIGURES – *Continued*

3.15	Point-to-point RMS repeatability histograms shown for the panel residual (left), as well as for the best fit 5th order polynomial (right). Each value on the histogram is the RMS calculated for a single point across each of the five measurements.	79
4.1	3D rendering of the Student Radio Telescope. The telescope will be made up of 26, 500 mm x 500 mm panels, each with a different shape due to the off-axis paraboloid design.	87
4.2	Coordinate system and actuator layout for each panel. Once tip, tilt, and piston values are extracted, they need to be converted to actual numbers of rotations on the actuators.	91
4.3	Left, one of the two FLIR Blackfly USB3 cameras with 8 mm focal length lens. Center, both cameras mounted to 8020 aluminum extrusion, mounted to a tripod. Right, BenQ 1080P short-throw projector used in this experiment.	92
4.4	An example image from the 20-image set used to calibrate the intrinsic and extrinsic parameters of the stereo camera pair. The checkerboard was moved throughout the overlapping FOV in order to properly calibrate for radial distortion.	93
4.5	Layout of the telescope structure. Two fiducials are placed where the paraboloid vertex and focus should be using 8020 extrusions. An example panel 1 and panel 2 are installed on the telescope. They are the bottom two rows of the center column of panels.	95
4.6	Nighttime measurement setup. The projector is placed near the telescope and utilizes the short-throw to cover the entire dish. The tripod carrying both cameras is placed roughly 3 meters away from the dish and positioned such that the entire dish can be seen in the field of view of both cameras. Shown in the image is the 10-pixel period frequency projected onto the dish structure.	96
4.7	Images from each camera are masked to isolate the two panels being measured. The phase unwrapping process produces four images: horizontal and vertical phase for each camera. These maps are used to find matching object locations from pixels on camera 1 to locations on camera 2.	97

LIST OF FIGURES – *Continued*

4.8	Each FPP measurement results in a point cloud for each panel, and the relative location of both the vertex and the focus. Raw data is shown on the left. The triangulated 3D points are produced relative to the coordinate system defined by camera 1. Matrix rotations and translations are applied to the panel point clouds to align the optical axis with the z-axis, shown on the right. In this configuration, the panels can be directly compared to Eq. 4.8 to extract the residual error in the panels, as well as the rigid body alignment error.	98
4.9	Best fit planes for each panel, including piston.	98
4.10	In addition to finding the rigid body motion error of each panel, the system also has enough resolution to map the surface errors of each panel compared to their ideal shape. Shown here are the residual surface maps compared to the ideal paraboloid.	99
4.11	Four measurements were performed, with three adjustment iterations between each measurement. Left, is the tip and tilt of each panel improving across each iteration. Right shows the piston for each panel also improving. Panel 1 was fortunately close to the ideal piston position before an adjustment was performed.	100

LIST OF TABLES

4.1	Calibrated stereo camera parameters.	94
4.2	Results before the first adjustment iteration.	97
4.3	Final results after 3 adjustments.	100

ABSTRACT

Optics has been for 400 years one of the most impactful fields of science; starting with medicine and astronomy. Optical engineering challenges differ greatly across applications. Large optical systems are exponentially more costly and complex, especially when made in quantities of one. The future of astronomy demands more photons and higher resolution, thus even larger collecting area. Scalability is needed in order to keep costs low while still producing these large collecting areas to meet demand. This dissertation explores methods for advancing concepts that enable large optical systems to become scalable.

In Chapter 1, we discuss the problem of large optical systems: why they are needed, why that need is difficult to meet, and what concepts need to be implemented in order to solve some of those needs. The following chapters cover design, metrology, and alignment for large optical systems, with scalability in mind. The first work discusses optical design for the Large Fiber Array Spectroscopic Telescope (LFAST) in Chapter 2. At 30" diameter, this telescope is designed to be replicated thousands of times. Next, we discuss a novel metrology method to support efficient manufacturing of radio antenna panels in Chapter 3. Finally, we discuss using the same metrology method to form an accurate dish by rapidly aligning radio antenna panels in Chapter 4.

CHAPTER 1

Introduction

When it comes to large optical systems, the goal is clear: see things with better resolution, whether it be spectral, angular, depth or otherwise. At its simplest, angular resolution is based on the ability to discern two adjacent objects from each other. The theoretical limit of the resolution of an optical system is dependent on two variables: the wavelength and the diameter of the collecting area. Lord Rayleigh derived the relationship of these variables with angular resolution, coined the Rayleigh Resolution (Eq. 1.1) in the late 1800s. It is equal to the radius to the first zero in the Airy diffraction pattern for a circular aperture. If two objects are separated by this distance or more, then they can be reliably discerned by the optical system.

$$\theta \approx 1.22 \frac{\lambda}{D} \quad (1.1)$$

To see things with high angular resolution, it is also necessary for UV, visible, and IR telescopes to collect enough photons to reduce \sqrt{n} noise, whether it be a complementary metal-oxide semiconductor (CMOS) or charge coupled device (CCD) for ultra-violet (UV), optical, or infrared (IR). For antennas used in millimeter wave and radio frequencies (RF). These detectors have noise that is inherent to the sensors even in the presence of zero photons, known as dark noise. It is necessary to gather enough photons obtain a signal higher than the inherent noise of the detector to be confident that a true detection has been made. Dark noise can be significantly reduced by cooling detectors to near absolute zero, reducing the probability that an electron will gain enough thermal energy to escape and thus cause current to flow. This is an expensive and generally undesirable solution. The most direct ways to gain more sensitivity and angular resolution (as shown by Eq. 1.1) is to make a larger collecting area. Ideally, the cost of a telescope scales quadratically with aperture

diameter (linearly with collecting area). This has long been known to not be the case, especially for optical telescopes[4, 5]. Van Belle et. al. published a paper in 2004 the trend of telescope cost versus aperture diameter, and compared telescopes pre-1980 and post-1980. The paper found that cost scales with $D \propto 2.45$ post-1980 versus $D \propto 2.77$ pre-1980. Figure 1.1 shows the plot from van Belle’s paper, with the additions of the Giant Magellan Telescope (GMT), European Extremely Large Telescope (E-ELT), and Thirty-Meter Telescope (TMT) estimated costs, adjusted to 2004 dollars. These power laws are not fundamental limitations, simply observations of the trends of existing observatories over time.

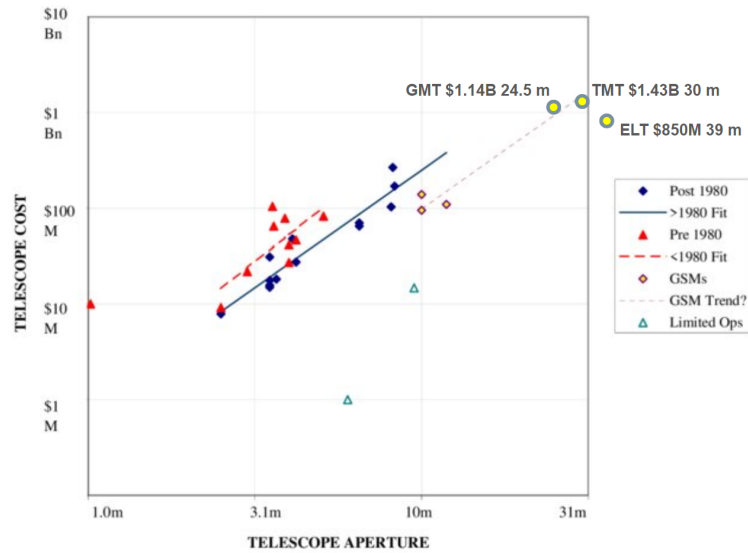


Figure 1.1: Cost versus aperture for a variety of large telescopes. Van Belle covered all telescopes pre-2004, and found that the trend was $D \propto 2.45$ post-1980 versus $D \propto 2.77$ pre-1980, showing a slight improvement over time. GMT, TMT, and E-ELT appear to be on a similar trend or slightly better.

To get to the even larger telescopes of the future, looking past GMT, TMT, and E-ELT, the cost could approach \$10B for only doubling the collecting area compared to these three near-future large telescopes. To break this paradigm, a significantly different approach to large telescopes is needed. Many of these new large telescopes are made with segmented primary mirrors. In order for the telescope to form direct

images of a celestial object, each segment of the telescope needs to be individually aligned and controlled to combine the image from each segment coherently. As the size of a telescope of this kind scales, the controls behind coherently aligning the segments get more and more complicated, continuing to follow the unsustainable cost versus aperture trend shown in Figure 1.1. For many astronomical research topics, like single object spectroscopy, direct imaging with a large aperture is unnecessary. Spectroscopy is inherently a photon deficient process, since light from a single object is spread across a large detector. This results in a need for either longer exposures or larger apertures in order to achieve high SNR. Transit spectroscopy is a method for determining the composition of an exoplanets atmosphere. Subtracting the spectrum of the host star with the spectrum of the host star during a transit (when the planet occluded the star), reveals the spectrum of the exoplanet atmosphere. Molecular absorption lines reveal molecular compositions of the atmosphere. In many cases, like transit spectroscopy, longer exposures are not an option, as the transit event happens for a limited period of time. If the only goal is to collect more photons, the paradigm of large telescopes can change. The Large Fiber Array Spectroscopic Telescope (LFAST) is a telescope concept based on thousands of small individual telescopes. Each telescope couples the light from a single star into an optical fiber similar to those used in fiber-optic communication. The outputs of the optical fibers from the individual telescopes are combined incoherently to form a slit-input for a spectrograph. In theory any number of telescopes can be used to form the slit. If economies of scale can be implemented to mass-produce the telescope at a low cost, collecting apertures much larger than the GMT, TMT, or E-ELT could be achieved for a fraction of the cost. Chapter 2 will describe in more detail the concept of LFAST, and how an optical design was created for mass production.

Optical telescopes are not the only kind of telescope aiming for mass manufacturing and deployment. In April of 2019, the Event Horizon Telescope (EHT) released the first image of a black hole (Figure 1.2) at the center of galaxy M87[6]. This image was formed by coherently combining many large radio telescopes across the globe to

create an effective aperture equivalent to the diameter of Earth. While an individual radio telescope would have angular resolution orders of magnitudes worse than an equivalent optical counterpart, the concept of radio astronomy can achieve angular resolutions far better than optical. Radio frequencies are slow enough that existing materials can respond to the speed of its alternating electromagnetic (EM) waves. This means that the amplitude and phase of a signal can be recorded and correlated with a different telescope at a later time. Looking back at Eq. 1.1, millimeter-wave telescopes are roughly 1000 times less resolved than an equivalently-sized optical telescope (λ), but the effective aperture (D) of the Earth is over 500,000 times larger than GMT, E-ELT, or TMT, which gives a net gain in angular resolution of about 500. For example, GMT is expected to have a 10 mas resolution, but EHT has a 20 μas resolution.

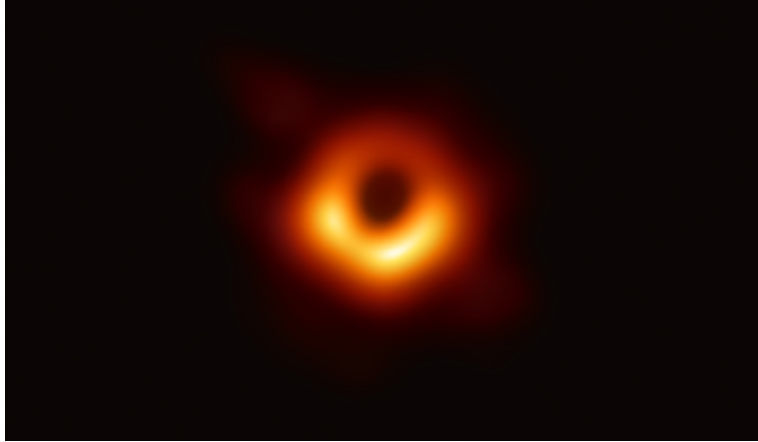


Figure 1.2: Black hole images released by EHT in 2019. The diameter of the colorized donut is roughly 50 μas . It is formed with a combination of 8 radio telescopes around the globe.

The ability to produce such images will greatly assist the understanding of gravity and fundamental physics. The future of astronomy demands the ability to view objects like this with higher angular resolution, higher sensitivity, and more often, to further accelerate these discoveries. The next-generation Very Large Array (ngVLA) and Square Kilometer Array (SKA) are two such projects to support these needs.

ngVLA involves 263 18-meter telescopes, and SKA plans for nearly 200 telescopes with varying sizes of 10-meters or greater. Radio telescopes have a more complicated cost versus aperture relationship than optical. They cover a much broader range of frequencies, covering many octaves, whereas even some of the most broadband optical/infrared telescopes only cover four octaves. The cost of a radio telescope highly depends on the wavelength. The gain of a radio telescope depends on the reflector surface accuracy relative to the wavelength being observed; the higher the frequency, the tighter the requirements on the primary reflector, and the more costly the telescope. The Ruze equation describes how the surface root-mean-square (RMS) error of a reflector affects the antenna gain, where G_0 is the nominal gain considering a perfect reflector, ϵ is the surface RMS and λ is the wavelength, expressed in the same physical units[7].

$$G(\epsilon) = G_0 e^{-\frac{4\pi\epsilon^2}{\lambda}} \quad (1.2)$$

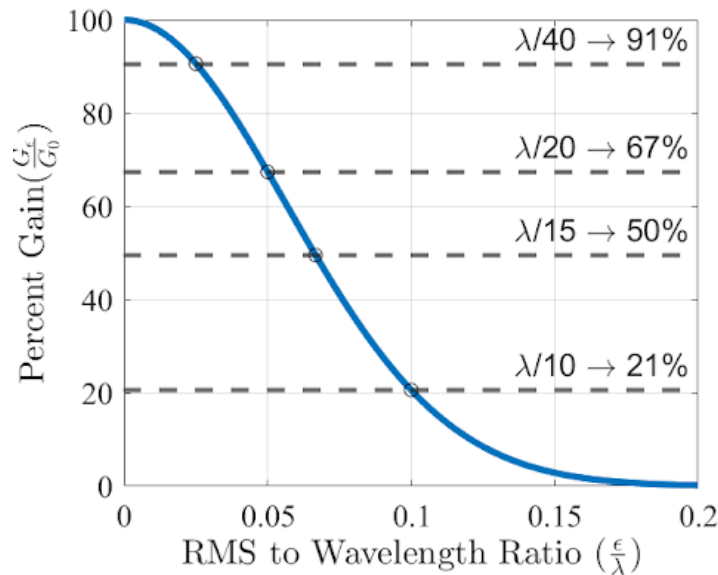


Figure 1.3: Plotting the percent gain dictated by the Ruze Equation as a function of surface RMS to wavelength ratio. At $\lambda/15$, 3 dB loss, or 50%, is achieved.

Just like large optical telescopes, radio telescope reflectors are commonly split

into smaller segments. The RMS value in the Ruze equation includes the error stack-up from the individual panel shape accuracy, gravity deformations, temperature gradients, wind-shake, and panel misalignment[8]. As the operating frequency increases (and the wavelength decreases), the sensitivity to all of these errors also increases. Gravity deformations, temperature gradients, and wind-shake are all related to unavoidable environmental conditions. They can be mitigated, but are not economical to actively control. Individual panel accuracy and alignment, however, can be improved in the manufacturing and assembly process, leaving more error budget for deformations due to these environmental conditions. For millimeter-wave astronomy, a general goal is $\lambda/25$ for individual panel accuracy. This places the required RMS of each panel at 40 microns for a 1 mm wavelength. While this is significantly easier to achieve than $\lambda/25$ for an optical telescope, these panels typically need to be made in mass quantities for arrays of radio telescopes like ngVLA, thus they need to be made with a low-cost, scalable manufacturing method. There are many common methods for making radio telescope panels: machining, electroforming, aluminum cassette, and carbon fiber reinforced plastic (CFRP)[8]. These methods all have varying limitations in speed, size, accuracy, and cost. Machining is slow and expensive due to tooling time. Electroforming, aluminum cassette, and CFRP all require a specific mold for each panel shape, which is expensive and time consuming to make. The Steward Observatory Solar Lab (SOSL) has been performing research to improve the process of another method: thermoforming[9]. The thermoforming process uses high temperatures to reduce the yield strength of a metal as a function of temperature, and performs a plastic deformation of the metal with a reduced force, similar to hot stamping[10]. Thermoforming also involves the use of a mold, but SOSL has been developing a mold that can change shape to accommodate a large range of panel geometries and curvatures, for use with both metal and glass (US Patent 10,538,451). Figure 1.4 shows one such mold; a 1/4" thick sheet of stainless steel that is cut by a water jet machine with a tile and blade flexure pattern to make it flexible. Tiles are controlled by linear actuators to set the vertical height, and the flexible mold surface conforms to the shape prescribed

by the linear actuators.

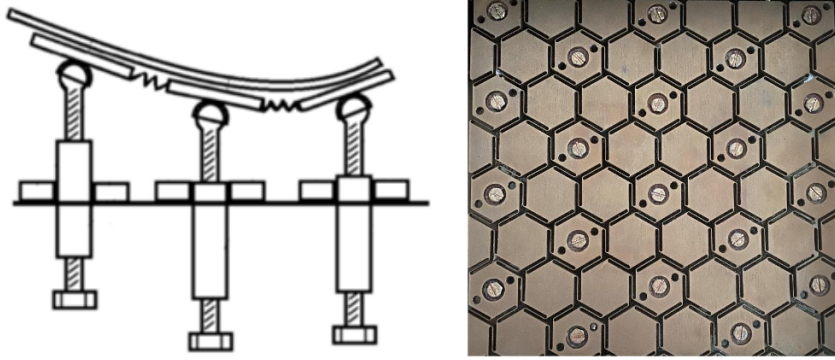


Figure 1.4: Shown on the left is the concept for a flexible mold; a surface with linear actuators that control the position of tiles that are interconnected with springs. Shown on the right is the actual implementation of the flexible mold surface.

The goal of this project is to make panels that meet the $\lambda/25$ for a 1 mm wavelength, or 40 μm RMS. Any specification requires a complimentary testing process in order to verify that it is being met. For a depth RMS error requirement with radio telescope panels, a metrology system that produces three dimensional (3D) data with a higher accuracy than the specification is required in order to compare a manufactured surface to an ideal shape. There are many metrology systems for optical surfaces that meet and far exceed this required accuracy (e.g. interferometers), but they only function with specular surfaces, and require unique components that depend on the surface shape and size that needs to be measured. Current measurement options for large antenna segments either require physical probing of the surface or measurement of the locations of physical fiducials. Coordinate Measuring Machines (CMM), laser trackers, and photogrammetry are all commonly used methods that are manual in nature with single point scanning and manual placement of fiducials. All of these panel metrology methods are time-consuming, limited in accuracy, expensive, and limited in spatial resolution. If a panel is measured with one of these methods and does not meet specifications, it is often unclear what is causing the error due to sparse spatial resolution of the measurement, leading to a

lack of feedback for the manufacturing method. This is especially true for the thermoforming method using a flexible mold in SOSL. The mold needs to be remeasured every time it is changed. Since the precision metal forming is a new technique, the team wanted a strong understand of the impacts of all manufacturing variables on both the mold and the resulting panels. Chapter 3 describes a method and system that has been implemented to rapidly measure both the mold and the panels with high accuracy and high spatial resolution using a combination of cameras and a digital projector. It has become a critical tool for the lab to make progress on this new thermoforming technique.

As mentioned previously, there are two ways that directly improve the performance of a radio telescope: the panel accuracy and the alignment accuracy. SOSL has been working on building panels more efficiently using the new thermoforming method, and as a demonstration the group has been aiming to use the panels to build a 3-meter radio telescope. Any radio telescope needs a metrology method to align the panels to form a continuous dish, and the lab needed a way to measure and align the demonstration telescope. Common methods to measure panel alignment and shape have historically included photogrammetry[11, 12, 13, 14], holography[15, 16, 17, 18] and laser trackers or laser trusses[13, 19, 20, 21]. Oftentimes, a combination of methods is used[13, 22, 23, 24]. All methods deliver the information on the surface accuracy of a dish, but they have many fundamental limitations and drawbacks related to logistics, speed, accuracy, and size limitations. Chapter 4 discusses the problems with current dish metrology methods, and presents an adaptation to the same panel metrology solution in Chapter 3 to the measurement and correction of alignment errors for full radio telescope dishes, as well as a path forward to measuring up to the 18-meter dishes prescribed for ngVLA.

Note

The chapters of this dissertation are based on a collection of published and submitted journal articles, included in the appendices. In-depth discussions of each

research study are provided in this dissertation.

CHAPTER 2

Large Fiber Array Spectroscopic Telescope: Optical Design for a Scalable Unit
Telescope

This chapter includes material from an article submitted to Springer *Nanomanufacturing and Metrology*, Appendix A, and SPIE proceedings from *Astronomical Telescopes and Instrumentation 2022*, Appendix B.

2.1 Background**2.1.1 Why we want larger telescopes and why we can not build them.**

The goal of building future large telescopes is daunting when considering the rapid scaling of cost with aperture diameter. However, while the goals of some astronomy topics require more angular resolution, others only require more photons. Spectroscopy relies on collecting light from one or more astronomical sources, dividing it based on wavelength, and analyzing it to understand the spectral composition of the source. Most large telescopes have segmented apertures which need to be co-phased for direct imaging of objects. This careful co-phasing is not required to perform spectroscopy of brighter stars observed at the seeing limit of approximately 1 arc-second due to the atmosphere. If a telescope was dedicated to such spectroscopy, the aperture no longer needs to be coherent. Large telescopes are expensive due to challenges in the manufacture, mounting, support, and control of a surface over a large area to form a cophased aperture. Instead of one expensive large telescope, the cost versus aperture power law discussed in the introduction could be inverted to produce many smaller telescopes that create an equivalent collecting area, for the purpose of spectroscopy. The concept of many smaller telescopes being linked together with optical fibers to form a spectroscopic slit was first introduced by Angel et. al. in 1977[25]. Since then, the discovery of exoplanets in 1992[26] prompted a new area

of astronomical research: transit spectroscopy. Transit spectroscopy occurs when an exoplanet crosses directly between its host star and Earth, occulting the star slightly, and changing the spectral composition of the light slightly by absorption in the exoplanet's atmosphere.[27, 28] Transit spectroscopy is the perfect application for a telescope made up of smaller telescopes, linked together with fibers. The signal from the absorption of an exoplanet's atmosphere is incredibly small compared to the light from the host star. As a result, extremely large apertures are needed to reduce photon noise sufficiently to make a detection of some expected bio-signatures like oxygen[29]. The speed of detection of oxygen in the atmosphere of a nearby exoplanet is highly dependent on a number of factors: the duration and frequency of transits, the resolution of the spectrograph, the brightness of the host star, the size of the collecting aperture. With current telescopes, the detection of oxygen would take many decades to confirm, even using the GMT, TMT, and E-ELT combined. In reality, a 100-meter diameter telescope would be required to make regular observations of nearby exoplanets and reduce the time to a few years. Based on the power law, a 100-meter telescope would be 30 times more expensive than GMT (using $D \propto 2.45$), landing at roughly \$60B in 2023 dollars.

2.1.2 A larger collecting area without building a larger telescope: The Large Fiber Array Spectroscopic Telescope

A 100-meter diameter circular aperture telescope would be roughly 7,800 m^2 of collecting area. The collecting area of E-ELT is 1,200 m^2 . The Large Fiber Array Spectroscopic Telescope (LFAST) is a concept for an array of 2640 30" diameter telescopes, that together make-up 1,200 m^2 by collecting light from each telescope via 18 μm optical fibers and combining it to form a single slit-input for a spectrograph. E-ELT has a diameter of 39 meters, 50 times larger than the 30" LFAST telescopes. Using the cost scaling law, a 30" telescope should cost roughly \$100k, thus the array would cost only \$264M, nearly 5 times cheaper than E-ELT. Angel et. al.[30] expects that this unit telescope cost could scale even lower by taking advantage of 5-meter scale tracking mounts carrying 20 telescopes each, avoiding the

use of a protective dome, and other advantages of at-scale manufacturing. The goal is that the telescope may cost roughly $\$50,000/m^2$, or $\$60M$ for the whole array. At scale, the cost of each telescope should scale linearly, making a 100-meter ($7,800 m^2$) equivalent collecting aperture possible for less than $\$500M$.

LFAST will be comprised of 132 altitude and azimuth tracking mounts. 'Unit' telescopes and fibers from 132 '20-unit' mounts are combined at a central location for spectrograph input. Figure 2.1 shows a rendering of the 20-unit telescope.

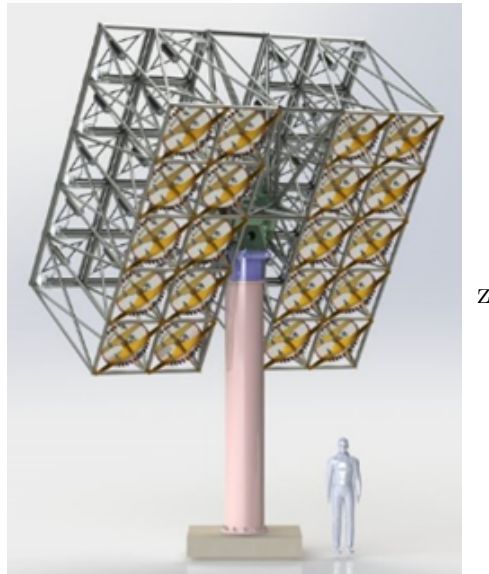


Figure 2.1: Rendering of 20-unit telescopes mounted on a single alt-az bearing. An array of 132 of these is equivalent in collecting area to E-ELT.

The engineering problems for this kind of telescope are very different from traditional ELTs, where extensive time and money can be spent on a single telescope's design, manufacturing, integration, and operation. For LFAST, the goal is to evolve a robust manufacturing and integration process early in the telescope development process and replicate it many times. The desire to eliminate recurring costs is key. This drives the need for a large portion of the telescope cost to be from non-recurring engineering (NRE), such that the extra cost per every additional telescope quickly diminishes as the number of telescopes manufactured increases and approaches a

regime of cost scaling linearly with collecting area. The optical design for the telescope directly impacts manufacturing, alignment, assembly, and operation, therefore setting the right optical design is key to reducing costs in downstream processes.

2.2 Requirements for each unit telescope

When designing any optical system, a set of three specifications are needed in order to define the design problem: wavelength range, aperture diameter, and field of view (FOV). Figure 2.2 shows a summary of the requirements. The goal of LFAST is to make the telescope as versatile as possible for a broad range of spectroscopic applications beyond just transit spectroscopy. The goal was to design each telescope to be diffraction limited on-axis over two octaves of bandpass. We selected 400-1700 nm to cover a broad range of potential molecular absorptions that could be observed during an exoplanet transit. Below 400 nm, the UV-band edge of most dielectric materials, including fused-silica fibers, causes poor transmission due to ionization. For aperture size, we chose 30" for a number of reasons. First, reducing the total number of fibers to combine to form a spectrograph slit is beneficial from a cost of assembly standpoint, so more collecting area per unit telescope is better. If the aperture is made smaller, LFAST must make more telescopes to achieve the goal total collecting area. This means more correcting lenses, more fibers, more guide cameras, etc. We decided that 30" was the largest that we felt comfortable making while also reducing the number of required peripheral hardware. 30" aperture diameter would will create roughly 1 arcsecond images (using 1.1) even for the longest 1700 nm wavelength. Typical atmospheric seeing should also be on the order of 1 arcsecond, so there is ultimately no imaging gain in making a larger telescope without the assistance of adaptive optics. We also felt that a mirror with $f/\#$ between $f/3$ and $f/4$ would be easily achievable and well-matched to most fiber numerical apertures (NA) that are used in astronomy. We allowed the focal ratio of the telescope to vary in the design between those two values, landing on $f/3.33$ in the final design.

<i>Specification</i>	<i>Value</i>
f/#	f/3.33
Wavelength Range	400-1700 nm
Aperture Size	30" (762 mm)
Fiber Core Diameter	18 μm
Plate Scale	12.3 $\mu\text{m}/\text{arcsec}$
FOV	4 arcmin HFOV
Maximum viewing angle from zenith	70°
Performance: On-axis @ fiber as-built	Average for 2640 Monte Carlo trials >80% encircled energy into fiber
Performance: 4 arcmin @ guide camera	1 arcsec FWHM spot size

Figure 2.2: Requirements for an LFAST unit telescope.

There are a few interesting things to note about the specifications for an LFAST unit telescope. First, there are two places where image quality is important: at the fiber injection and at the guide camera. A paraxial layout of the telescope is shown in Figure 2.3. At the 18 μm fiber (cure set in a planar fold mirror), only the near on-axis fields are important. The only goal at that surface is to get as much starlight as possible in the fiber core, allowing image quality requirements for the rest of the field to be less strict. The image quality across the whole field only matters at the guide camera, and only $\sim 380\text{-}950$ nm light can be detected by typical CMOS sensors. There are three purposes for the guide camera: to know where the telescope is pointing in the night sky, to give feedback on the coupling of the starlight into the fiber, and to give information on the telescope aberrations. The fiber will show up as a 18 μm 'black hole' in the center of the FOV on the guide camera. Being able to couple dim stars into the fiber is important, so brighter stars in the field need to be used to triangulate their locations. Good imaging performance means more photons per pixel, which means improved guiding on dimmer stars, but the performance at this surface does not need to be diffraction limited. We expect LFAST will be located at a site that supports arcsecond-quality seeing conditions,

so we aimed for arcsecond full-width half maximum (FWHM) at the guide camera to balance image quality with atmospheric effects.

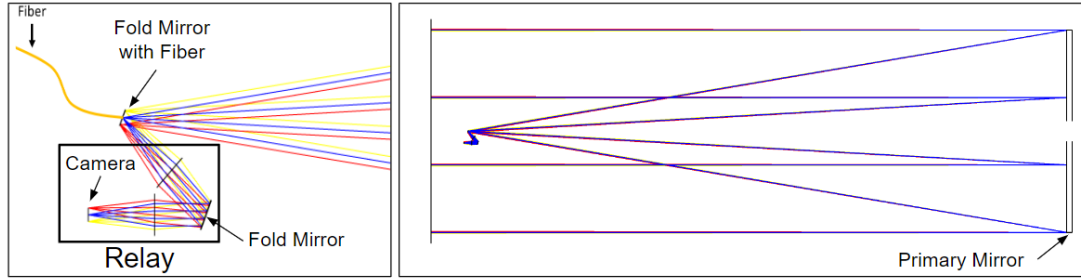


Figure 2.3: The paraxial model here is shown with a ± 4 arcminute field. The guide camera needs a significantly larger FOV than at the fiber in order to ensure that there will be stars with enough brightness to guide with. The chosen field gives a 97% chance of at least one 16th magnitude star in the field of view, which we found can be captured with a signal to noise ratio of ~ 30 with a 10 second exposure[1, 2].

In addition, we have a requirement for being able to view objects down to 70° from zenith as well as perform over two octaves of bandpass, to cover as much of the night sky as possible and collect a broad bandpass for spectrographs. For the $18 \mu\text{m}$ fiber, and a focal length of 2520.12 mm, the fiber subtends 1.47 arcseconds on the sky. At 70° elevation from zenith, atmospheric dispersion is a few arcseconds, so correction needs to be made to maintain performance across the bandpass. The fourth lens in the corrector stack is used as an atmospheric dispersion compensator, which is described in more detail in Section 2.4. Lastly, we are producing these telescopes in mass quantities, with maximum energy coupled into each telescope's fiber. As a final performance check, 2,640 Monte Carlo trials were performed to represent all telescopes in the $1,200 \text{ m}^2$ array to ensure that an average of at least 80% encircled energy is maintained in presence of all alignment errors. The rest of this chapter will describe each piece of the LFAST design, and the reasoning behind it in attempt to make a cost-effective, high-performing telescope.

2.3 Optical Design

In 2022, I designed the first iteration of the LFAST unit telescope and presented it at SPIE Astronomical Telescopes and Instrumentation in Montreal, Canada (Appendix A). In 2022 and 2023, we went on to manufacture the entire unit telescope and mount it on the same altitude and azimuth drives that are planned for the 20-unit telescope, with a goal of completion by the end of 2024. In 2023, we have been performing testing on the unit telescope, and using lessons learned to redesign some of the optical components for next year's 20-unit telescope prototype. The updated design and analysis has been submitted to Springer Nano-manufacturing and Metrology Special Issue on "Astronomical Optics Manufacturing and Testing" (Appendix B). The following optical design subsections focus on the updated design for the 20-unit telescope and summarizes some of the changes and lessons learned from the first unit telescope. Figure 2.4 shows layout of the final design to be used for the 20-unit telescope, and Figure 2.5 shows the table with the full design prescription.

2.3.1 Primary Mirror

A substantial driver of cost and schedule in nearly any large telescope is the primary mirror, and all ELTs currently in production have known this since the project design phase[31, 32, 33]. This is often due to logistical and physical limitations of manufacturing large, custom mirrors. It takes a long time for large glass mirrors to cool, and a long time to remove material to polish perfect aspheric shapes. This would be impractical if LFAST were to make mirrors in a similar way, since the goal is to make thousands of them. The cost of the primary mirror needs to diminish at higher manufacturing volumes for the concept of LFAST to be viable. This leads to a rather unusual design decision for meter class telescopes[34]: a spherical primary mirror. While spherical primary mirrors suffer from significant spherical aberration (on-axis) and coma (off-axis), they are much easier to make via using full-sized pitch polishing laps. This method naturally produces spherical shapes, reducing the time and costs associated with figuring. Spherical primary mirrors are more tolerant to

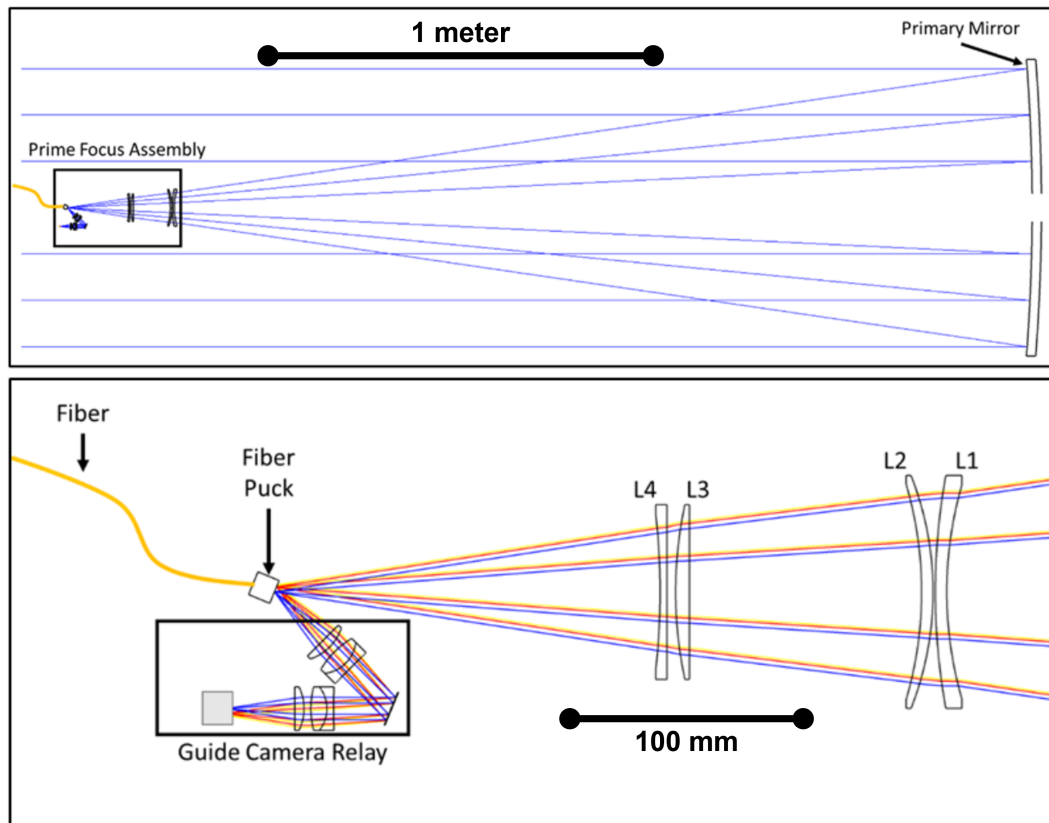


Figure 2.4: 2D optical layout of the final designed unit telescope for the 20-unit prototype (top). Zoomed in view of the 2D layout of the prime focus corrector assembly, including corrector lenses, fiber puck, relay system, and guide camera (bottom).

alignment errors since they have no axis, an additional benefit. Even an optimized aspheric mirror would still leave significant coma in the near off-axis fields needing correction in some downstream optics. A conic would also require aspherizing in the polishing process, costing the project money and time. Spherical is actually the optimal choice for the primary mirror shape for a small, narrow field of view telescope meant for mass manufacturing and single object spectroscopy.

The team had initially considered a Mangin mirror (reflective coating on the back surface) to extend the lifetime for mirror coatings outdoors[35]. While Mangin mirrors would have the added benefit of extended lifetime, there are significant

Primary Mirror		
	R	5275.0 mm
	Substrate	BOROFLOAT
	Clear Aperture	30 inches
	Spacing to L1	2351.83 mm
Prime Focus Corrector		
L1	R1	170.22 mm
	R2	279.50 mm
	Thickness	8.0 mm
	Substrate	H-K9LGT
	Diameter	101.6 mm
	Spacing to L2	1.0 mm
L2	R1	141.69 mm
	R2	167.86 mm
	Thickness	8.0 mm
	Substrate	H-F4
	Diameter	101.6 mm
	Spacing to L3	95.40 mm
L3	R1	Infinity
	R2	185.37 mm
	Thickness	7.0 mm
	Substrate	H-K9LGT
	Diameter	76.2 mm
	Spacing to L4	5.67 mm
L4	R1	Infinity
	R2	295.5 mm
	Thickness	3.9 mm
	Substrate	H-F4
	Diameter	70.0 mm
	Spacing to Fiber Puck	167.86 mm
Fiber Puck		
	Tilt Angle	22.5 degrees
	Fiber Diameter	18 μ m
	Spacing to Relay Singlet	35 mm
Relay		
Singlet	R1	Infinity
	R2	27.72 mm
	Thickness	5.0 mm
	Substrate	H-K9LGT
	Aperture	19.0 mm
Doublet	R1	43.44 mm
	R2	19.54 mm
	R3	Infinity
	Thickness 1	6.0 mm
	Thickness 2	3.0 mm
	Substrate 1	H-K9LGT
	Substrate 2	H-F4
	Aperture	19.0 mm
Distance to Fold Mirror	26.91 mm	
Fold Mirror		
	Fold Angle	25 degrees
System Properties		
	f/#	3.33
	Focal Length	2534.3 mm

Figure 2.5: Optical prescription for each unit telescope in the first 20-unit LFAST telescope.

downsides in their manufacturing, testing and operation. A Mangin primary mirror for LFAST would require polishing both sides of a 30" mirror, potentially doubling the time on a full-sized lap. The homogeneity of the glass in the mirror would also be important since it is used in double-pass. Inhomogeneity in a Mangin LFAST mirror would add an additional layer of complexity in characterization and correction of the wavefront error introduced by it. There would also be a tight requirement on the two Mangin mirror surfaces to be concentric. If the mirror has wedge, lateral chromatic error would be introduced to the telescope. All of these potential errors would need complementary metrology efforts in order to characterize them. In addition, the emissivity of glass versus silver would cause large index of refraction variations in a Mangin mirror. For these reasons, we decided to not pursue Mangin mirrors for LFAST, even though they may have a longer lifetime outdoors. A single coated surface is a much simpler and likely more cost effective choice in this case.

2.3.2 Prime Focus Corrector

The corrector optics can be split into two categories: before the fiber injection, and after the fiber injection. As was discussed in Chapter 2.2, the requirements at each of those image planes are quite different. At the fiber, only a central few arcsecond field of view is crucial for diffraction limited imaging performance for maximum fiber coupling efficiency for the as-built telescope. At the guide camera, it is only important to obtain a larger field of view, sufficient that there are available stars for tracking.

The corrector optics were designed to maintain the focal ratio of the primary mirror, contributing minimal optical power. This allows for loose axial alignment and manufacturing requirements for the corrector lenses. The spherical primary mirror on its own has ~ 65 waves of spherical aberration, relative to a paraboloid of the same size and focal length. Maksutov originally revealed that third order spherical aberration can be perfectly corrected with a single meniscus lens close to focus, where the lens is self-achromatic[36]. However, this single lens cannot correct coma, leaves some residual transverse chromatic aberration, and adds more higher

order spherical aberration. This lens is essentially L1 in the LFAST design. To reverse the additional higher order spherical aberration and coma and keep the focal ratio constant, only two lenses are needed to give enough degrees of freedom, one of flint and one of crown to correct for chromatic aberrations. This leaves a small amount of astigmatism and Petzval curvature[37, 38]. At this point, the system can either be diffraction limited within a 1 arcminute field and degrade significantly toward off-axis fields, or be balanced across the full field. Figure 2.6 shows an LFAST telescope with just two lenses, and the spot diagrams for the on-axis, 3-arcminute, and 4-arcminute field when weighting the optimization for RMS spot size equally, or more heavily for the on-axis field.

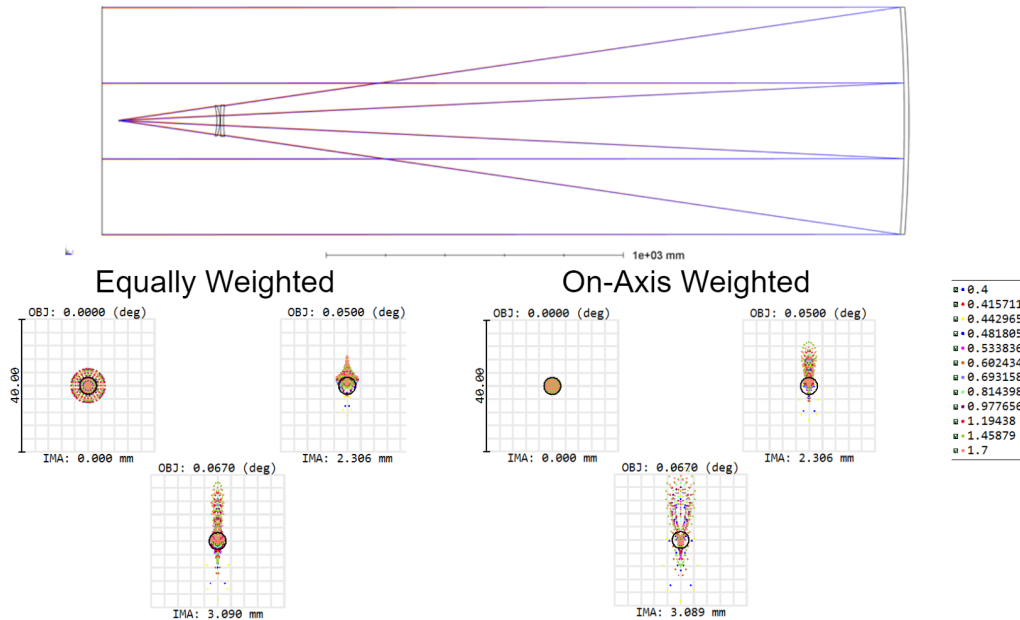


Figure 2.6: Conceptual design to create high quality images on-axis, for two-octaves of bandpass. If the optimizer is weighted toward the on-axis field, diffraction limited imaging is achieved in the vicinity of the on-axis field, and degrades for the rest of the field. Black circle in the spot diagrams is the airy disk for $1 \mu\text{m}$ wavelength. Alternatively, the imaging performance can be balanced if weighted equally. While this simple telescope design works in theory, the addition of atmospheric dispersion compensation and better performance near the on-axis field is needed for the as-built telescope.

To give some margin for optical and mechanical tolerances and pointing errors, we require a broader range of diffraction-limited imaging performance. Thus, more than two lenses are needed to extend the diffraction limited performance beyond the on-axis field. We found that two more lenses (L3 and L4) enable this correction, as well as atmospheric dispersion compensation, to be discussed in the next section. The corrector was designed with these concepts in mind, correcting for Seidel aberrations one by one and sequentially from L1 to L4. All lens radii and spacings were optimized to achieve diffraction limited spot sizes within a 1 arcminute field, from $1.6 \mu\text{m}$ Airy radius at 400 nm to $6.9 \mu\text{m}$ at 1700 nm. Figure 2.7 shows the polychromatic RMS spot size as a function of field. The traditional glass types of N-BK7 and F2 from Schott were originally chosen for the corrector lenses for their low cost, high manufacturability, and good transmission in the required bandpass, but these days those traditional glass types are much higher cost than alternatives. In the current design, equivalent H-K9LGT and H-F4 from CDGM will be used instead due to availability and cost, but in theory any crown-flint combination with Abbe number difference comparable to 27.7 for BK7 and F2 could achieve good image quality.

2.3.3 Atmospheric Compensation

As mentioned previously, the optical system needs to meet all specifications across the entire two-octave bandpass, even at elevation angles close to the horizon. Exoplanet transits happen all the time, in various parts of the sky, thus covering as much sky as possible gives a higher probability of being able to observe them around candidate stars. Across 400 to 1700 nm, nearly 4 arcseconds of atmospheric dispersion is present at 70 degrees from zenith (shown on the left in Figure 2.9, which means significant dispersion correction is necessary for optimal coupling into the 1.47 arcsecond fiber. Common atmospheric dispersion compensator (ADC) strategies involve counter-rotating prisms (Amici prisms, or CR-ADC)[39, 40], linear ADC's (LADC) using axial motion of thin wedge prisms[41], tilting low-power lenses[38], or compensating lateral ADC (CL-ADC)[42, 43] using counter-translating lenses. CR-

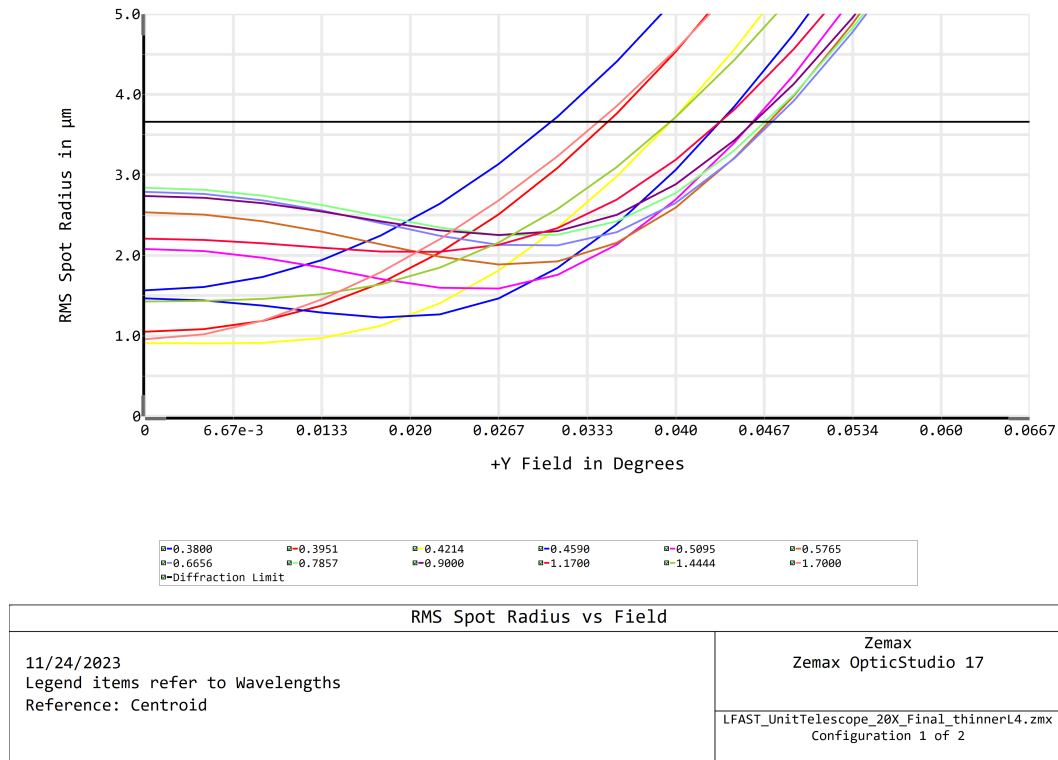


Figure 2.7: RMS spot size at the fiber image plane as a function of field position. Diffraction limit is shown for 900 nm. The telescope is diffraction limited at this wavelength up to ~ 0.03 degrees.

ADCs and LADCs work extremely well and can be designed to correct secondary color down to 10s of milliarcseconds[40], but often involve complicated mechanics to achieve the desired prism motion. Commonly these method correct dispersion down to only 50 degrees. Operating down to 70 degrees nearly doubles the amount of observable sky, creating more opportunities to observe transits.

For the thousands of telescopes in LFAST, fewer moving parts are desirable to eliminate points of failure. In addition, CR-ADCs and LADCs add additional components, causing energy losses at each interface and taking up valuable space and mass in the prime focus corrector of each telescope. The simplest solution for LFAST is the concept of CL-ADCs, as it does not add any additional components to the system. Typically, this method involves counter-translating two lenses to

compensate for the tilt and astigmatism caused by translating one of the lenses. Since the only performance metric that matters is encircled energy into the fiber, perfect correction of atmospheric dispersion is unnecessary, thus some secondary spectrum can be tolerated. I designed the telescope to require translating only one lens for atmospheric dispersion correction. Using lateral translation of only one lens also creates significant image motion. Usually this would be a problem for any other telescope that has a primary mirror with an axis, where tilting the primary mirror would cause significant aberrations. Since the primary mirror is spherical (no axis) and the required time for this correction is slow, simply tilting the primary mirror to recenter the celestial target on the fiber can be done with minimal effect on the image quality.

This design utilizes L4 as the ADC component. L4 decentering can perfectly correct primary lateral color caused by the atmosphere (match the position of chief rays of the shortest and longest wavelength in the bandpass). Figure 2.8 shows a plot of the primary lateral color caused by the atmosphere as a function of elevation angle [44, 45], the primary color induced by L4 as a function of decenter, and thus the L4 decenter required at each elevation angle to correct for primary lateral color. However, since the atmosphere does not have the same dispersion as the H-F4 flint glass in L4 (or any type of glass), this is not the best solution for optimum encircled energy coupled into the fiber. We carried out a numerical analysis to determine the actual required L4 decenter values to achieve the best encircled energy. At shallower elevation angles, these values start to diverge and expose the slight differences in dispersion of the flint glass and the atmosphere. A slight under-correction of primary lateral color due to the atmosphere yields the best encircled energy. Figure 2.9 shows an example corrected spot diagram at 70° from zenith. L4 needs to move 2 mm in order to correct the dispersion at this elevation angle, causing the image to move nearly 0.7 mm (~ 1 arcminute). Encircled energy in this worst case is 90.3%, compared to the diffraction limit of 92.7%. Thus, even in this worst case, the telescope would still be seeing-limited.

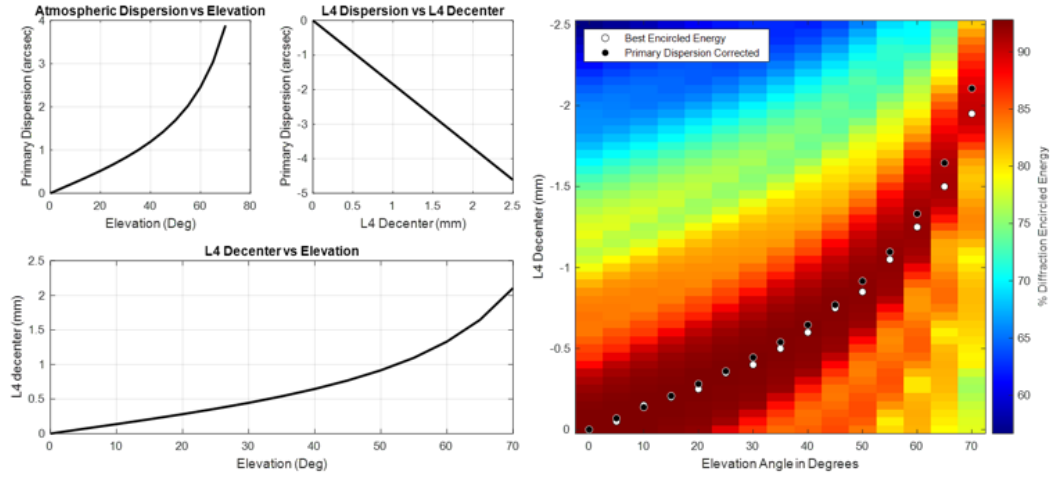


Figure 2.8: Optimization of L4 decenter to correct for atmospheric dispersion. Upper left shows the primary atmospheric dispersion (for 400-1700 nm) as a function of elevation and induced primary dispersion from L4 as a function of decenter. These curves can be mapped to the required L4 decenter to correct for primary atmospheric dispersion as a function of elevation angle (bottom left). The decenter required to correct for primary atmospheric dispersion correction, however, does not produce the best encircled energy, thus a numerical analysis was performed to find the optimal L4 decenter as a function of elevation (right).

2.3.4 Atmospheric jitter compensation

As mentioned in the previous section, translating L4 to compensate for atmospheric dispersion also significantly translates the image. In other telescopes, this would be an inconvenience, requiring extra components to compensate for the chief ray deflection and aberrations caused by misalignment of aspheric primary mirrors. For LFAST, we can use this property as an advantage. The atmosphere will cause seeing motion to the wavefront on the order of 0.5 arcseconds or less. This will significantly degrade fiber coupling efficiency if uncorrected. For every 100 μm translation in L4, the image moves 34 μm , or about 2.8 arcseconds. This is a small percentage of the lens motion needed to correct for atmospheric dispersion at low elevations on the horizon (for example 1.9 mm at 70 degrees), thus this lens motion can be used to correct for image motion caused by atmospheric wavefront tip/tilt without

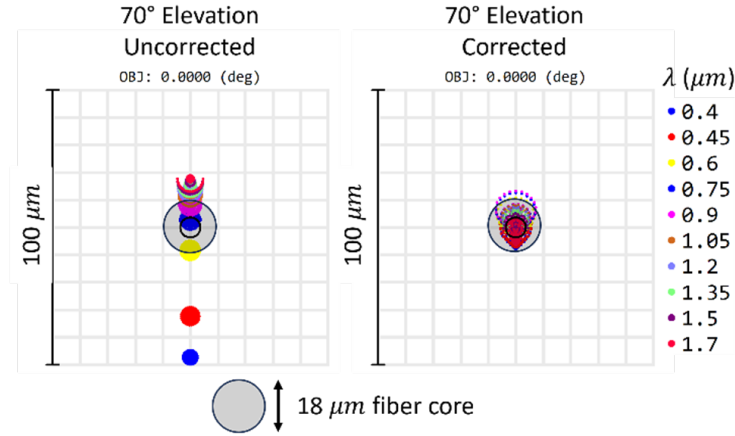


Figure 2.9: Spot diagram at the lowest elevation uncorrected (left) and corrected with L4 lateral translation (right). The corrected focus is shown after recentering the image on the fiber using tilt of the primary mirror. Also shown is the $18 \mu\text{m}$ fiber core in gray.

significantly disrupting dispersion correction. Looking again at Figure 2.8, for each elevation if the L4 decenter is non-optimal by $100 \mu\text{m}$, less than 1% encircled energy is lost, as opposed to more significant losses if the wavefront tilt is uncorrected. Implementing a rapid corrective movement on L4 allows LFAST to obtain improved performance with the presence of image motion due to seeing.

2.3.5 Fiber feed and relay optics

Each telescope will use feedback on whether light is properly coupled into the fiber or not, as well as a wide field for guiding. The LFAST telescope primary mirror is small, and thus has limited light collecting ability for short exposure times, which are required for fast guiding to reduce atmospheric image motion. A simulated image of a star when perfectly coupled with the fiber and when misaligned by 0.2 arcseconds due to the atmosphere is shown in Figure 2.10. The telescope needs a wider field of view in order to improve the chances of bright stars existing in the field of view to use for off-axis guiding. To achieve this, the fiber will be potted inside a small fold mirror at the image plane, which is relayed 1:1 onto a camera sensor with

a relay lens and another fold mirror, shown in Figure 2.4. This avoids losses that would be caused by using a beam splitter to pick off the guide field and maintains a mechanically compact layout. The requirements on the relay require a larger field of view, but a narrower bandpass. The relay was optimized for wavelengths 500-800 nm, over a 4-arcminute half field of view, to give a high chance of an available guide star as mentioned in Chapter 2.2. The relay is made of two copies of a simple lens assembly, a plano-convex lens and a doublet. Again, these lenses were originally made with N-BK7 and F2 but were switched to CDGM equivalents H-K9LGT and H-F4, The relay was redesigned with an equal optimization weighting across all fields. Figure 2.11 shows the polychromatic point spread functions (PSFs) at the guide camera sensor plane.

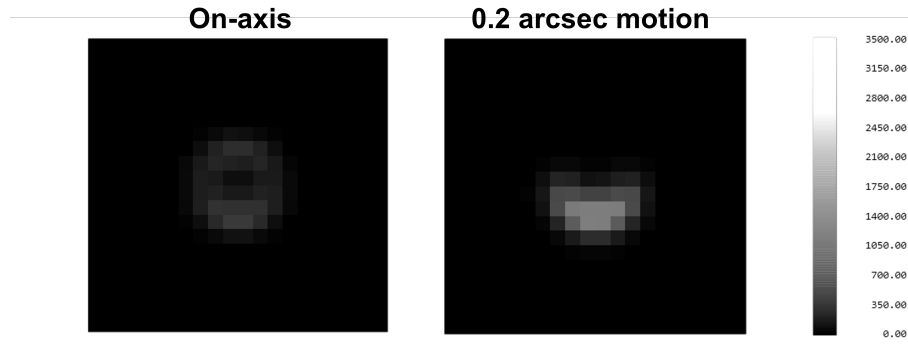


Figure 2.10: Simulated images of the 'black hole' at the guide camera due to the fiber. Shown is the off-axis image, and image given 0.2 arcseconds of image motion.

2.4 Tolerancing

Our initial design tolerancing was done with a small number of trials, but this telescope is designed to be built 2640 times, so a more encompassing Monte Carlo trial was executed to gain a perspective on how the telescope array as a whole may perform. Previously, a standard irregularity tolerance was used to specify the primary mirror, but this does not suffice for a meter-class mirror. For this new design, tolerancing was split into two pieces: the corrector and the primary mirror.

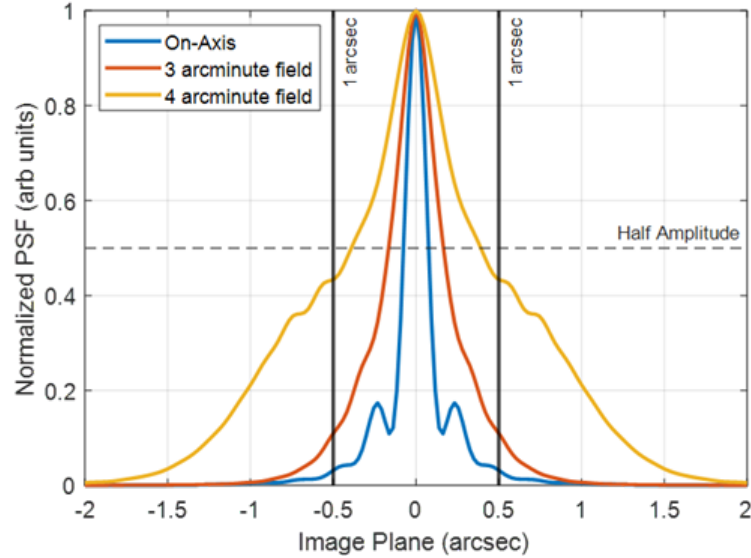


Figure 2.11: Polychromatic PSFs for 3 field points at the guide camera image plane. All field points are better than 1 arcsecond FWHM.

For mirrors of this size, it becomes difficult to specify with a single root-mean-square (RMS) or peak to valley irregularity value (e.g., $\lambda/4$ or $\lambda/8$). Wavefront slope is what truly impacts image quality, but slope cannot be described by a single depth RMS value, as it is dependent on spatial scale. A structure function is used to define the mirror requirements instead. The following sections tolerance the two key pieces of the telescope separately and attempts to balance the errors introduced by the mirror, the corrector, and the atmosphere.

2.4.1 Prime Focus Corrector

One of the key characteristics of LFAST is mass manufacturability at low cost. This largely depends on the optical and mechanical tolerances of the system to maintain high quality performance. LFAST needs components to be produced in large quantities, therefore any components that require high-precision machining or alignment are undesirable. All components and optics should be easily scalable both in their manufacturing as well as the assembly. Thus, we took great care to loosen

tolerances wherever possible to expedite production of LFAST telescopes at a low cost.

Because the primary mirror is spherical, and the prime focus corrector was designed to maintain the focal ratio of the primary mirror, axial errors have minimal impact on wavefront error (WFE). Thus, image degradation due to errors such as lens spacing, lens thickness, surface radii, and even refractive index, are mitigated with the assumption that primary mirror piston is a compensator for defocus.

Figure 2.12 shows mechanical tolerances and sensitivity curves for non-axial errors found for decenter/tilt of L1-L4. L1 and L3 are the most mechanically sensitive components, while L2 and L4 are looser. This information allowed us to better tighten tolerances where they are most effective as compared to the previous design. We began with 0.1 mm decenter tolerances on L2 and L4, 0.05 mm on L1 and L3, and 3 arcminutes (0.05 degrees) of tilt on all lenses, or approximately 0.1 mm edge thickness difference (ETD) at 100 mm diameter. Figure 2.13a shows how this is combined together with all other tolerances for Monte Carlo trials. All axial tolerances are very loose ($\pm 150 \mu\text{m}$), and were set to the standard loosest requirement per many optical manufacturer's tolerancing charts[46, 47, 48, 49].

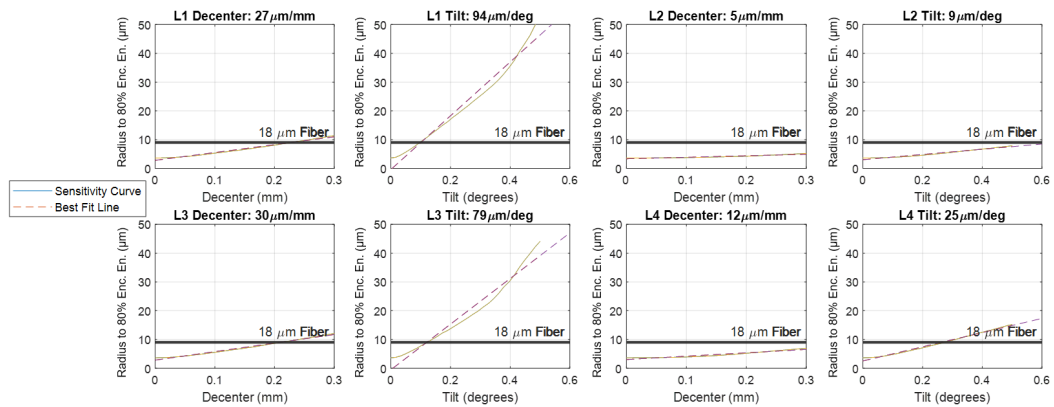


Figure 2.12: Sensitivity curves and best fit lines shown for decenter and tilt of each corrector lens. Sensitivity values are shown as $\mu\text{m}/\text{mm}$ for decenter or $\mu\text{m}/\text{deg}$ for tilt. These values indicate the increase in radius to 80% encircled energy per unit perturbation.

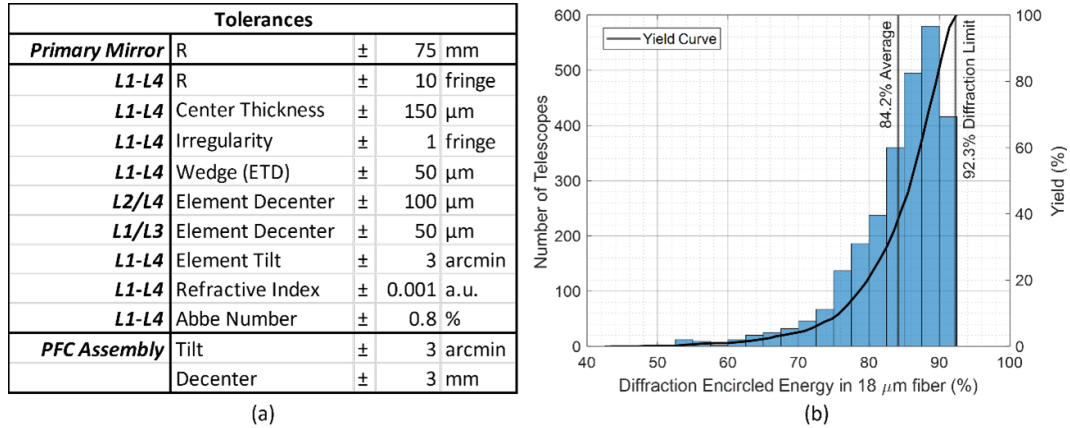


Figure 2.13: Final tolerances for the prime focus corrector (a). L1 and L3 have slightly more sensitivity than L2 and L4, thus the decenter tolerance is tighter for L1 and L3. Irregularity, wedge, radius error, center thickness, and material properties are all within standard tolerances for a variety of manufacturers. Mechanical tolerances are within achievable tolerances for a lens barrel. The yield curve and histogram (b) are shown for 2640 Monte Carlo trials using these tolerances with uniform statistics. The average performance is 84.2% encircled energy, and the number of telescopes is shown in 2.5% bin widths.

This tolerancing does not include aberrations on the primary mirror, but rather isolates properties of the corrector that are loose or sensitive. As expected, any axial errors due to surface power or lens spacing/thickness are easily compensated for with ± 25 mm of primary mirror piston. The most sensitive parameters are non-axial errors: lens decenter, lens wedge, and element tilt, although these are still well within commercial machining tolerances. All tolerances chosen are within "commercial" or "standard" tolerances given by a variety of optics manufacturers, and should be achievable with commercial machining and alignment tolerances for a lens barrel[50]. Figure 2.13b shows the yield for 2640 telescopes using uniform distributions of the tolerances shown in Figure 2.13a. The simulation showed that 80% of telescopes meet the 80% encircled energy requirement, and the average of all telescopes is 84.2% encircled energy.

2.4.2 Primary Mirror

All other surfaces in the telescope design have a single surface irregularity specification in number of fringes, which is a depth value. Common irregularity in pitch polished lenses takes the form of low order Zernike polynomials. However, for large surfaces, this specification is often not good enough, as mid-spatial frequencies become more present and impactful to the surface slope errors. For high performance systems, especially ELTs, a slope specification is needed to define surface deviations at a variety of spatial scales. LFAST uses 1" thick, 30" diameter BOROFLOAT® mirrors. This is the standard thickness for BOROFLOAT® glass, which reduces the cost of procurement. Due to the small aspect ratio of the mirror (30 to 1), it is likely that mid-spatial frequencies may show up in the polishing process due to local bending of the mirror. As the spatial scale of surface errors shrink but the amplitude does not, the RMS slope increases[51]. Because optical performance (wavefront error) is truly dependent on surface slope error, surface error amplitude requirements are directly dependent on spatial scale. A peak to valley specification suffers from the same problem[52]. At scale smaller than $\lambda/20$, light will react to the surface as if it is perfectly smooth.

The GMT mirrors have been specified using a structure function[53, 54, 55, 56], which is a measure of the wavefront error as a function of spatial scale. It is defined as the mean square wavefront difference between random points in the aperture as a function of their separation. It is used since wavefront error due to atmosphere turbulence is also commonly described by a structure function[57, 58]. Turbulence fundamentally limits the image quality of a telescope that does not use adaptive optics, like LFAST. It is expected that the location of LFAST may have seeing as good as 1 arcseconds FWHM, which will create a baseline best case encircled energy. Figure 2.14 shows this effect by convolving the polychromatic point spread function (PSF) of the telescope with a Gaussian of various arcsecond FWHM (or $2\sqrt{2\ln(2)}\sigma$).

At 1 arcsecond FWHM, we can expect approximately an 8% loss in energy.

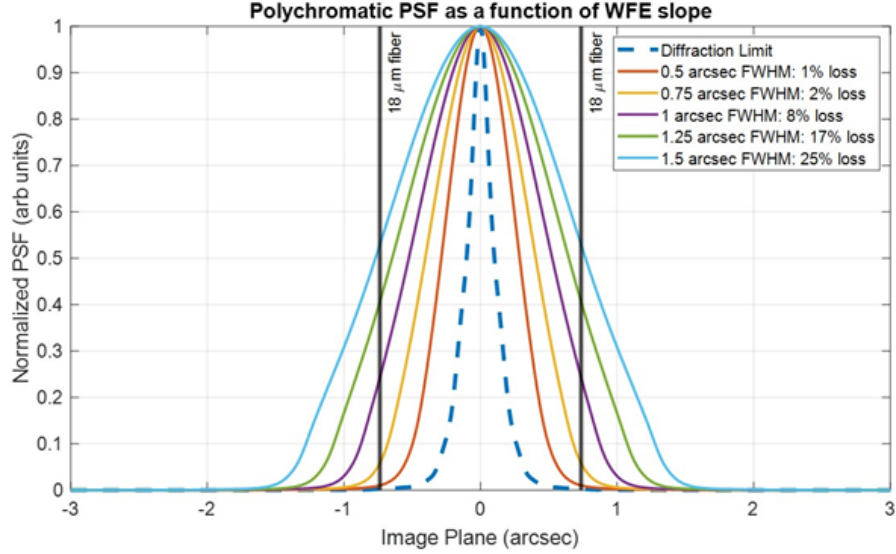


Figure 2.14: Point Spread Function as a function of seeing. Loss of encircled energy increases rapidly as the FWHM approaches the fiber diameter.

This can be similarly applied to requirements for the primary mirror to define a requirement for the structure function. We showed in the previous section that the tolerancing of the PFC accounts for on average 8% loss compared to the diffraction limit. Using a tighter requirement on the primary mirror would thus make the telescope seeing limited. A 0.5 arcsecond FWHM requirement on the primary mirror would thus roughly balance the error contributions from the primary mirror, the corrector optics, and atmospheric seeing. Figure 2.15 shows the resulting structure function requirement for 1 arcsecond FWHM (the same as expected from the atmosphere), and a goal of 0.5 arcsec FWHM, measured at the interferometer test wavelength, 632.8 nm. The LFAST primary mirrors will have 24 Peltier devices around the edge of the mirror to control low order Zernike deformations[30]. As with the GMT mirrors, eventually, the diffraction limit is reached and a better surface will not make a better image, thus the requirements can be loosened at spatial scales that correspond to required wavefront error smaller than $\lambda/20$ RMS.

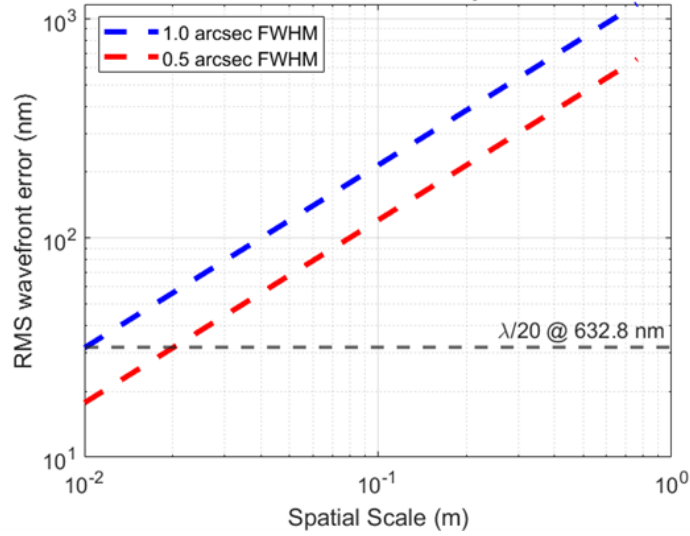


Figure 2.15: Structure function requirement for LFAST. 1 arcsec is the expected atmospheric seeing conditions, and 0.5 arcsec is the mirror requirement goal.

2.4.3 Testing

It is important to establish testing regimens to ensure that both the primary mirror and the PFC will meet performance requirements before testing them on-sky. For the primary mirror, the measurement is trivial: a phase-shifting interferometer with the mirror center of curvature aligned with the interferometer focus for a null test configuration. The collected data is then used to calculate the structure function and compare to requirements in Figure 10. Testing the PFC is more difficult.

The PFC compensates for the spherical aberrations present in the spherical primary mirror when used at infinite conjugates. In a blackbox, it appears as an optic with a large amount of spherical aberration, and a small amount of power. If the PFC on its own was tested in double pass with a flat reference mirror, there is enough power and spherical aberration present that the fringes would alias, rendering the wavefront unmeasurable. Additionally, a point source test with a spherical reference mirror would run into similar problems. To test the entire PFC assembly separately from the primary mirror, we have developed a null corrector made of two 3" H-K9LGT lenses to correct the on-axis aberrations introduced by the PFC.

The PFC will be tested with a 2" diameter collimated beam from a Fizeau interferometer. Figure 2.16 shows the layout of the null lens and PFC test in double pass.

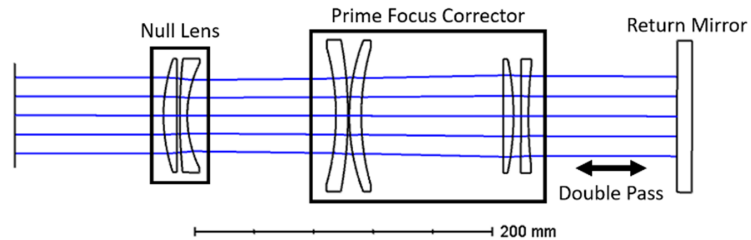


Figure 2.16: Null Lens, Prime Focus Corrector, and return mirror set up in a double-pass configuration. The returning beam has only 0.0033 waves of wavefront error.

Plano-Convex	Value	Units
<i>Material</i>	H-K9LGT	
<i>S1</i>	115.055	mm
<i>S2</i>	Inf	mm
<i>Center Thickness</i>	9	mm
<i>Spacing</i>	2	mm
Negative Meniscus		
<i>Material</i>	H-K9LGT	
<i>S1</i>	374.933	mm
<i>S2</i>	78.82	mm
<i>Center Thickness</i>	5	mm
<i>Spacing to L1 Vertex</i>	100	mm

Figure 2.17: Optical prescription for the null lens.

This double-pass Fizeau interferometer setup produces a $\lambda/300$ null. From the yield data in Figure 2.13b, about 80% of systems pass the 80% encircled energy

requirement. The Monte Carlo trials indicated that the wavefront error associated with this cutoff is 0.5 waves RMS. This wavefront error will be doubled due to double-pass but will only be tested with half of the full aperture (2" test beam versus 4" L1 and L2 lenses) thus we have set 0.5 waves RMS as the pass or fail requirement for the as-built PFC assembly under the double pass measurement. A computer generated hologram (CGH) could be used in place of this null lens, but for now the team aims to use a nulls lens due to its simplicity and familiarity among typical optical engineers and technicians.

2.5 Results from first unit telescope testing

This Chapter has focused on the design for the telescopes 20-unit assembly(it is the most recent, and better than the previous design), but it is important to briefly discuss the prototype unit telescope as-built. In 2022, the team used an older version of the design discussed in this Chapter. The design is very similar, with the main differences being lens diameter to thickness aspect ratio, atmospheric dispersion performance, and change of material. Many team members have been crucial in getting parts of the telescope together: rapid manufacturing of the spherical primary mirrors, designing and manufacturing the prime focus corrector housing, structural design of the telescope frame, control of the azimuth and elevation drives, and so much more. This section serves as a very short summary of the construction of the first unit telescope to put the previous parts of this chapter into context. The end of this section shows some initial results of on-sky testing with the single unit telescope.

2.5.1 30" Mirror

Manufacturing and Testing

Traditionally mirrors are made by grinding and polishing a glass blank. This process is a material removal process. The GMT blanks are made at the Richard F. Caris Mirror Lab by spin casting, where glass is melted and slowly spun in the furnace to

create the base paraboloid shape. The LFAST team has taken a different approach to manufacturing mirrors. The mirrors are formed from 1" thick, 32" diameter BOROFLOAT® blank disks (with a 3" inner bore hole for center mounting). The disks are placed on a precision machined, lapped and polished mold, and the mold and glass blank is heated to soften the glass and allow its own gravity to slump it to match the mold surface. Figure 2.18 shows the steel mold and the blank mirror being placed on it in the furnace. This process saves significant time that would typically be attributed to slowly removing material via grinding to form the rough shape of the mirror. The slumped glass mirror is then cooled, and sent to the fine grinding and polishing station to create the finished mirror figure, shown in Figure 2.19. Since the mirror shape is spherical, this can be done with a full-size lap, speeding up the polishing process from 6 months for a GMT mirror segment, to two days for an LFAST mirror.



Figure 2.18: Precision polished steel mold (left), lifting the 32" BOROFLOAT® mirror into the oven (center), and the slumped glass blank on the mold surface in the oven (right).

Mirror Mounting and Thermal Shape Control

We aimed to use a 18-point wiffle tree[59] to support the primary mirrors, modeled to only have 10 nm RMs error at zenith pointing. Since the mirror for LFAST is so thin, it is susceptible to warping due to thermal gradients. LFAST aims to use this as an advantage by applying thermal-electric coolers (TECs) to the back of the mirror to either deliver heat or take heat away[30]. With a proper applied heat map, Zernike surface terms can be added to the surface to offset errors in the inherent

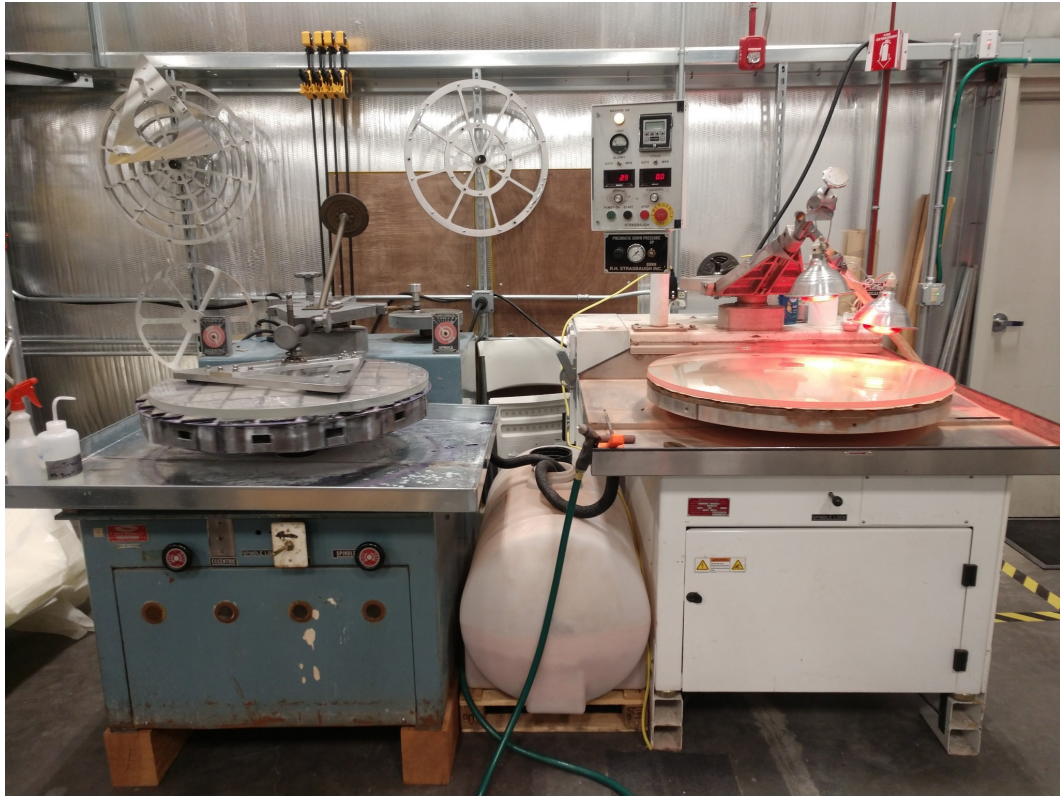


Figure 2.19: Grinding station (left) and polishing station (right).

mirror shape, or mirror bending due to gravity at a pointing angles below zenith. The mirror is a separate unit with three motors for tip, tilt, and piston adjustment, 132 TECs, and an 18-point wiffle tree. 24 edge TECs are used for control of low-order shape, with an additional 108 that may not be needed in the future. Figure 2.20 shows the completed assembly before mounting on the telescope frame.

2.5.2 PFC Mechanical Design and Alignment

Without a mechanical design, an optical design is just floating in the air. Dr. Andrew Monson designed the mechanical mounts for the PFC optics, and assisted with the lens alignment using a point source microscope (PSM) from Optical Perspectives. For the first unit telescope, atmospheric dispersion and jitter correction was not implemented, thus L4 was statically mounted to L1-L3. These lenses were aligned on a

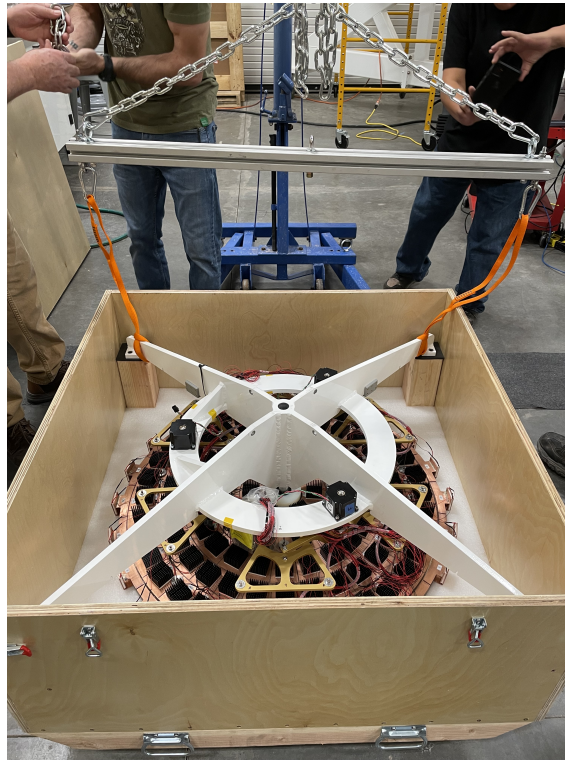


Figure 2.20: First LFAST primary mirror assembly.

lens centering station (LCS), and epoxied in place. The relay lenses were self-aligned using spacers, and held in place with standard Newport RMS thread retaining rings. Figure 2.21 shows the assembly process of the PFC lens mounts. Figure 2.22 shows the full top end assembly ready to be mounted to the telescope frame.

2.5.3 Unit Telescope Frame and Azimuth/Elevation Drive

To demonstrate the ability to use the two low-cost worm drives that are typically used in solar concentrator control, the LFAST team used the same worm drive on the single unit telescope as will be used for the final 20-unit telescope demonstration. A frame using the same tubing size and structure was used to build the first unit telescope. Figure 2.23 shows LFAST project manager Peter Gray (left) and principal investigator and developer of the original 1977 concept for LFAST, Roger Angel

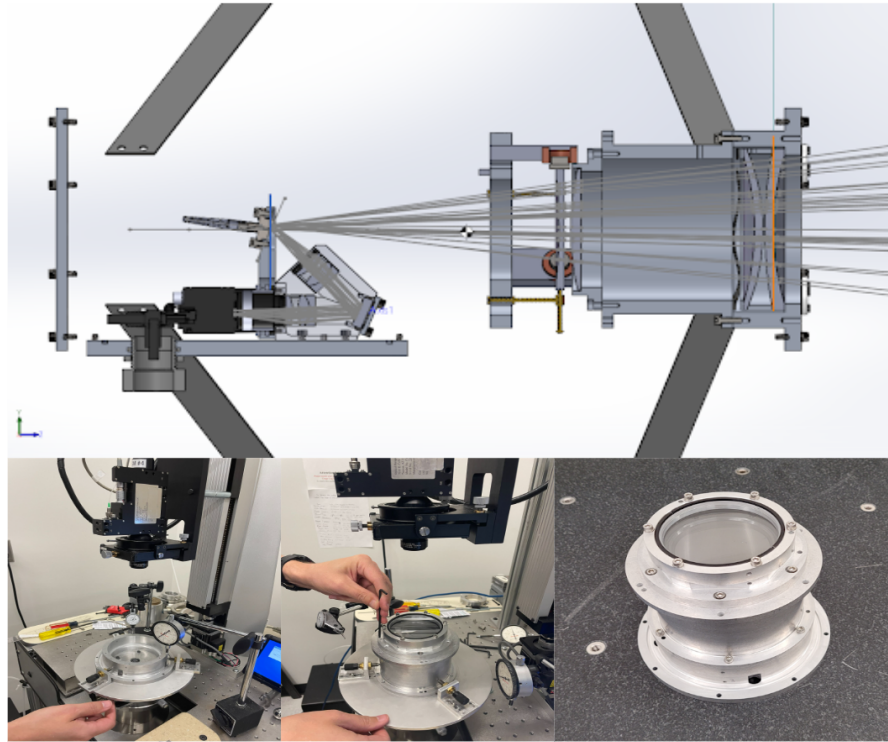


Figure 2.21: Shown here is the CAD layout cross-section of the mechanical mounts for L1-L4 and the relay lenses (top). The barrel was centered on the lens centering station (bottom left), and the optics were stacked in order from L1 to L4 (bottom center). Final assembled L1-L4 is shown on the bottom right.



Figure 2.22: CAD drawing of the PFC barrel (left), the barrel attached to its mounting structure (center), and the final PFC barrel populated with the lens assembly with graduate student Sonja Choi and Dr. Andrew Monson. (right)

(right).



Figure 2.23: The final painted frame for the single unit telescope. It uses the same azimuth and elevation drives and the same pier that the 20-unit telescope will use.

2.5.4 On-Sky Testing

The unit telescope has been used for significant on-sky testing in 2023, with the goal of understanding potential problems and improvements for the 20-unit telescope construction in 2024. Figure 2.24 shows the final assembled unit telescope on-sky at dusk, tracking Vega. The telescope is currently being tested at the UArizona Tech Park.



Figure 2.24: Final unit telescope on-aky at the UArizona Tech Park.

CHAPTER 3

Binocular Fringe Projection Profilometry for Metrology of Meter-Scale Optical Surfaces

This chapter is a summary of an article published in to *OPTICA Continuum*, in Appendix C. The software that runs the system described in this chapter has been licensed from Tech Launch Arizona to Fringe Metrology LLC (founded by the author of this dissertation). Fringe Metrology LLC aims to continue this research to address a number of improvements to the current system, which is described at the end of this chapter.

3.1 Motivation

In 2020, Dr. Justin Hyatt and Dr. Daewook Kim received a grant from the National Science Foundation (NSF) titled "Rapid and Inexpensive Thermoforming Technology for Precision Radio Telescope Reflector Panels". As discussed in Chapter 1, the project aims to avoid the use of expensive, custom molds, continuing the theme of scalability. Radio telescope reflectors are nearly always made with small individual panels, and those panels often have shapes that are different than other panels in the dish, especially for off-axis dishes. The project solves this problem by researching methods to develop an adjustable mold that can conform to a broad range of shapes that are in radio telescope reflector dishes. The process involves heating an aluminum panel to reduce its yield strength and allow it to 'fall' into the shape of the mold due to its own weight. But, as Jim Wyant puts it: "If you can't measure it, you can't make it." [60]. Without measurement feedback, this project would be nearly impossible. Measurements are needed at nearly every stage of research for this project. Measurements are needed in order to know how much to move each actuator on the mold, and to know when sufficient mold accuracy is achieved.

Measurements are needed to test how the mold changes after heating cycles. Measurements are needed to research the right heating cycle to apply to the aluminum panels. Measurements are needed on the resulting panels to characterize the spring-back and invert it to apply it to the mold. For this research project to function efficiently, a complementary metrology method is needed that is fast, accurate, has a large dynamic range, and works on a wide range of materials and surface finishes.

In applications such as radio astronomy and optical component manufacturing, reflecting and refracting surfaces need to have very accurate shapes, yet often have surface roughness that makes them non-specular to visible wavelengths, either as the final product or in an intermediate stage of manufacturing. This presents a significant measurement challenge, since scattering reduces coherence and specularity. For example, surfaces used in high frequency radio astronomy have a common accuracy requirement of $\lambda/25$ [61] (often tens of microns for millimeter-scale wavelengths) but still need to scatter visible and near infrared wavelengths to avoid unintentional heating from focused sunlight [62]. Measurement of these surfaces is crucial to the performance of the final antenna [8, 63, 64], but metrology methods that rely on specular surfaces are futile in this application.

Current measurement options for large antenna segments either require physical probing of the surface or measurement of the locations of physical fiducials. Coordinate Measuring Machines (CMM) have traditionally been used to measure surface shapes by touching the surface with a probe at multiple points [65] and extracting 3D points using encoders. This method is performed on a point-by-point basis, so oftentimes taking high spatial resolution measurements aren't possible in a reasonable amount of time, as each sampled point takes a few seconds to acquire. Laser trackers have also been heavily used in the manufacturing of individual panels and shape verification of the final constructed antenna [66, 20, 67, 68]. Laser trackers require physical placement of retro-reflector fiducials, meaning the fiducials need to be continuously relocated in order to sample a 3D point. Therefore, rapid high spatial resolution measurements are not possible with this method either.

Photogrammetry has also been used for some of these applications [65, 69, 70].

Photogrammetry involves capturing many images of precision fiducials that are placed on the surface, and triangulating the fiducials to produce 3D points. This method has shown high accuracy, but also requires manual placement of fiducials[71], significantly slowing the measurement process. In this type of system, pixel utilization is low: only pixels that see the fiducial pattern are used to triangulate object locations.

The original metrology plan for the project was to design and build an infrared (IR) deflectometry system to measure the panels and the mold. Deflectometry is a non-null, slope measuring metrology method, concept shown in Figure 3.1. I built such a system[72] and was able to produce data but found that it required different configurations to measure a broad range of convex and concave shaped panels. This made it challenging to calibrate to produce reliable low-order shape measurements and recalibrate every time a new configuration is required. The project needed a method that was more compact, flexible, and reliable.

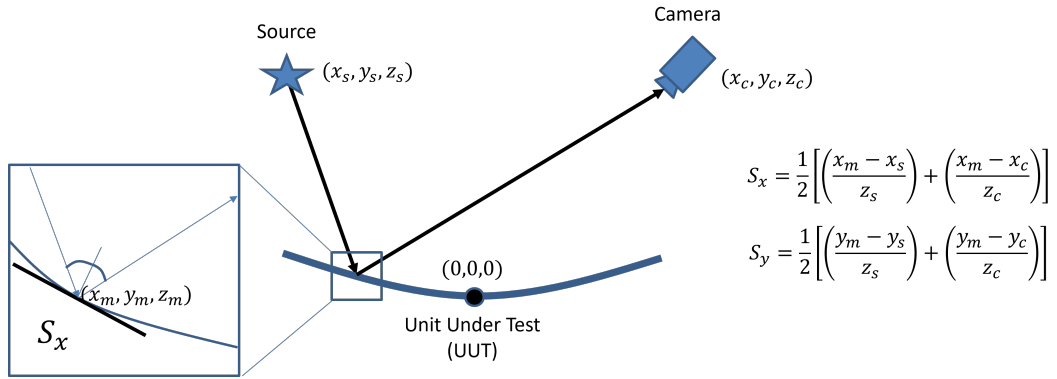


Figure 3.1: The concept of deflectometry, If the positions of a source, a camera, and a point on the unit under test is known, simple law of reflection can be applied to extract the surface slope at that point. Scanning the source to cover all points on the unit under test builds a slope maps of the surface, which can be integrated to reconstruct the surface depth map.

I ultimately decided that a structured light system was the right type of system for this application. Structured light scanning systems are similar to photogrammetry, but output much higher spatially sampled scans by utilizing a light source

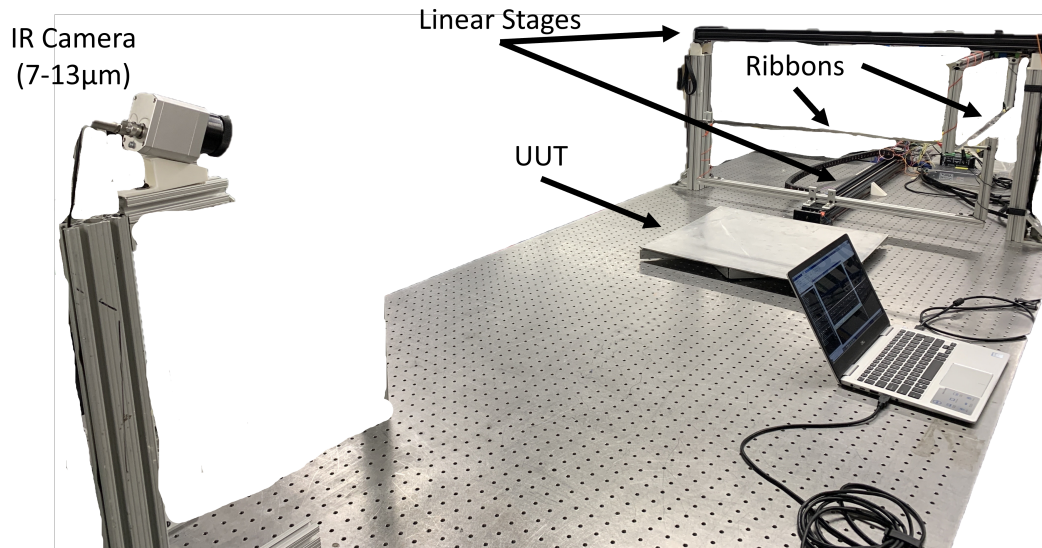


Figure 3.2: Actual implementation of infrared deflectometry. I used two nichrome ribbons on two separate encoded linear stages, one for X scanning and one for Y scanning. Current was allowed to flow through the nichrome ribbons as they were scanned using the linear stages, and a thermal camera was used to capture the reflected images.

to produce fiducials and observing the scattered image with a camera in order to extract more information about the surface via triangulation[73, 74, 75]. This makes it a great candidate concept for rapid metrology of large, diffuse surfaces like radio telescope panels. Recent decades have produced vast amounts of research into 3D scanning techniques using structured light, particularly Fringe Projection Profilometry (FPP)[76]. FPP is a sub-category of structured light measurement systems that specifically focuses on projecting a periodic pattern onto an object in order to rapidly extract feature information by observing the deformed pattern. There are many variations of FPP. Some research in this field focuses on optimizing system calibration methods[77, 78]. Others focus more on the hardware, using different types of projectors or numbers of cameras[79]. There is also significant research into reduction of the non-linear effect of the phase shifting algorithms[80, 81, 82, 83]. Much of the research in this field is focused on improving the measurement speed by using more efficient phase shifting algorithms that require fewer pattern acquisitions[84, 85, 86],

and converting phase directly to depth based on calibration of a camera and a projector[87]. However, in general there is little focus on scaling up the concepts to measure large surfaces with extremely high accuracy. When it comes to radio telescope panels, the bottleneck in the manufacturing process is more heavily attributed to the panel-forming method than to the metrology method. This allows for ample time to tune a FPP method for high accuracy or meter-sized surfaces.

3.2 Technical Background

3.2.1 Stereo Vision

The metrology method I developed for panel metrology is based on the simple concept of Stereo Vision (SV)[88]. SV computes 3D coordinates of objects based on the binocular disparity between the 2D images of an object from two different perspectives. It is used in everything from robotic navigation to 3D movies to our own human depth perception. If the intrinsic properties of the cameras are known (i.e. focal length, distortion, principle point) and the extrinsic properties of the camera pair are known (i.e. relative rotation and translation difference between each camera), a 3D object could theoretically be perfectly reconstructed. However, diffraction, camera noise, feature matching accuracy, and calibration errors of the intrinsic and extrinsic parameters result in an uncertainty in measured coordinates. These errors culminate into an expected depth resolution limit of a SV system, which depends on the geometry of the camera perspectives relative to the object to be measured, and the method used to match object features. The equation for estimating the depth resolution of a SV system is well-established in the field of computer vision[89]:

$$\delta z = \frac{z^2}{bf} \Delta p \quad (3.1)$$

where b is the camera baseline distance, z is the object distance from the baseline, f is the focal length of the cameras, and Δp is the disparity error in number of pixels multiplied by the physical pixel size, coming from the feature matching uncertainties

in the system. These parameters can be easily adjusted to give predicted resolution in the tens of microns for surfaces sizes on the order of a square meter using current image sensor technology (pixel size and total array size limitations), assuming disparity error is on the order of a pixel. This resolution starts to degrade for systems that attempt to cover a larger area. If a larger area needs to be measured, one could decrease the focal length, but this hurts depth resolution inversely. One could simply move the cameras further away, but the distance from the object hurts depth resolution quadratically. One could also extend the camera baseline distance, but this can cause depth of focus limitations, making calibration of extrinsic parameters difficult and creating poor spatial resolution in one dimension. Therefore the only way to significantly improve the depth resolution while keeping hardware configuration constant is to decrease the pixel disparity error by combining a robust feature on the object with a sub-pixel matching method. Fundamentally, the limits of the method are limited by the minimum detectable point separation. As SNR increases, the probability that a target is identifiable as two separate points also increases[90]. The SNR and therefore the matching limitation is thus limited by photon noise.

3.2.2 Fringe Projection Profilometry

FPP systems often involve projecting a series of N phase-shifted sinusoidal patterns onto an object and taking images of the distorted pattern with a camera[85]. The captured pattern typically takes the form of Eq. (3.2) for vertically oriented fringes:

$$I_n(x, y) = a(x, y) + b(x, y) \cos \left[u_0 x + \frac{2\pi n}{N} + \phi_{obj}(x, y) \right] \quad (3.2)$$

where u_0 is the fringe frequency, n is the current phase step, N is the total number of phase steps, and $\phi_{obj}(x, y)$ is the phase of the object observed by a camera's 2D detector plane, which contains information about the object shape. $a(x, y)$ and $b(x, y)$ are the background intensity and the fringe modulation, respectively. Projecting this series of N patterns onto an object and capturing images with a camera encodes that object with contours of equal phase (ϕ_{obj}). The wrapped

phase $\phi_{obj,wrapped}$ in Eq. (3.2) can be recovered with the N-step Phase Shifting Algorithm[84]:

$$\phi_{obj,wrapped}(x, y) = \arctan \left(\frac{\sum_{n=0}^{N-1} I_n(x, y) \sin(\frac{2\pi n}{N})}{\sum_{n=0}^{N-1} I_n(x, y) \cos(\frac{2\pi n}{N})} \right) \quad (3.3)$$

where $I_n(x, y)$ is the 2D irradiance pattern captured on the camera detector for each phase step n . This equation recovers the wrapped phase in modulo 2π steps, which can then be unwrapped with a spatial phase unwrapping method[3].

Most FPP systems then use a variety of phase-to-height mapping methods to produce 3D measurements, based on the calibrated geometry of the camera and projector, or a calibration surface[91]. Oftentimes the projector and camera is treated as a stereo-pair, where the projector acts as an inverse camera, and the phase contours are used as epipolar geometry constraints to determine matching features[85]. Either way, both of these methods require some form of calibration of the projector, which can be challenging to do accurately and quickly, and has limited dynamic range. This often requires additional calibration for gamma distortion, the nonlinear brightness response of displays[92, 93]. In addition, this method relies on the temporal stability of projector illumination.

3.2.3 Stereo Camera FPP

Some have added an additional camera to the system and leveraged multiple benefits[79]. With two cameras, the projector can simply act as a fiducial generator to assist stereo camera triangulation. Strategies to calibrate the intrinsic and extrinsic parameters of two cameras is very well-established [94]. In this case, the projector can be used to encode contours of equal phase using phase shifting in one direction, and feature matching based on the same epipolar geometry method as the projector-camera systems. This combines the concept of SV, requiring feature matching across two images from different perspectives, and FPP, requiring a calibration using a known object.

Looking back at 3.1, if the stereo matching precision (pixel disparity error) can be

improved to sub-pixel matching accuracy, then the theoretical depth resolution experiences the same linear improvement, assuming perfect calibration. As described in Section 2.2, using a set of phase-shifted sinusoidal fringe patterns encodes the object with contours of equal phase. Adding another set of phase shifted patterns oriented in the orthogonal direction encodes the object with a unique phase pair combination at every point on the 3D object, imaged onto a camera's 2D detector plane: $\phi_h(x, y)$ and $\phi_v(x, y)$, for horizontal and vertical phase, respectively, with x and y denoting the vertical and horizontal locations on the detector plane. Figure 3.3 shows an example set of projected fringes, the wrapped phase for each direction, and then unwrapped phase. I use a spatial phase unwrapping technique based on a reliability sorting method[3] to recover the continuous phase in the horizontal and vertical phase directions, for both cameras.

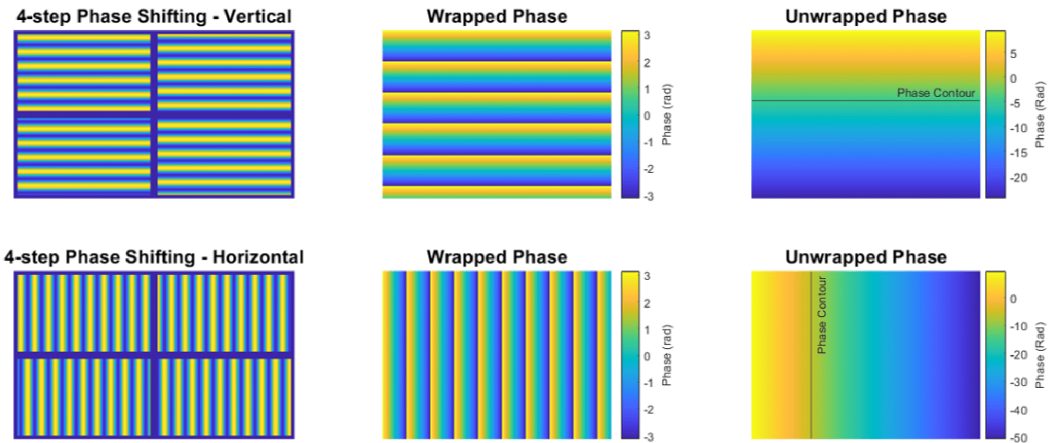


Figure 3.3: Phase-shifted sinusoidal patterns encodes contours of equal phase. Only four steps are shown for simplicity. Using Eq. 3.3 produces the wrapped phase maps. The reliability sorting method by noncontinuous path[3] is used to unwrap the phase. The result is a continuous phase distribution. Using this phase shifted pattern in two orthogonal directions produces two phase distributions, which encodes every point with a unique phase pair combination.

3.3 Binocular FPP with sub-pixel phase matching

3.3.1 Subpixel Matching Process

Pixels on camera 1 can be matched to pixels on camera 2 based on the phase pair that has the minimum difference, and these matched pairs of pixels are triangulated using the camera intrinsic and extrinsic parameters to produce a set of 3D points representing the object being measured.

However, this method does not fully utilize the information encoded on the object. The projector encodes the object with a quasi-continuous phase distribution, and those distributions are measured with a discretely sampled detector array from each camera’s perspective. It is highly unlikely that there is any one pixel on camera 1 that exactly samples the same area on the object as any pixel on camera 2. That means there is no pixel on camera 1 that has a phase pair that *exactly* matches the phase pair of a pixel on camera 2. Existing research has shown that subpixel phase matching can improve calibration via bundle adjustment using thousands of matched points and a variety of subpixel matching methods [95, 96, 97, 98].

We used subpixel phase matching to create a 3D point from every pixel on camera 1 that projects onto the object, and interpolate the rough matching location on camera 2 until the subpixel matching location is as precise as possible. In order to accomplish this, we can assume that there likely exists a subpixel location on camera 2 that nearly exactly matches the phase pair of a pixel on camera 1. Much higher feature matching precision can be obtained by matching the phase pair of a *pixel* on camera 1 to a corresponding phase pair subpixel *location* on camera 2 via interpolation. One could simply interpolate the entire phase map by a large factor, but the image size, and therefore the search algorithm time for finding matching phase pairs, scales by n^2 . This would make processing times far too long on an average computer, on the order of hours. One could also fit each phase distribution to a surface map and solve the matching phase pair locations analytically, but would require an extremely high number of terms in order to preserve high frequency surface information. Instead, we search the image first for a rough match, and use a

windowed interpolation strategy to iteratively search smaller interpolated windows, greatly reducing computation time while still producing subpixel matching precision, without losing spatial resolution. The steps of this process are described in-depth below and visualized in Figure 3.4.

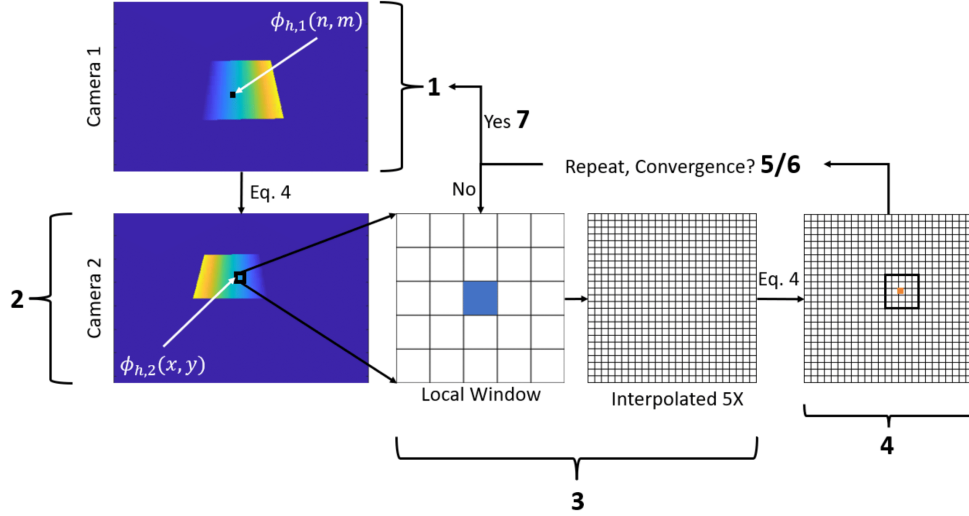


Figure 3.4: Precision stereo matching process shown for the horizontal phase only, for simplicity. For each pixel on camera 1, the closest matching phase pixel on camera 2 is found. A local window around the closest match is made and interpolated, and a new closest match is found. Repeating this process converges on a best matched 'location' on the camera 2 detector to each pixel on camera 1. Actual algorithm uses vertical and horizontal phase pair. With the vertical direction included in the matching process, there is a small window where the best matched phase pair must exist.

1. Start with a pixel on camera 1, which has phase pair $\phi_{h,1}(n, m)$ and $\phi_{v,1}(n, m)$, where n and m are denoting a pixel in the n^{th} row and m^{th} column on the detector plane.
2. The first interpolated window on camera 2 is identified with its center at (x_0, y_0) on camera 2 by finding the location that has the minimum root sum squares (RSS) phase difference from the current (n, m) pixel on camera 1:

$$([\varphi_{h,2}(x, y) - \varphi_{h,1}(n, m)]^2 + [\varphi_{v,2}(x, y) - \varphi_{v,1}(n, m)]^2)^{\frac{1}{2}} = \min \quad (3.4)$$

where (x, y) denotes the pixel locations across the entire image.

3. Create a local 5×5 window centered on the matched pixel (x_0, y_0) for each vertical and horizontal phase distribution on camera 2, and linearly interpolate the window $5 \times$, producing a 25×25 frame. This is the 0^{th} interpolated layer.
4. Step 2 is then repeated, but now finding the optimal pixel location on the 0^{th} interpolated layer only. We then search for $\mathbf{r}_0^* = (x_0^*, y_0^*)$ on layer 0 where we obtain the best matched phase, in other words:

$$([\varphi_{h,2}(x^*, y^*) - \varphi_{h,1}(n, m)]^2 + [\varphi_{v,2}(x^*, y^*) - \varphi_{v,1}(n, m)]^2)^{\frac{1}{2}} = \min \quad (3.5)$$

where $(x^*, y^*) \in \mathcal{N}$ is denoting the location on the small neighborhood of 25×25 (sub)pixels in the 0^{th} layer.

5. Create a second interpolated layer taking the 5×5 pixel window around $\mathbf{r}_0^* = (x_0^*, y_0^*)$ and then interpolate it to build another 25×25 -(sub)pixel grid as the second layer \mathcal{N}_2 .
6. Repeat step 5 and 6 until the following convergence criterion is met:

$$\|\mathbf{r}_{l+1}^* - \mathbf{r}_l^*\|_2 < 0.01 \text{ pixel} \quad (3.6)$$

where $l = 0, 1, \dots$ is the super-resolution layer. Thus, \mathbf{r}_l^* indicates the best center location for the l -th interpolated layer. The number of iterations it takes to meet this criterion varies from 1 to 5, depending on the amount of overlapping projected area on the object of the pixel on camera 1 with a corresponding pixel in camera 2.

7. Repeat the entire process for each pixel on camera 1.

Using the phase of the projected fringes as the SV fiducial has major benefits in robustness to both hardware and environmental errors. Effects such as projector nonlinear brightness, temporal and spatial brightness fluctuations and projector lens distortion errors are eliminated since phase is not used directly to determine depth,

but is simply a fiducial to assist determining parallax of stereo vision[99]. Applying this process to each pixel results in highly accurate subpixel feature matching, which leads to high depth resolution, high spatially sampled 3D point clouds representing the surface figure.

3.3.2 Calibration

To demonstrate the predicted accuracy of this technique over large areas, we assembled an example system to cover an area of 1 m². We used two 20 megapixel FLIR Blackfly USB3 cameras with Sony IMX183 sensors and 12 mm focal length lenses. For the projector, we used a 1080P Optoma GT1080HDR Short Throw Gaming Projector, which allows pattern projection over a large area from a short working distance. The sensor pixel size was 2.4 μm , the baseline distance was 2.5 meters and the object distance was 1 meter (Figure 3.5). Based on Eq. (3.1), this should produce a depth resolution of 80 μm assuming a one pixel disparity error, however the performance should be significantly improved via smaller pixel disparity error by using interpolated stereo matching.

The two cameras were calibrated using MATLAB’s Camera Calibrator App for the intrinsic parameters and the Stereo Camera Calibrator App for extrinsic parameters, calibrating only for radial distortion, since these well-made cameras and lenses should have negligible tangential distortion. This software uses Zhang’s well-known method[94]. We used 19 images of a 22x23 black and white checkerboard with 15 mm squares placed in a variety of locations and orientations within the field of view. The calibration involved covering the entire field of view of both cameras, near the planned working distance of the measurement surface. Figure 3.6 shows the camera layout with sampled locations of the calibration target as well as the corresponding reprojection error.

The mean reprojection error shown in Figure 3.6 of the calibration process was 0.16 pixels. While this may seem like the limiting factor in accuracy based on Eq. 3.1, it is only the limiting factor in calibration. Errors in calibration due to the calibration board itself (such as board flatness, gravity deformation, and

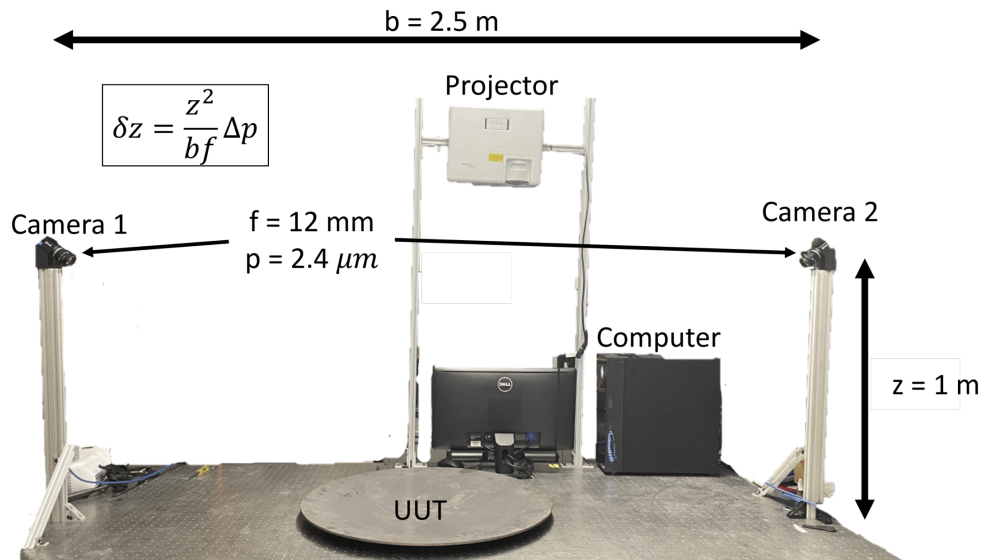


Figure 3.5: Actual system layout of cameras, projector, computer and unit under test (UUT). Note the rough placement of the projector. The only requirement is that the projector completely covers the UUT with fringes. The measurement is only made by stereo matching, so only the cameras require a stable mounting scheme. This configuration produces an expected depth resolution of $80 \mu\text{m}$ assuming one pixel of disparity error, but we expect the interpolated phase matching method to significantly reduce this.

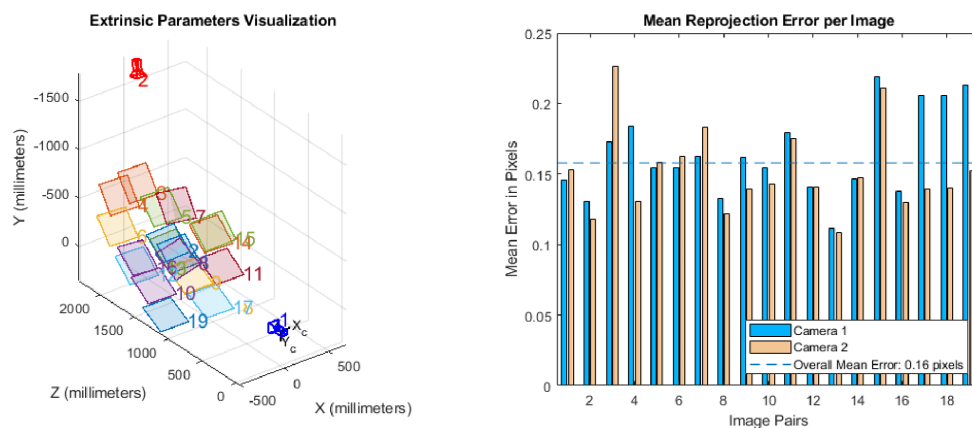


Figure 3.6: Layout of extrinsic parameters and calibration target locations (left) and their corresponding reprojection errors for each camera (right).

sharpness of checkerboard corners) as well as noise in the corner finding algorithm limits the calibrated reprojection error. It has been shown in other research that

measurements of real objects are required to evaluate the actual accuracy of a stereo-camera calibration[100]. For this reason we will focus on measuring real objects in Section 4.

It is important to note that this is just one embodiment of the system. In theory any combination of camera types (pixel size, array size, focal length) can be used in combination with any projector. The only requirements to obtain a 3D point on the surface is that both cameras see the same area on the object, and the projector also covers that area.

3.3.3 Data Acquisition and Processing

We employ an 11-step phase shifting algorithm in both orthogonal directions, making a total of 22 captured images for each camera, 44 images in total. Using 11 phase steps helps to reduce noise in the final measured phase maps [101, 102]. Eq. 3.3 is used to recover the wrapped phase, and the spatial phase unwrapping method based on reliability sorting from Herraes et. al. [3] is used to recover the unwrapped phase maps for each camera. Other methods aim to use fewer frequencies in order to speed up acquisition, but for this application it is better to trade faster speed for better precision and reliability.

The technique in Section 2 is then used to match each pixel on camera 1 to a location on camera 2, producing a set of matched feature points. Each set of matched points is then triangulated using the calibrated intrinsic and extrinsic parameters to produce the final 3D object[103].

3.4 Demonstrations

3.4.1 Flatness Accuracy

One of the challenges of claiming high resolution measurements is verifying it with a known test object. We expect the system to produce depth resolution of 80 μm for a disparity error of 1 pixel, so a good candidate test surface would ideally have a much higher accuracy. One of the industry standards for a high performing

structured light system is the ATOS 5 produced by GOM. It lists a max-permissible error (MPE) of $38 \mu\text{m}$ and a typical certification result for VDI-2634 of $26 \mu\text{m}$ over a 0.75m square measurement area[104]. Granite surface plates commonly have surface flatness in this range. We measured a 9×12 " Grade B granite surface plate, with specified root-mean-square (RMS) flatness accuracy of $5.1 \mu\text{m}$. Fig 3.7 shows some sample images of the projected fringes as seen from each camera, as well as an example wrapped and unwrapped phase for vertical fringes as seen from Camera 1.

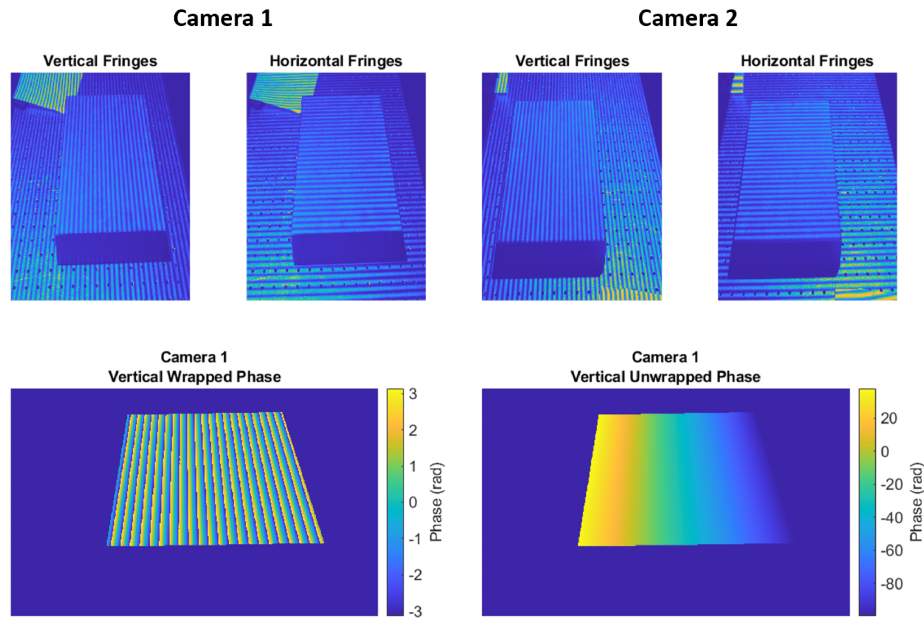


Figure 3.7: Shown are images of the first phase step for horizontal and vertical fringes, seen from both cameras (top). Also shown is a masked image of just the granite surface, with the wrapped phase shown (bottom left) and the unwrapped phase (bottom right). Shown is only the wrapped and unwrapped phase for one fringe direction and for one camera, for simplicity.

Figure 3.8 shows the actual granite surface plate that was measured along with the final measurement using the interpolated stereo matching method, along with the final measured point cloud with plane fit subtracted, which has 1.29 million points and a $5.2 \mu\text{m}$ RMS error. Note that much of the error in Figure 3.8 is high spatial frequency, not low order error, demonstrating the overall shape accuracy of this system. Compared to the theoretical depth resolution of $80 \mu\text{m}$ assuming one pixel of

disparity error, this measurement would imply that the system is capable of subpixel matching up to at least $80\mu\text{m}/5.2\mu\text{m} = 1/15$ pixels. While this measurement is not the same as the certifications used in VDI-2634 for the ATOS 5, it does provide some validation that the overall measured shape of a continuous surface is accurate. The time from beginning of the fringe image acquisition to interpolated reconstructed surface is less than 5 minutes. Most of the measurement time is attributed to image acquisition, requiring 3 second exposures between phase steps due to the large measurement area and the relatively low-brightness of the off-the-shelf projector. The ATOS 5 system advertises up to 0.2 second acquisition times, using a custom high-powered LED or laser projector, but the total processing time is not listed. It is important to note that our developed solution is not designed to produce extremely high speed measurements.

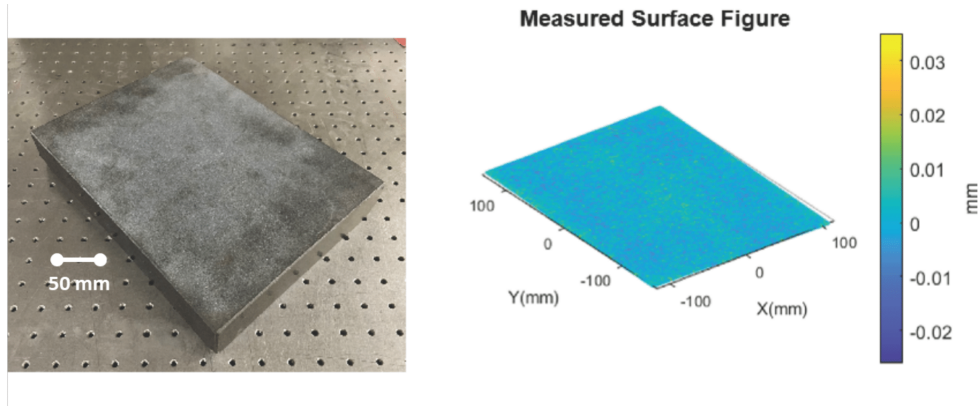


Figure 3.8: Grade B granite surface flat (left) and the measured flat top surface (right). RMS fit error to a plane is $5.1\ \mu\text{m}$.

3.4.2 Highly Specular Machined Surfaces

We also applied this measurement method to measuring the shape residual of a prototype secondary reflector panel designed for the next-generation Very Large Array (ngVLA). The surface was machined on a CNC mill. The surface aperture is hexagonal, 750 mm in the longest dimension. The prescribed low-order shape was not made available, so this example is used to visualize mid- and high-spatial

frequency errors in the surface. The surface was fit to a 5th order XY polynomial and this polynomial was subtracted from the point cloud in order to visualize the higher frequency errors in the surface. The residual has an RMS of $27.8 \mu\text{m}$, which meets the panels accuracy requirement of $40 \mu\text{m}$ RMS, assuming the 5th order shape is correct. The measurement data (shown in Figure 3.9) illustrates the capability of this method to measure beyond the overall low-order shape of a surface, which is often the extent of information provided by other methods like CMMs or laser trackers. In addition, no surface treatment is required, even though the surface has a strong specular component. There is still a small diffuse component, so simply increasing the exposure time to capture more light scattered from the surface from the projector is sufficient. The projector was positioned so that specular reflections from the surface did not enter the camera aperture. Total measurement time is increased due to the required long exposure, but for the application of radio telescope panels, it is still a very small portion of the total manufacturing time and will not become a bottleneck of the process. Small scale structures of tooling marks on the surfaces are easily resolved using this interpolated matching method, which gives insight into how the reflector may perform while focusing high frequency radio waves. This information provides valuable feedback to the effects of different panel manufacturing processes.

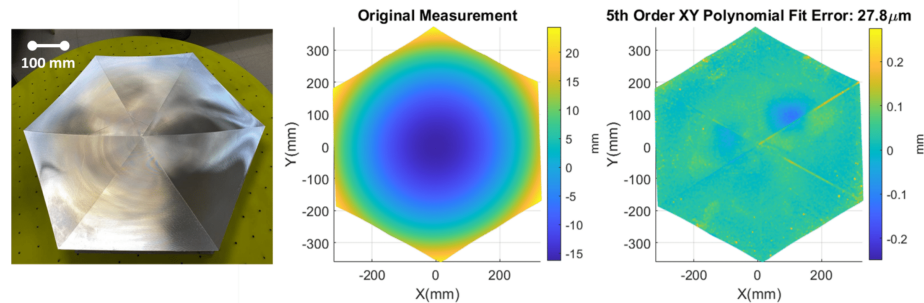


Figure 3.9: Image of hexagonal prototype panel (left), its measurement (middle) and 5th order XY polynomial residuals (right). After subtracting low order shape up to 5th order, errors due to surface machining and support structure are revealed.

3.4.3 Laser Tracker Comparison to LFAST mold

We also applied this measurement method to verifying the accuracy of a convex steel dish that was to be used for slumping the mirrors for the LFAST project discussed in Chapter 2. The measurement was performed on an early-stage mold. The surface is spherical and was originally specified for a radius of curvature of 5.275 m and a circular aperture 34" in diameter. The mold was measured with a laser tracker by a third party company, data report shown below in Figure 3.10. The laser tracker has a 0.001" resolution, or $\sim 25.4 \mu\text{m}$.

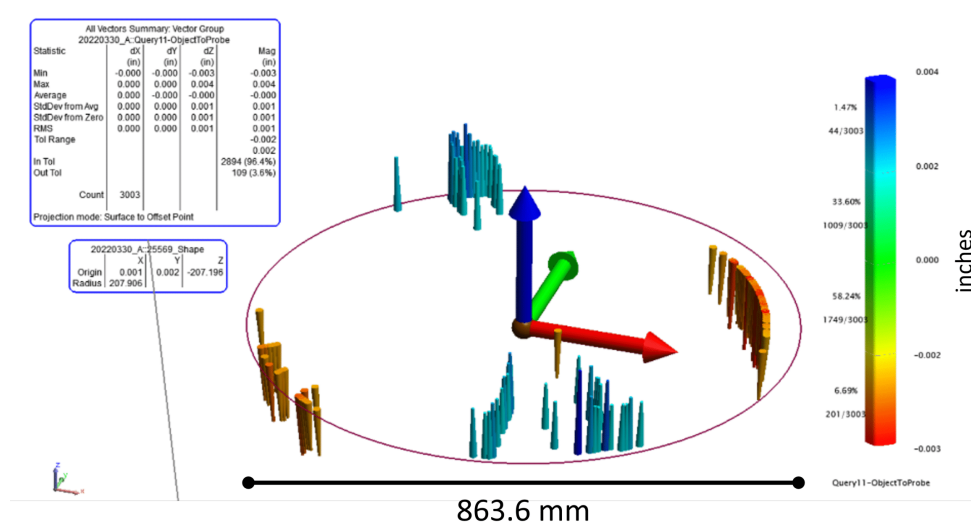


Figure 3.10: Shown is a screenshot of the laser tracker measurement report. The black circle represents the outer boundary of the steel mold surface. The table in the top left shows a summary of the measurement results compared to the ideal 5.275 m radius sphere. The red and blue spikes show the measured points with the largest deviation from the ideal sphere, blue being too low and red being too high. Best fit radius reported was $R = 5.281 \text{ m}$. The blue and red spikes indicate astigmatism in the surface of about $0.007''$, or $175 \mu\text{m}$, peak to valley.

The mold was also measured with the FPP method described in this Chapter and the system shown in Figure 3.5. With the best fit sphere removed from the measurement data ($R = 5.292 \text{ m}$), astigmatism is revealed along with some higher order structure. Compared to the laser tracker measurement, the difference in measured radii is only 0.21%. The fringe projection measurement shows a peak to valley

astigmatism of $183 \mu\text{m}$, on the same order of magnitude as the laser tracker measurement, $175 \mu\text{m}$. Overall, there is much agreement between the well-established metrology method (laser tracker) and the binocular FPP method, especially considering that the laser tracker only reads-out with $25 \mu\text{m}$ resolution. Removing a 2nd order XY polynomial fit (power and astigmatism) from the raw FPP measurement reveals an underlying grid structure, which matches the configuration of steel ribs welded onto the back of the dish, which is the main source of the surface RMS error, after astigmatism. This measurement (Figure 3.11) illustrates the capability of this method to measure beyond overall low-order shape of a surface, revealing other causes of error that is not resolved by the laser tracker measurement, and would not be resolved by a CMM or fiducial-based photogrammetry either.

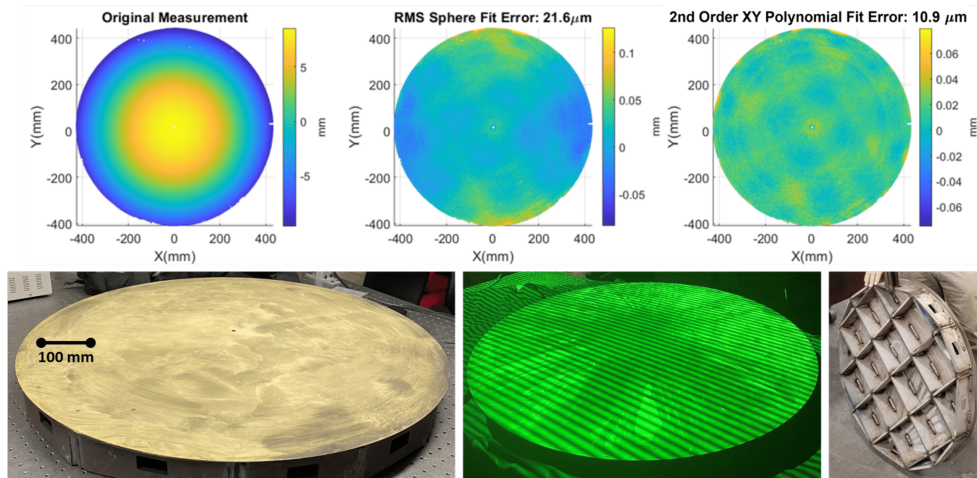


Figure 3.11: Measurements of 863.6 mm steel mold. Shown above is the original measurement (upper left), the sphere fit error (upper middle), the 2nd order XY polynomial fit error (upper right), and images of the measured surface (lower left), projected fringe pattern, and the support structure underneath the surface (lower right). After subtracting low order shape, the underlying rib structure is seen 'printing through' the surface.

3.4.4 Large-Scale Surfaces

We scaled up the system further to measure a 1.8 m x 1.8 m deformable mold that was designed to shape freeform heliostat mirrors and radio telescope panel segments

(Figure 3.12). In order to deform the surface to approach the ideal shape, there is a 18×18 grid of linear actuators (324 total) that can be adjusted, but a measurement of the surface is needed in order to provide feedback. The surface is complicated, with hundreds of square tiles connected with thin blade flexures. At this size, the surface is too large for nearly all portable or permanent CMMs. The same cameras and lenses as in the previous measurement examples were used, but with a 2 m baseline distance and a camera to UUT distance of about 2.5 m.

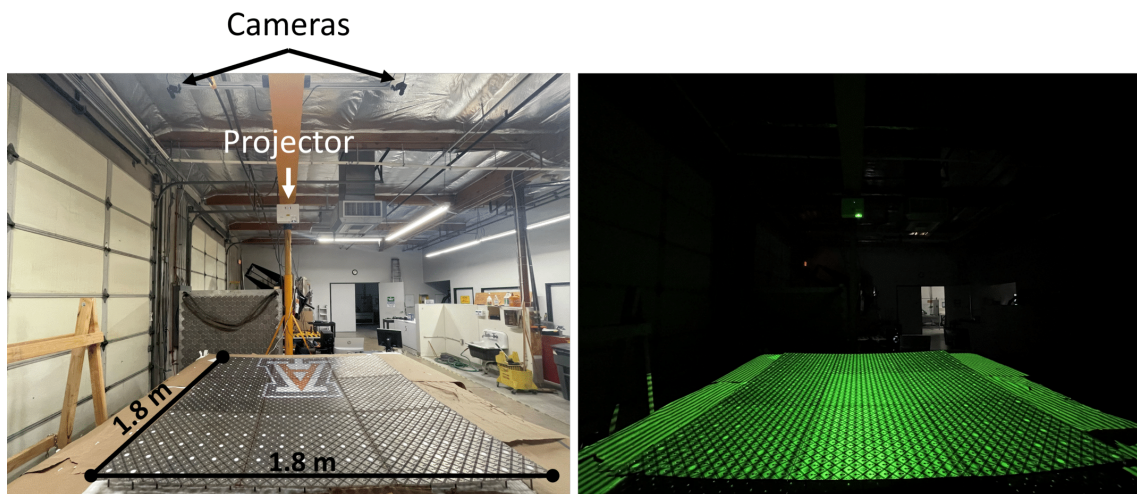


Figure 3.12: Layout of measurement system for 1.8 x 1.8 m adjustable mold (left) and an image of the projected fringes on the surface (right). Camera baseline is 2 m, and distance to the surface is 2.5 m.

Here, the modulation (difference between maximum and minimum brightness at each pixel through the data series of phase shifted fringes) of the phase was used to mask 3D points that were not on the surface. The ideal surface for the adjustable mold is an off-axis hyperboloidal segment, which was subtracted from the measured map to give a residual map. This residual map is crucial feedback for driving the linear actuators that control the mold surface shape and develop this method for shaping metal and glass with a deformable mold. Measurement data from the surface is shown in Figure 3.13.

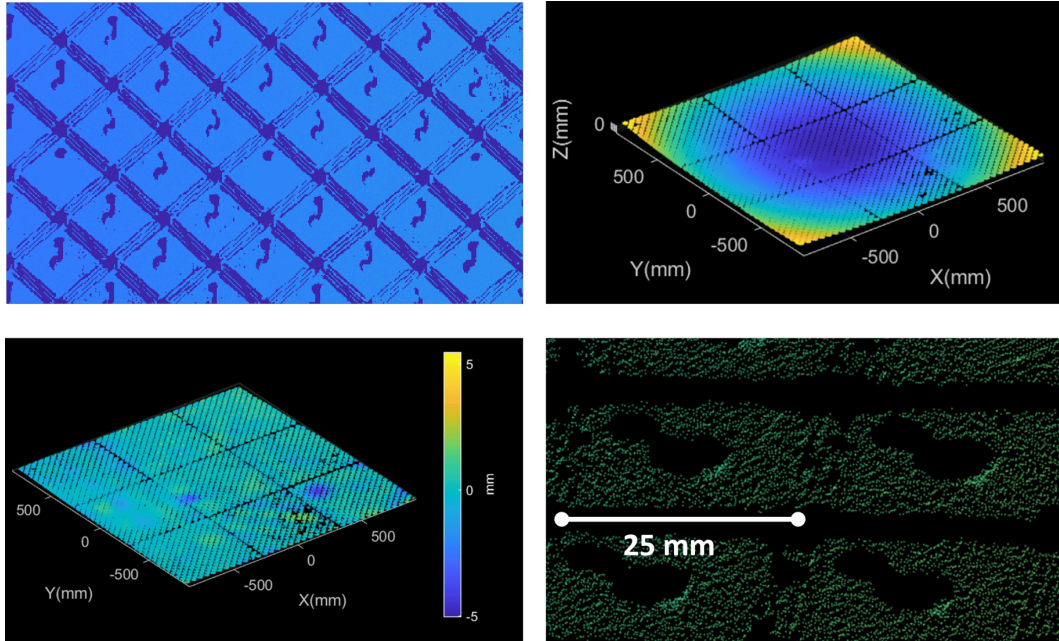


Figure 3.13: Example image used to mask camera images taken of the mold surface (top left) using a modulation threshold to identify pixels that are on the mold surface. 3D map of the raw data with 4.6 million measured points (top right) and a 3D map of the residual with the ideal shape subtracted. Bottom right image is a zoomed in view of the measurement to demonstrate the point density over each 25 x 25 mm square tile.

3.4.5 Repeatability

To verify the repeatability of the system, a 500 x 500 mm concave thermoformed panel was measured 5 times using a binocular FPP system with a 1 meter measurement area, 1.5 m object distance and 1 meter baseline distance. An iterative closest point (ICP) algorithm was used to transform the point clouds to match as best as possible [105]. Since the spatial sampling of each panel is different from different perspectives, each point cloud is resampled with 1 mm spatial sampling, leaving $\sim 200,000$ sample points. I ran five measurements with no image averaging (single captures per each pattern), and analyzed the point to point repeatability. For the applications described in this chapter, it is important to isolate low-order shape repeatability vs individual point repeatability. Each surface was fit to a 5th order XY polynomial, residuals shown in Figure 3.14. Figure 3.15 shows the point to point

repeatability histogram for each measurement with the 5th order fit removed as well as the point to point repeatability histogram of the 5th order fit. The average point to point repeatability for the residual is $3.4 \mu\text{m}$ and $1.2 \mu\text{m}$ for the best fit 5th order polynomial across the five measurements.

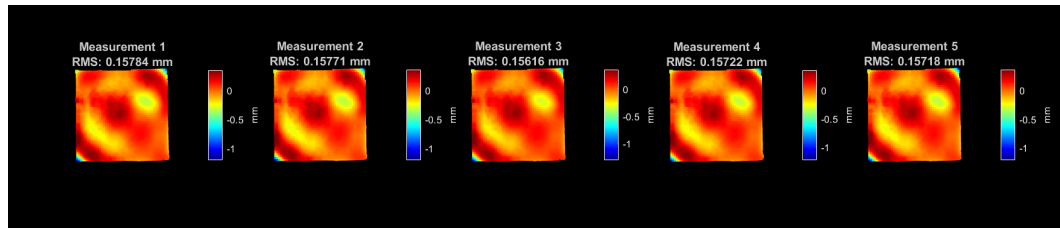


Figure 3.14: Residual surface error from a 5th order XY polynomial fit for each of the five measurements.

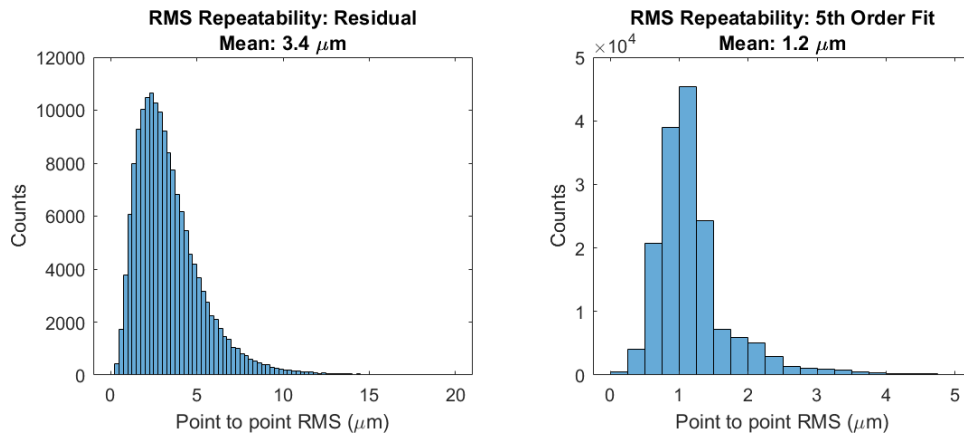


Figure 3.15: Point-to-point RMS repeatability histograms shown for the panel residual (left), as well as for the best fit 5th order polynomial (right). Each value on the histogram is the RMS calculated for a single point across each of the five measurements.

3.5 Discussion

This method provides a variety of advantages over other types of 3D surface profiling systems. The accuracy over a 9" x 12" granite flat is much better than commercial FPP systems [79, 104], which often specifies accuracy on the order of 0.025 mm, and is comparable or better than the metrology methods used to measure rough

surfaces based on measurement time, accuracy, flexibility, and spatial resolution. While the total measurement and processing time is slower than other commercial FPP systems, the method described in this paper has not yet been optimized with custom hardware, in the form of brighter projectors, more processing power, and faster cameras. This FPP method can measure millions of points across a square meter, making the spatial resolution on the order of 1 mm^2 . Because CMMs and laser trackers only measure a single point at a time, a comparable spatial resolution measurement would take many weeks of constant sampling, assuming a few seconds for each sample point. An IR interferometer may have similar spatial resolution by viewing the surface with a high resolution IR camera, but measurements require a unique configuration for every type of surface shape.

This FPP method is capable of measuring any continuous surface that can be simultaneously seen by both cameras and the projector, allowing for a wide range of convex, concave, and freeform surfaces. As a result, this system can be used for a variety of projects beyond radio telescope fabrication including but not limited to glass shaping for heliostat mirrors, optical table flatness measurements, and damage analysis. Calibration of the system is simple and well-established, and can be done with a standard checkerboard pattern, compared to other FPP methods that may require extra steps for projector calibration. The method is also tolerant to errors in the projector. Since the projector acts simply as a fiducial generator, phase errors due to gamma brightness distortion and temporal brightness variation are common to both cameras, which have negligible affect on the ability to match features, and ultimately allows retrieval of accurate point measurements. The hardware cost of the system is low, requiring only off-the-shelf machine vision cameras, a gaming projector, and a computer: far less than the cost of comparable CMM, laser tracker, or IR interferometer. These properties make it a valuable, flexible method for use in the development of new surface forming techniques.

3.6 Comments on limitations and paths for future developments

There are many commercial FPP systems on the market today, from ATOS to EinScan to Hexagon. Commercial systems have benefited from years of research to make their FPP systems faster, more robust to noise, and more user friendly. The FPP system described in this chapter, while producing data that is more accurate than these commercial systems, suffers more from environmental conditions, speed, and ease of calibration. This section aims to discuss some of the shortfalls of the developed FPP system, and where improvements can be made to make it truly compete with commercial systems.

3.6.1 Calibration

One drawback of this system is it is difficult to get feedback on a poor measurement or calibration, and establish a ground truth measurement. Reprojection errors in the calibration generally aren't relied upon for verifying a good calibration. Calibration of the intrinsic and extrinsic parameters can be easily skewed by distortion in the checkerboard printing process, warping of the calibration board, camera intrinsics changing with temperature, and limitation in depth of focus resulting in uncertainty of detected checkerboard points. Commercial FPP systems typically use a long rod made of metal or carbon fiber with fiducials with a known separation as a system calibration method. While this may suffice for measurement of commercial objects, the FPP system described in this chapter aims to reach higher precision over large areas. This system is being used to measure not just small structural features in the radio telescope reflector panels, but also their overall low-order shapes e.g. astigmatism, coma, trefoil etc. To truly verify that the system is delivering accurate surface shape data, a measurement of a known object should be performed that covers the entire measurement area. While we showed in this chapter the 9" x 12" granite surface plate met specifications, the FOV of the entire measurement area is more than triple the size of that piece of granite. Granite surface plates only come off the shelf in sizes 48"x36", roughly 1 m^2 . For a FPP system with a 2 x 2 meter

FOV, a granite plate of this size could be traversed to each quadrant of the FOV and measured in order to verify flatness. This ground-truth verification method does not scale to larger areas. This ground truth is used to verify that the intrinsic and extrinsic parameters being used to triangulate 3D points is still valid, however, if the intrinsic and extrinsic parameters are constantly being probed for accuracy, this could replace the ground truth measurement. Methods utilizing auxiliary sensors to calibrate cameras with long baselines and large FOVs could be used[106, 107], but would likely need some adaptation for higher accuracy. For areas larger than 2 x 2 meters, a sensor-aided method is likely the best method to verify system calibration.

3.6.2 Measurement Speed

Cameras

The FPP system in this chapter takes minutes to perform data acquisitions, but commercial systems typically quote seconds. This is for a number of reasons. First, commercial FPP systems use global shutter cameras which allow for easier synchronization of camera captures. We have used rolling shutter cameras due to their lower cost, but at shorter exposure times the sensors suffer from artifacts caused by the rolling shutter and frequencies from external lighting. Similar to the framerate of a camera matching the rotation rate of a helicopter blade: it produced incorrect and unrepeatable errors from image to image. This limits the cameras to using longer exposure times to avoid this artifact. Switching to global shutter cameras would alleviate this problem.

Projector

The other limitations are related to the projector. Since we are using an off-the-shelf projector, we must use Java images in order to splash the fringe patterns to the projector display. The projector also works in a rolling shutter fashion, writing current values to pixels one row at a time with a fixed 60 Hz framerate. Switching to global shutter camera would solve the rolling shutter artifact, but not the projector

rolling display artifact when used with short exposures. Projectors that are delivered as an application development kit are needed to solve these problems: where the digital micromirror device (DMD) can be directly controlled to hold a fixed position during captures, and load images from flash memory more quickly.

Brightness of off-the-shelf projectors also limit this measurement method. For large, specular, or black objects, longer exposures are needed to capture images with high SNR for reliable phase unwrapping. For very dark objects over a 2 x 2 meter FOV (for example in the system shown in Figure 3.12) the required exposure time for each image is a few seconds. Since 10s of images are required, this results in an acquisition time that takes minutes.

3.6.3 Robustness to the environment

Currently, all measurements are performed with room overhead lights turned off. This allows for the shortest possible exposure time without saturating the camera sensors due to light sources other than the projector. Many commercial systems utilize a projector with a customized wavelength and matching bandpass filters for the cameras. This blocks a majority of the light from overhead light sources from reaching the cameras, while allowing the light from the projector to pass. In commercial systems, this allows for measurements to be performed with the lights on, which is not only convenient but additionally avoids safety risks related to unlit factory spaces. Future work will aim to add this feature to the system.

3.6.4 Summary

While the FPP system described in this chapter is a very useful research tool for SOSL, there is still many improvements to be made in calibration, speed, and robustness. Most of these improvements can be solved by spending more money on higher-performing hardware, and some need to be solved with continued research. The software that runs the FPP system has been licensed from Tech Launch Arizona to Fringe Metrology LLC (founded by the author of this dissertation). Fringe

Metrology LLC aims to continue this research to address these improvements both by improved hardware and system research and development.

CHAPTER 4

Systematic Radio Telescope Alignment using Portable Fringe Projection Profilometry

This chapter is a summary of an article submitted to Springer *Nano-manufacturing and Metrology*, Appendix D.

4.1 Motivation

As with the previous chapter, this chapter deals with the construction of radio telescopes, but at the dish level rather than the panel level. Radio telescope panels can be measured individually in a laboratory or factory environment, but radio telescope dishes are designed to exist outdoors and operate under regular weather conditions. Unlike optical telescopes (LFAST is the exception), radio telescopes are almost always constructed without a protective dome. As a result, they are exposed to the elements: temperature fluctuations from day to night and from season to season, wind, and varying gravity deformation as the telescope slews in elevations. Just like the segmented ELTs described in Chapter 2 (GMT, TMT, E-ELT), radio telescope dish surfaces are also segmented and need cophasing, or alignment. While the alignment tolerances for a radio telescope are much looser than optical telescopes, radio telescopes typically have more segments to align for a single dish, and many more than one dish to align, sometimes in the hundreds like for ngVLA and SKA. Most radio telescopes do not have motorized actuators, so panel adjustment is done manually. It often takes many iterations of metrology and adjustment to achieve the desired dish accuracy. Due to the highly manual process, it is imperative that metrology is done right to avoid long cycle times of alignment per telescope.

As shown in the Introduction Figure 1.3, surface accuracy is a critical process to deploying a radio telescope to meet optimal gain. This is true for the entire

dish not just the individual panels. Manufacturing cost associated with making accurately-shaped panels is wasted if not properly aligned. If the status of panel to panel alignment and panel deformation is not known, then adjustments cannot occur.

Another goal of the NSF grant for rapidly manufacturing radio telescope panels (discussed in Chapter 3) is to build a demonstration radio telescope. SOSL planned to make 26 0.5 x 0.5 meter panels to form a $\sim 2.4 \times 3.2$ m dish. The team planned to use an existing altitude-azimuth pedestal that was donated to UArizona Chris Walker in 1991[108] to build a radio telescope for student use. University of Arizona senior design team (SDT) 21039 was tasked with redesigning the dish framing and surface for reconstruction, named the Student Radio Telescope (SRT), with the 3D rendering shown in Figure 4.1. The SRT is designed to be a demonstration telescope for the new panel thermoforming method. As the team began to produce prototype panels for mounting on the SRT, we ran into the same problem as any radio telescope: aligning the panels to each other. This chapter describes some existing methods to align radio telescope panels, and covers their drawbacks. We then present using the same FPP method described in Chapter 3 as a solution to this problem. We demonstrated using this method by aligning two panels that were mounted to the SRT.

4.2 Other methods for dish alignment

Common methods to measure panel alignment and shape have historically included photogrammetry[11, 12, 13, 14], holography[15, 16, 17, 18] and laser trackers or laser trusses[13, 19, 20, 21]. Oftentimes, a combination of methods is used.[13, 22, 23, 24] All of these methods deliver the information on the surface accuracy of a dish, but they have many fundamental limitations and drawbacks. The spatial sampling of photogrammetry and laser trackers is limited to the number of fiducials or manually scanned points. The manual nature of these methods makes them time consuming and expensive, requiring large teams of researchers to execute the metrology.

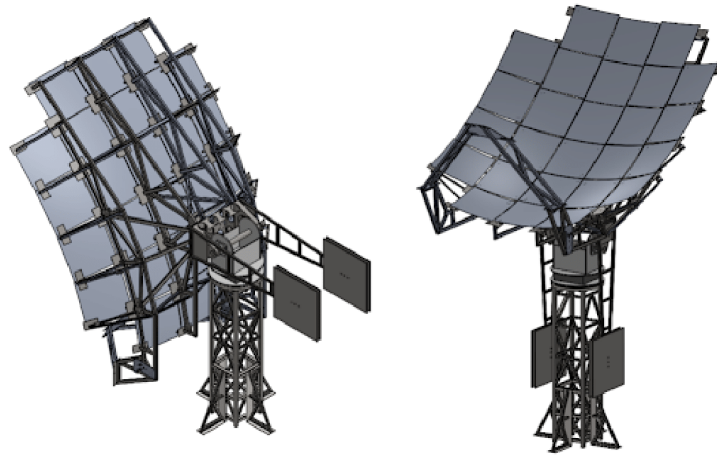


Figure 4.1: 3D rendering of the Student Radio Telescope. The telescope will be made up of 26, 500 mm x 500 mm panels, each with a different shape due to the off-axis paraboloid design.

The University of Arizona recently tuned the alignment of dish panels in a 12 m diameter radio telescope using photogrammetry. It required a team of 3 (scientists and engineers) to work for two weeks. At a similar rate, it would take years to align all of the planned ngVLA dishes, even with multiple teams. The accuracy of these methods also degrades with working distance, so as aperture size increases, the depth resolution decreases. For extremely large apertures observing with millimeter wavelengths, holography has been the default method to measure reflector deformations. Holography utilizes a smaller dish (that is assumed to be perfect) pointed at a satellite beacon (typically a geosynchronous satellite to avoid the need for tracking) as a reference signal. The antenna under test and the reference antenna raster scans across the source to sample the beam.[109, 110] Correlations with the reference signal are used to recover the absolute phase errors and inverse Fourier transforms are used to recover the aperture wavefront error, which feeds back to required surface adjustments to make corrections. While holography is known to have great sensitivity, it is limited in logistics. Specialized cryogenic detectors designed to match the frequency of the geosynchronous satellite beacon are required to take measurements. Also due to the use of geosynchronous satellites, only one elevation

angle can be tested, meaning gravitational deformations at other elevation angles remain unknown. The measurements are time consuming due to the need to raster scan the entire telescope to sample the beam, and good environmental conditions are required for successful measurements. The algorithms to determine adjustments on the primary reflector vary largely from telescope to telescope depending on the size, on-axis versus off-axis configuration, as well as the presence of secondary or tertiary reflectors. Many future plans for large radio telescopes involve multiple off-axis reflectors[111, 112, 113, 114]. It is clear that no matter what current metrology method is used on a radio antenna dish, there are drawbacks in cost, time, logistics, and data quality. Oftentimes, the use of multiple methods is required.

We adapted the FPP method described in Chapter 3 to make it portable, function outdoors, measure discontinuous objects, and cover large areas with high resolution. As a demonstration, we will show in this paper how the system can be used to deliver alignment feedback information for two adjacent panels on the SRT. For background on the binocular FPP method with subpixel feature matching, please refer to Chapter 3 for more details.

4.3 Methods

4.3.1 Binocular Fringe Projection Profilometry with Hierarchical Unwrapping

The previously described method does not work for discontinuous surfaces, as the spatial phase unwrapping for a single frequency only produces relative phase, not absolute phase, as was discussed in Chapter 3 Eq. 3.3. Previously, we would solve this problem with a spatial phase unwrapping method, and adjust the phase of each map by finding the average nearest integer multiple of 2π for each phase map, and applying a constant phase shift. However, this only works for continuous objects, like individual panels. For multiple objects, there is an integer multiple of 2π phase ambiguity, for example two adjacent panels in a radio telescope, when using a spatial phase unwrapping method. To ensure reliable and absolute phase unwrapping, we

have implemented a temporal phase unwrapping technique known as hierarchical, or multi-frequency, phase unwrapping[115]. The method uses an initial low frequency fringe period such that less than one period covers the entire span of the projected area, and thus has no 2π phase ambiguity. Consecutively higher and higher frequencies are used, with the lower frequency used to unwrap the next highest frequency, as in Eq. 4.2.

$$k_n(x, y) = \text{Round}\left(\frac{\frac{\lambda_{n-1}}{\lambda_n}\phi_{n-1}(x, y) - \phi_n(x, y)}{2\pi}\right) \quad (4.1)$$

$$\Phi_n(x, y) = \phi_n(x, y) + 2\pi k_n(x, y) \quad (4.2)$$

In Eq 4.1, n indicates the frequency being used, from lowest to highest. $k_n(x, y)$ is the map of fringe orders used to unwrap $\phi_n(x, y)$ to create the unwrapped map, $\Phi_n(x, y)$, for fringe period λ_n . The process of Eq 4.1 and 4.2 is done iteratively until the final highest frequency, or shortest fringe period, is reached. We used 5-step phase shifts for each fringe period of 1920, 500, 100, and 10 pixels. Fringe period 1920 matches the widest screen dimension for 1080P projectors, producing no unwrapping ambiguity. In theory, only the lowest frequency and the highest frequency are needed, but in the presence of noise and imperfect fringe patterns, using multiple frequencies helps ensure proper identification of fringe orders for unwrapping each consecutive frequency[86]. There is much research into optimal selection of fringe periods to reduce the number of required frequencies, but it is highly dependent on the configuration[116]. Since our application is not dependent on highly rapid measurements, it is more important to guarantee high quality data than to improve measurement speed by small amounts.

4.3.2 Dish Measurement with Global Reference Frame

As mentioned in the Introduction, this stereo camera FPP system returns 3D data points relative to one of the camera axes. This is sufficient to align panels to one another to make the smoothest surface, but this surface needs to focus incoming

radio signals to a known position. The SRT is an off-axis paraboloidal design, with a direct feed. To ease the process of determining a global reference frame, two circular fiducials are included in the FPP measurement field of view of SRT to define the optical axis of the telescope: at the paraboloid vertex and at the desired focal point.

These two fiducials will also be identified and triangulated in the stereo camera system, returning two 3D points relative to camera 1: $P_{vertex} = (X_{vertex}, Y_{vertex}, Z_{vertex})$ and $P_{focus} = (X_{focus}, Y_{focus}, Z_{focus})$. Their centers are identified using the Hough transform[117, 118]. We perform the following coordinate transformations to orient the measured panels ($\mathbf{P}_{panel} = (\mathbf{X}_{panel}, \mathbf{Y}_{panel}, \mathbf{Z}_{panel})$) with the optical axis and paraboloidal equation, and extract the required rigid body motions for each panel for lowest RMS surface error.

1. Translate the entire map to locate P_{vertex} at the origin.

$$\begin{aligned}\mathbf{P}'_{panel} &= \mathbf{P}_{panel} - P_{vertex} \\ P'_{focus} &= P_{focus} - P_{vertex}\end{aligned}\tag{4.3}$$

2. Calculate Euler angles α and β of the line connecting the vertex and the focus.

$$\begin{aligned}\alpha &= \arctan\left(\frac{Z_{focus}}{X_{focus}}\right) \\ \beta &= \arctan\left(\frac{Z_{focus}}{Y_{focus}}\right)\end{aligned}\tag{4.4}$$

3. Calculate rotation matrix using Euler angles from the coordinates of the measured focal position

$$\mathbf{R} = \begin{bmatrix} \cos(\beta) & \sin(\alpha)\sin(\beta) & \cos(\alpha)\sin(\beta) \\ 0 & \cos(\alpha) & -\sin(\alpha) \\ -\sin(\beta) & \sin(\alpha)\cos(\beta) & \cos(\alpha)\cos(\beta) \end{bmatrix}\tag{4.5}$$

4. Apply rotation matrix to each panel point cloud and focus point

$$\begin{aligned}\mathbf{P}''_{panel} &= \mathbf{R}\mathbf{P}'_{panel} \\ P''_{focus} &= \mathbf{R}P'_{focus}\end{aligned}\tag{4.6}$$

5. Compare ideal paraboloid (radius R) to each panel

$$Z_{ideal}(X, Y) = r^2/(2R) = (X^2 + Y^2)/(2R) \quad (4.7)$$

$$\mathbf{Z}_{residual}(X, Y) = Z_{ideal}(\mathbf{X}''_{panel}, \mathbf{Y}''_{panel}) - \mathbf{Z}''_{panel} \quad (4.8)$$

6. Fit residual XYZ points of each panel to a plane

$$A\mathbf{X}''_{panel} + B\mathbf{Y}''_{panel} + C\mathbf{Z}_{residual} + D = 0 \quad (4.9)$$

7. Calculate piston, tip and tilt from plane-fit coefficients

$$\delta Z = D$$

$$\theta = \arctan(C/A) \quad (4.10)$$

$$\phi = \arctan(C/B)$$

The metrology process is set up to automatically deliver the required tip, tilt, and piston at the end of each measurement. Each panel has 4 actuators in each corner of the panel, separated by 400 mm, as shown in Figure 4.2. Eq 4.11 shows how to convert the tip, tilt and piston to actuator number of rotations using the angle approximation of $\theta \approx \frac{s}{r}$. Once of the number of mm of translation is determined, the threads per inch (TPI) of the actuators is used to convert to number of rotations.

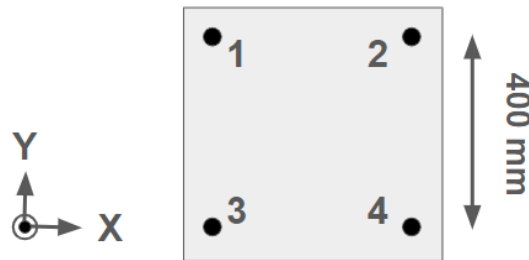


Figure 4.2: Coordinate system and actuator layout for each panel. Once tip, tilt, and piston values are extracted, they need to be converted to actual numbers of rotations on the actuators.

$$\begin{aligned}
\mathbf{1} & : (0.5\theta\delta S + 0.5\phi\delta S + \delta Z) * TPI/25.4 \\
\mathbf{2} & : (-0.5\theta\delta S + 0.5\phi\delta S + \delta Z) * TPI/25.4 \\
\mathbf{3} & : (0.5\theta\delta S - 0.5\phi\delta S + \delta Z) * TPI/25.4 \\
\mathbf{4} & : (-0.5\theta\delta S - 0.5\phi\delta S + \delta Z) * TPI/25.4
\end{aligned}
\tag{4.11}$$

4.4 Experimental Setup, Calibration, and Configuration

4.4.1 Hardware

The hardware for this system utilizes two FLIR Blackfly S USB 3 machine vision cameras with Sony IMX183 sensors (20MP 5472x3638, with 2.4 μm pixels), each with a Computar V0826-MPZ lens (8 mm focal length). Each camera is mounted to the ends of a 0.8 m length 8020 aluminum extrusion. The 8020 is mounted to a tripod for portability and pointing. With this setup, the entire 3.2 m dish can be seen from a 3-meter distance. We utilized an off-axis short-throw 1080P projector from BenQ (Model MW817ST), that can cover the entire surface from 1.5 meters away. The software to capture the images, process the fringe patterns, calculate the unwrapped phases, match the phase pairs, and triangulate the matched pairs to produce the 3D point clouds is written in MATLAB. Photos of the camera and projector hardware are shown in Figure 4.3.



Figure 4.3: Left, one of the two FLIR Blackfly USB3 cameras with 8 mm focal length lens. Center, both cameras mounted to 8020 aluminum extrusion, mounted to a tripod. Right, BenQ 1080P short-throw projector used in this experiment.

4.4.2 Calibration

Calibration of the stereo camera pair was performed indoors for easier control of lighting and environmental conditions. A checkerboard calibration board made of aluminum and low-density polyethylene (LDPE) with size of 800 mm x 600 mm and square size of 30 mm was used. The calibration board was mounted to a tripod and traversed through the overlapping FOV at the 3-meter working distance for a set of 20 images. An example of one of these images is shown in Figure 4.4. Using the detected checkerboard corners on each sensor, each camera was calibrated individually for intrinsic parameters, then the pair was calibrated together for extrinsic parameters, keeping the intrinsic parameters fixed. The calibrated intrinsic and extrinsic parameters are shown in Table 4.1.

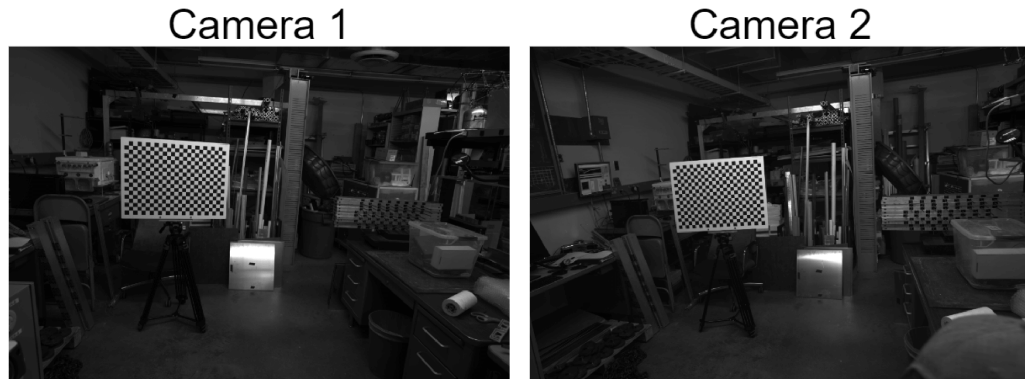


Figure 4.4: An example image from the 20-image set used to calibrate the intrinsic and extrinsic parameters of the stereo camera pair. The checkerboard was moved throughout the overlapping FOV in order to properly calibrate for radial distortion.

4.4.3 Measurement Setup

As described in Section 4.3.2, fiducials are placed at the paraboloid vertex and the telescope focal plane for defining the optical axis. These were roughly located using dimensions from the SRT CAD files. We used 1.0" white stickers placed in the middle of 1.5" black stickers as these fiducials for reliable contrast for circle detection

Table 4.1: Calibrated stereo camera parameters.

Property	Camera 1	Camera 2
Focal Length (mm) f_x, f_y	8.25 mm, 8.25 mm	8.25 mm, 8.25 mm
Principle Point (pixels) u_x, u_y	2745, 1820	2750, 1843
Radial Distortion (r_2, r_4, r_6)	-.100, .126, -.043	-.096, .115, -.033
Extrinsic Matrix $\begin{bmatrix} \mathbf{R}_{3 \times 3} & \mathbf{t}_{3 \times 1} \\ \mathbf{0}_{1 \times 3} & 1 \end{bmatrix}$	$\begin{bmatrix} 0.926 & 0.061 & -0.373 & 801.048 \\ -0.072 & 0.997 & -0.014 & -40.332 \\ 0.371 & 0.039 & 0.928 & 170.496 \\ 0 & 0 & 0 & 1.0000 \end{bmatrix}$	

with the Hough transform. Figure 4.5 shows the physical locations of the fiducials with respect to the rest of the telescope structure as well as the two adjacent panels to be aligned.

Measurements of the SRT are performed at night in order to increase the SNR of the projected patterns relative to ambient lighting. We also aimed for a night with low to no wind to reduce temporal errors associated with telescope structural bending or vibration. To avoid boosting noise in the images, the cameras were used with a gain of 0. To utilize the full dynamic range of the camera bit-depth, a 5-second exposure was used for each camera. We employed 4 frequencies for the hierarchical phase unwrapping method, where we used the N-step phase shifting algorithm[84] for each frequency and each phase shifting direction (horizontal and vertical) to retrieve the wrapped phase maps. Equations 4.2 and 4.1 are used to calculate the four unwrapped phase maps (two for each phase shifting direction, for each camera). This results in a 40-image pattern sequence (4 frequencies, 5 phase steps, 2 directions). Each pattern was captured 3 times and averaged to further eliminate noise, resulting in a 600-second (10-minute) acquisition time. Figure 4.6 shows an actual data acquisition in progress at night.

Once a measurement is made, the rigid body motions for each panel are extracted using the process described in Section 4.3.2, and each panel is adjusted using the 4 manual actuators located in the corners of each panel. The actuators have 1 mm

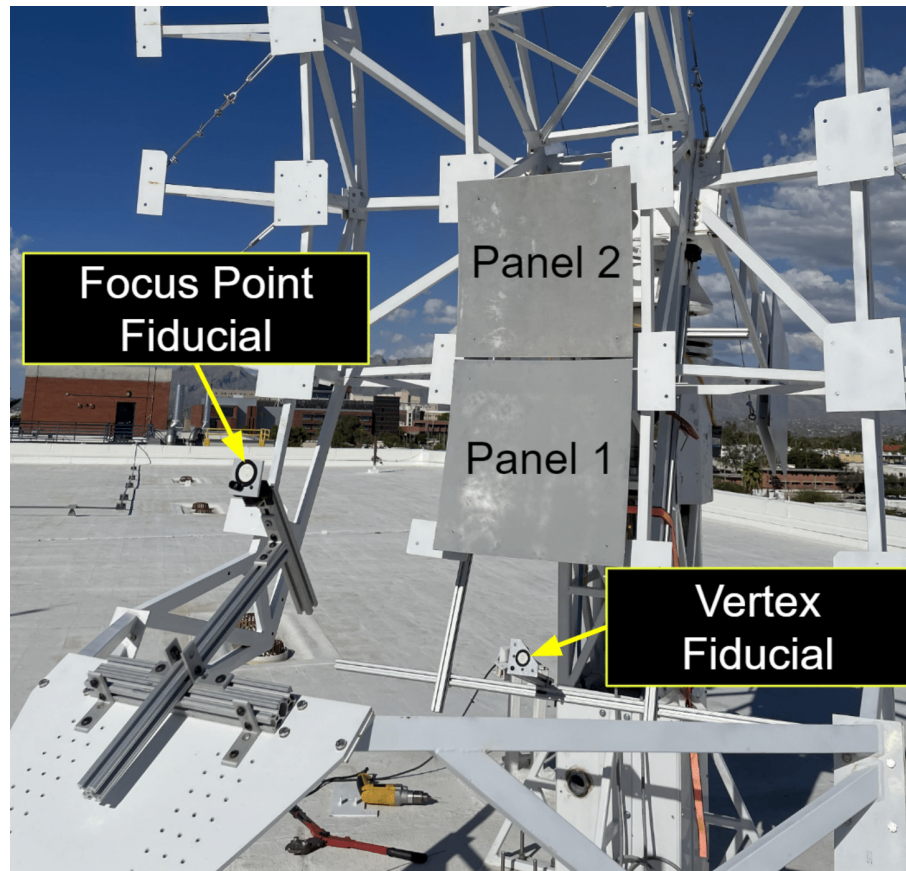


Figure 4.5: Layout of the telescope structure. Two fiducials are placed where the paraboloid vertex and focus should be using 8020 extrusions. An example panel 1 and panel 2 are installed on the telescope. They are the bottom two rows of the center column of panels.

thread pitch and are separated by 400 mm. Using Eq.4.11 returns the required number of turns for each of the 4 actuators for each panel. After an iteration of adjusting tip, tilt, and piston is performed, the panels are then remeasured and the adjustment process is repeated until the remaining errors are satisfactory.

4.5 Results

Figure 4.7 shows an example set of horizontal and vertical phases from the perspectives of camera 1 and camera 2. Each pixel on each panel in camera 1 has a unique

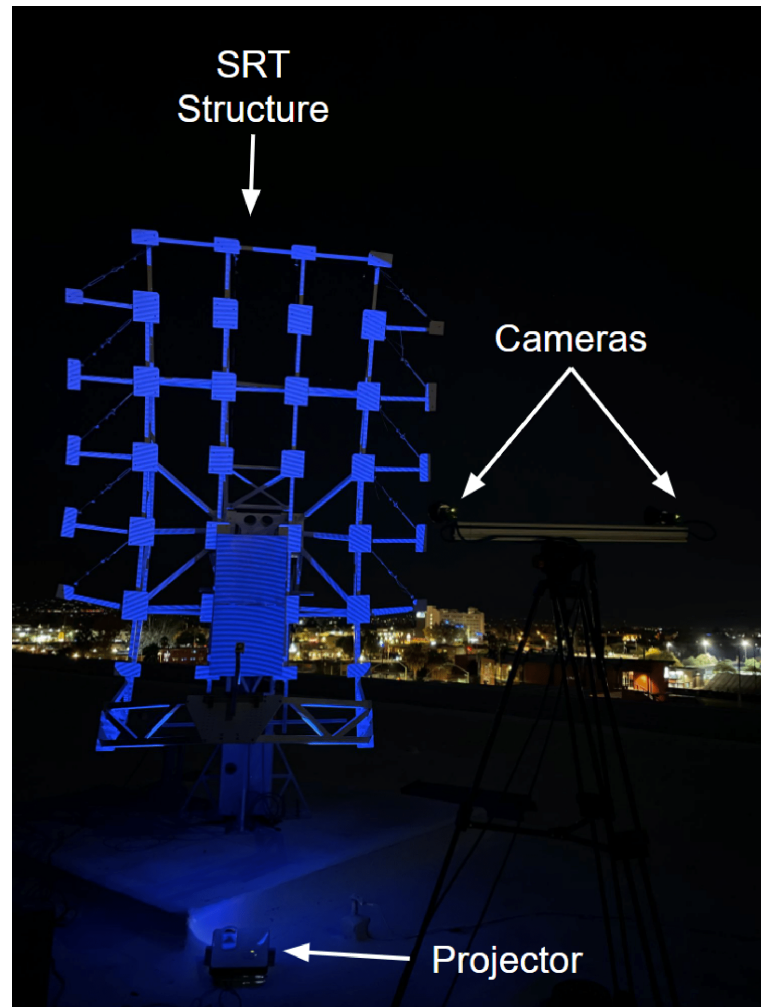


Figure 4.6: Nighttime measurement setup. The projector is placed near the telescope and utilizes the short-throw to cover the entire dish. The tripod carrying both cameras is placed roughly 3 meters away from the dish and positioned such that the entire dish can be seen in the field of view of both cameras. Shown in the image is the 10-pixel period frequency projected onto the dish structure.

combination of horizontal and vertical phase. The camera 2 phases are searched for a matching phase pair for each pixel on camera 1. The resulting matched locations on each camera detector are triangulated using the calibrated parameters from Table 4.1. Figure 4.8 demonstrates the data produced by the system described in this paper. Figure 4.8a shows the data returned from the software in its raw format,

with the locations of the cameras, paraboloid vertex, focus, and point clouds of both panels. Using steps 1-4 from 4.3.2 yields Figure 4.8b to align the optical axis of the telescope with the z-axis. Steps 5-6 are done for each panel to produce the piston, tip, and tilt error for each panel. Figure 4.9 shows the best fit plane to panels 1 and 2 before adjustments begin and Table 4.2 shows the actual starting piston, tip and tilt values.

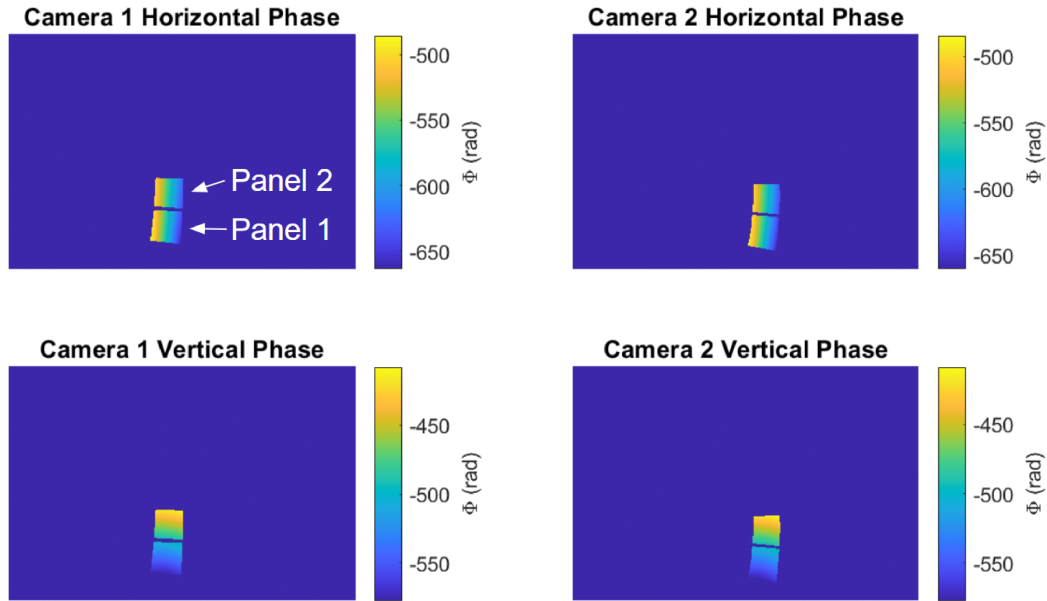


Figure 4.7: Images from each camera are masked to isolate the two panels being measured. The phase unwrapping process produces four images: horizontal and vertical phase for each camera. These maps are used to find matching object locations from pixels on camera 1 to locations on camera 2.

Table 4.2: Results before the first adjustment iteration.

Property	Panel 1	Panel 2
δZ	-0.70 mm	10.46 mm
θ	0.757 deg	0.80 deg
ϕ	-0.54 deg	-3.15 deg

Besides the rigid body errors, each panel has imperfections compared to the ideal

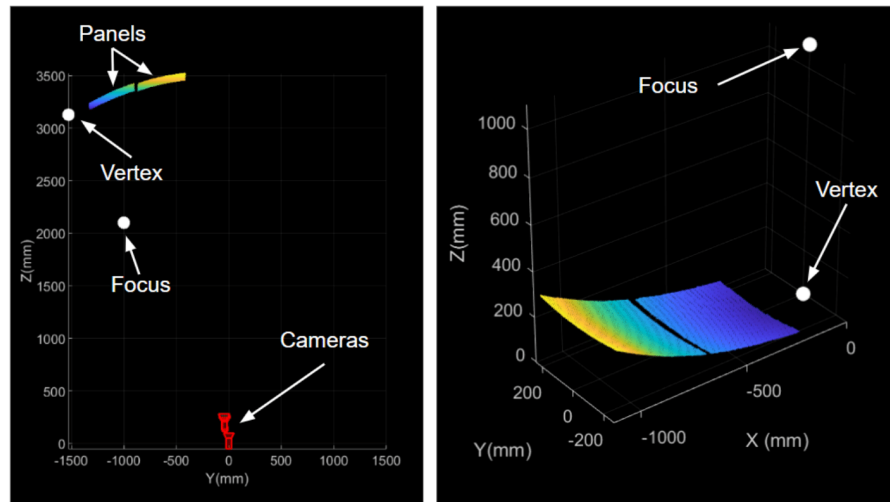


Figure 4.8: Each FPP measurement results in a point cloud for each panel, and the relative location of both the vertex and the focus. Raw data is shown on the left. The triangulated 3D points are produced relative to the coordinate system defined by camera 1. Matrix rotations and translations are applied to the panel point clouds to align the optical axis with the z-axis, shown on the right. In this configuration, the panels can be directly compared to Eq. 4.8 to extract the residual error in the panels, as well as the rigid body alignment error.

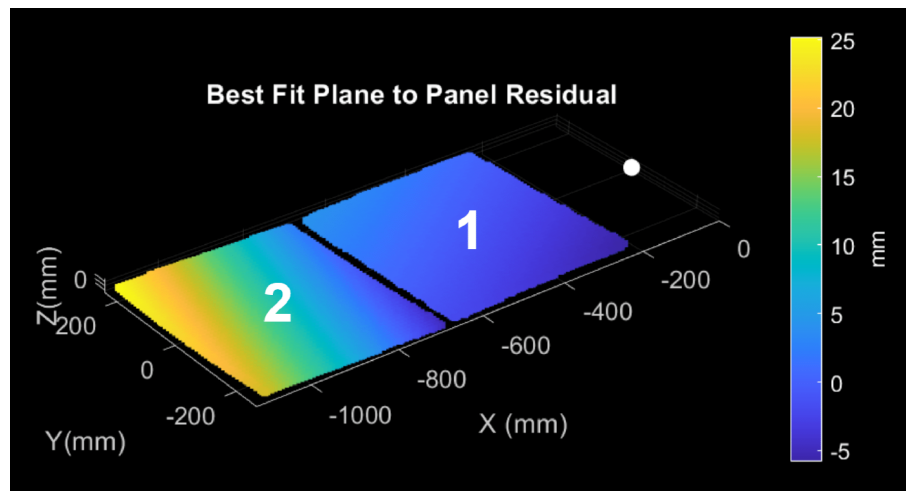


Figure 4.9: Best fit planes for each panel, including piston.

shape. Figure 4.10 shows the residual from the ideal paraboloid for each panel with tip, tilt, and piston errors removed. Panel 1 has a 1.28 mm RMS, and Panel 2 has a 0.81 mm RMS. These are not actual panels that will be used in the telescope, but are examples used for this initial alignment test. For this experiment, the panel actuators on SRT are not capable of reliable shape correction; however, the system delivers information that could be used to do so on most other large radio telescopes. The goal of the adjustment process is to make the dish surface accuracy limited by the individual panel accuracy, not the rigid body errors.

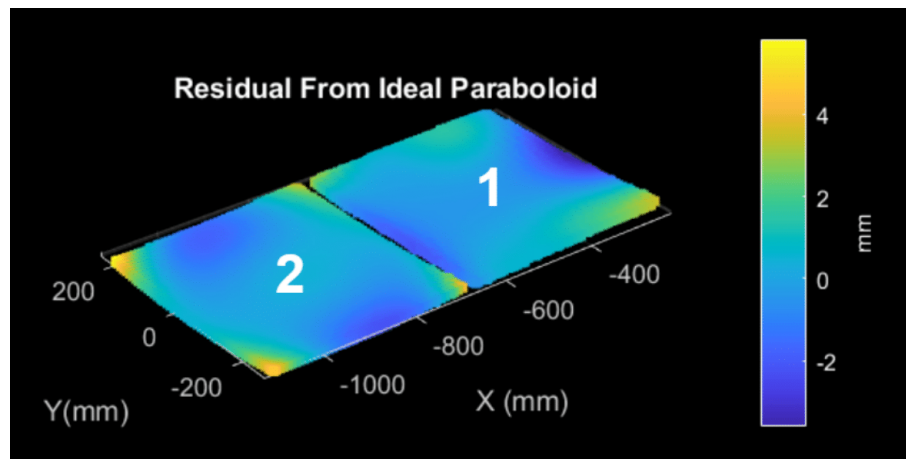


Figure 4.10: In addition to finding the rigid body motion error of each panel, the system also has enough resolution to map the surface errors of each panel compared to their ideal shape. Shown here are the residual surface maps compared to the ideal paraboloid.

We performed 4 measurements with 3 adjustment iterations. Within 3 iterations, piston error was reduced to < 0.25 mm and tip/tilt was reduced to < 0.1 degrees. The final panel RMS including alignment errors was 1.325 mm and 0.842 mm for panel 1 and panel 2, respectively. Collectively, the two panels make a small dish with 1.12 mm RMS error. Looking back at the plot of the Ruze equation in Figure 1.3, this error would make the dish capable of observing 2 cm wavelengths (15 GHz) with less than 50% loss. Most of the error in this test is attributed to panel shape, which the actuators for this telescope are not configured to correct. Figure 4.11

shows how the piston and tip and tilt errors converged through each iteration.

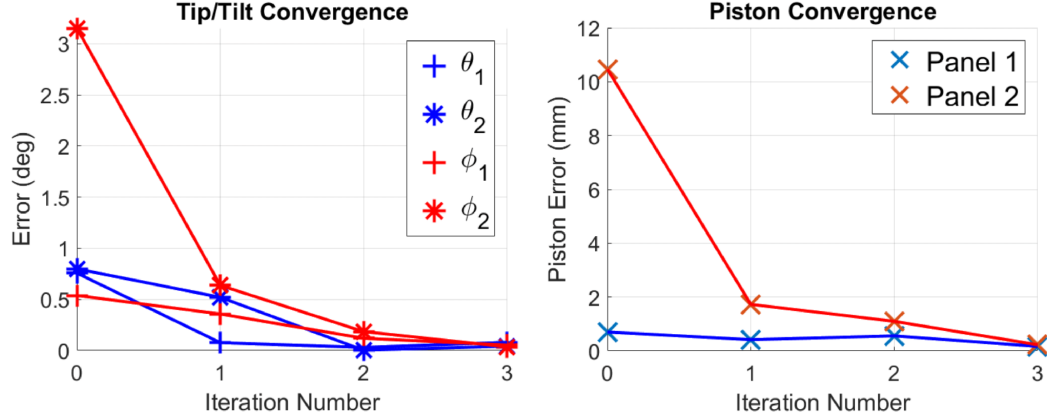


Figure 4.11: Four measurements were performed, with three adjustment iterations between each measurement. Left, is the tip and tilt of each panel improving across each iteration. Right shows the piston for each panel also improving. Panel 1 was fortunately close to the ideal piston position before an adjustment was performed.

Table 4.3: Final results after 3 adjustments.

Property	Panel 1	Panel 2
δZ	-0.17 mm	0.23 mm
θ	0.081 deg	-0.044 deg
ϕ	-0.054 deg	-0.037 deg

4.6 Discussions and Future Work

This method provides several advantages compared to other antenna metrology methods. The major improvement results from its non-contact nature. This has a two-fold benefit: speed and logistics. The setup time is less than 10 minutes, and the measurement takes only 10 minutes. This could be reduced even further by implementing a brighter projector and decreasing the required exposure time. Due to the rapid setup time, the system could be moved from telescope to telescope for the purpose of aligning arrays with large numbers of dishes. This avoids the

need to coordinate with satellites and the use of cryogenic detectors required by the holography method. This method also eliminates much of the labor required by photogrammetry and laser trackers, which require manual placement of stickers or retroreflectors. These methods are time consuming, labor intensive, and create safety risks for those that need to climb the dishes and place the fiducials. This method could also be installed on the telescope structure as a permanent metrology system for telescopes that have active surfaces or require regular maintenance[119]. This would also allow surface measurements to be performed at a variety of elevation angles to properly characterize gravity deformations.

Additionally, this method could be scalable to extremely large radio telescope apertures like the ngVLA 18-meter dish. Sensor size, lens focal length, and the number of cameras can be adjusted to achieve the required spatial resolution and field of view to cover the aperture of a large dish. There are some practical challenges to overcome to achieve this related to camera calibration and projector brightness. Some development is needed to calibrate a large number of cameras over a large area, with a long working distance. Methods utilizing auxiliary sensors to calibrate cameras with large baselines could be used [106, 107], but likely need some future development to adapt for more cameras. In addition, developing or sourcing a projector with enough brightness to cover this large area could be challenging, however commercial cinema projectors may be ideal. Regardless, the use of a light fiducial rather than a physical fiducial has many benefits in time, safety, and spatial resolution. Overall, the methods described in this chapter aim to ease the process for aligning current and future radio telescope dishes.

CHAPTER 5

Concluding Remarks

This dissertation has presented contributions to the fields of optical design, metrology, and alignment for scalable large optical systems. The aim of this research was to employ these methods to reduce the costs of large optical systems, thereby enabling faster production and enhancing accessibility to advanced optical technologies.

Chapter 2 covered optical design for the Large Fiber Array Spectroscopic Telescope (LFAST). LFAST is designed to circumvent the current status quo of large optical telescopes, whose costs scale unsustainably with aperture diameter. It would cost 10s of billions of dollars to build a single telescope of appropriate size to make annual detections of exoplanet atmosphere biosignatures. In 1977[25], Roger Angel originally proposed that you could make a large collecting area telescope by making separate telescopes and linking them together with fused silica optical fibers. At the time, the technology was not mature enough to make this happen. Looking forward 40 years, optical communication has become a key internet infrastructure, resulting in mass production of optical fibers. Telescopes are getting larger and larger, but smaller telescopes are getting cheaper and cheaper. This created the prime environment to begin executing LFAST. This dissertation covered a simple yet high-performing design for the unit telescope of LFAST. The design is all-spherical, has loose tolerances, uses low-cost materials, has diffraction limited performance, and has that diffraction limited performance even at low elevations in the sky that would be squandered by atmospheric dispersion without correction. The loose tolerances from using a spherical primary mirror allow for easier co-alignment of neighboring telescopes, which will be needed for the 20-unit prototype. The 20-unit prototype is slated to be constructed in 2024 using the optical design presented in this dissertation.

Chapter 3 covers metrology for a rapid panel forming technique. The field of

radio astronomy is growing rapidly, especially since the release of the black hole event horizon image from the Event Horizon Telescope (EHT). As a result, the demand is increasing for radio telescopes with larger apertures, longer baselines, higher quantities, and higher frequencies. Since these telescope dishes are made of smaller panels, the demand is also increasing for panels with higher accuracy, lower cost, higher quantities, and more exotic shapes. In 2020, the Steward Observatory Solar Lab (SOSL) received a grant to advance a new method for forming radio telescope panels that can meet these demands. The steps in this new manufacturing technique requires metrology at many steps along the way. To aptly assist the research into this new manufacturing method, the metrology needs to be rapid, accurate to 10s of microns, high spatial resolution, and operate over areas up to 2 x 2 meters. All existing metrology methods that could be purchased failed at least one of these requirements. This dissertation presented a metrology method based on photogrammetry and structured light for a binocular fringe projection profilometry (FPP) system. The method produces measurements in less than 10 minutes, has millimeter level spatial resolution, and less than 10 μm RMS depth accuracy. The team has been using the system for testing the flexible mold surface, measuring the panels made with the mold surface, and assisting iterative engineering development of the entire process. The system will continue to assist SOSL through the duration of the project.

Chapter 4 covers alignment for radio telescope dishes. While Chapter 3 discussed metrology for individual panels, the metrology and alignment of those panels once assembled on the full dish presents an entirely different challenge. Existing metrology methods based on physical fiducials like photogrammetry and laser trackers have low spatial resolution, are time consuming, and present potential safety hazards. Holography has been traditionally used because of its high sensitivity, but it requires custom cryogenic detectors, coordination with a geosynchronous satellite, and teams of experienced researchers. Part of the grant to advance methods of radio telescope manufacturing was to demonstrate it by building a radio telescope of our own, a 2.4 x 3.2 meter telescope named the Student Radio Telescope (SRT). The

team found that all existing methods to align the dish were expensive, inconvenient, or inaccessible. Chapter 4 outlines how the FPP metrology method described in Chapter 3 was adapted to assist with alignment of radio telescope dishes. The system was changed to be able to measure discontinuous surfaces outdoors, and was used to align two sample panels to create a dish that was limited in accuracy by the panel shape, not by the alignment. This method will be used to measure the entire SRT's 26 panels for completing the project next year. Both methods in Chapter 3 and Chapter 4 will be commercialized by the author's founded company Fringe Metrology LLC to continue research to make the methods faster, more accurate, and more robust to environmental effects. The goal is to deliver them to real world applications.

The solutions presented in this dissertation serve to advance the future of astronomy through scalability. Astronomy has historically been performed with custom manufactured, expensive instruments. The future of astronomy depends on the ability to produce astronomical instruments without an astronomical cost. This ability depends on every aspect of the design and manufacturing process, including but not limited to the optical design, metrology and alignment. Optical design is key for LFAST to be able to produce low-cost telescopes in volume. Metrology is required to advance new manufacturing techniques for accelerating radio telescope production. Alignment is required to commission large numbers of radio telescopes quickly. While this dissertation does not cover all problems related to large optical systems, it does contribute towards solving problems with scalability and reduction of cost through improved methods.

APPENDIX A

Large Fiber Array Spectroscopic Telescope: Optical Design for a Scalable Unit
Telescope

Joel Berkson, Roger Angel, Chad Bender, Andrew Monson, Peter Gray, Christian
Schwab, Warren Foster, Daewook Kim

Journal article submitted to

Springer Nanomanufacturing and Metrology

Special Issue: Astronomical Optics Manufacturing and Testing

*Author information removed from submitted reprint for double-blind peer review
from Springer.*

Large Fiber Array Spectroscopic Telescope: Optical Design for a Scalable Unit Telescope

***1,a,#, ***1,b, ***1,c, ***1, ***1, ***1,d

(***)

#corresponding author

Received: August XX, 201X / Revised: August XX, 201X/Accepted: August XX, 201X/Published online: August XX, 201X

Abstract:

The Large Fiber Array Spectroscopic Telescope (LFAST) concept is to collect light from a target object using 2,640 individual, 0.76 m 'unit telescopes'. The light from all the telescope foci is brought to a high-resolution spectrograph via optical fibers which subtend 1.47 arcsec diameter on the sky. The combined light collecting area of all the telescopes is 1,200 m². The need for coherence is eliminated since the telescope will be used for spectroscopy of seeing-limited images. The LFAST prototype goal is to demonstrate a telescope that can be rapidly and cost effectively replicated to achieve this 1,200 m² collecting area, making it comparable to extremely large telescopes (ELTs) currently under construction. The engineering, manufacturing, and design challenges of LFAST are far different from those of traditional ELTs. Since the 'unit telescope' is to be replicated thousands of times, decreasing the manufacturing cost per telescope is key. The design described here, with strong considerations for manufacturability, alignment, few moving parts, and high yield, works to achieve this goal. It is based on experience with a first prototype unit telescope built in 2022, and will be used to build the first 20-unit tracking module in 2024, with the collecting area of a 3.4 m diameter mirror. The design is made to be minimalistic and with commercial tolerances, therefore making it inexpensive to manufacture, assemble and align. The telescope is designed to operate as low as 70° from zenith by laterally translating a single lens to correct for atmospheric dispersion. We report a combined average of better than 80% encircled energy across 2,640 Monte Carlo trials with these commercial tolerances and capabilities, to model how the array will perform as a whole.

Keywords : telescopes, corrective optics, atmospheric dispersion compensation, mass production

Highlights:

1. LFAST is an 'array telescope' designed to combine light from multiple telescopes.
2. We have designed a telescope that is highly performing, at elevations as low as 70° from zenith.
3. Monte Carlo trials show that 80% average encircled energy can be achieved with standard tolerances for 2640 telescopes.

1. Introduction

Three extremely large telescopes (ELTs) are currently in production whose costs will exceed \$1 billion each: the Giant Magellan Telescope (GMT)[1], the European Extremely Large Telescope (E-ELT)[2], and the Thirty-Meter Telescope (TMT)[3]. While these telescopes will enable ground breaking science, they will still lack the capability to detect extremely faint signals, like the absorption spectrum in the atmosphere's of Earth-sized exoplanets around all but the brightest candidates.[4] Making a detection of potential biosignatures like oxygen with these ELTs will take many decades to accumulate enough photons. The direct way to improve this situation is to collect more photons per second. Unfortunately, current telescope cost scales approximately with the diameter of the aperture by $D^{2.77}$ [5, 6]. The cost makes it unreasonable to scale one of the currently in-development ELTs to an appropriate size, for example 10,000 m². To make regular characterizations of Earth-sized exoplanet atmospheres with a telescope of this size would cost in the

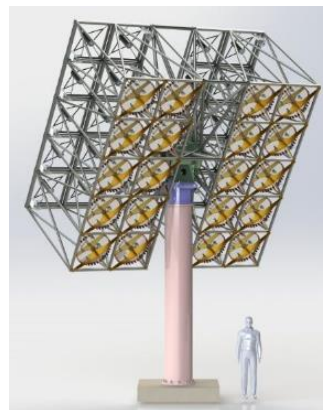


Fig. 1 Rendering of 20-unit telescopes mounted on a single alt-az bearing. An array of 132 of these is equivalent to ELT.

10s of billions of dollars. A new type of telescope is needed to target this science case.

The Large Fiber Array Spectroscopic Telescope (LFAST) is a concept for a telescope with a divided, incoherent aperture to combat the cost scaling laws of traditional telescopes[7]. The idea is to split the total collecting area of an ELT into many smaller 'unit' telescopes and produce them at a cost per unit area an order of magnitude less than the cost of current ELTs. To utilize the entire large collecting area, light from astronomical targets will be collected into optical fibers at the focus of each unit telescope and recombined to form a slit for a high-resolution spectrograph. To reduce the cost of tracking mounts, 20 of these 'unit' telescopes will be installed on one mount and fibers from many of these '20-unit' mounts will be combined at a central location for spectrograph input. Figure 1 shows a rendering of the 20-unit telescope. We designed and built a demonstration single unit telescope[8] during 2022 and 2023 for testing purposes, and are using lessons learned from that construction to iterate on the design to improve cost effectiveness and performance. The new design includes but is not limited to: increased optimization for manufacturing, better performance of the atmospheric dispersion compensator, a more in-depth tolerance analysis using a larger number of Monte Carlo trials, and a definition for the primary mirror specification using a structure function.

For the equivalent collecting area of E-ELT, LFAST will have 2640 primary mirrors with diameter 30": 132 20-unit mounts shown in Figure 1 combine to form an effective collecting area of 1,200 m². Co-phasing the telescopes is unnecessary and actually undesirable to accomplish the main goal of high-resolution spectroscopy, as the image formed at the spectrograph slit needs to be as stable as possible and coherent beams could cause interference fluctuations[9]. Because co-phasing is unnecessary, the cost of the entire telescope array can increase proportionally with collecting area (D²) once a repeatable manufacturing process is established. This concept is then scalable to add additional telescopes to further increase the collecting area with a linear increase in cost. This makes Earth-like exoplanet atmospheric detections possible more quickly.

The engineering problems for this kind of telescope are very different from traditional ELTs, where extensive time and money can be spent on a single telescope design, manufacturing, integration, and operation. For LFAST, the goal is to evolve a robust manufacturing and integration process early in the telescope development process and replicate it many times. The desire to eliminate recurring costs is key. This drives the need for a large portion of the telescope cost to be from non-recurring engineering (NRE), such that the relative cost per additional telescope diminishes as the number of telescopes increases, approaching a cost regime proportional to collecting area. To realize this goal, we developed a design for a unit telescope with a 30" clear aperture spherical primary mirror and a 4-element prime focus corrector. The design delivers diffraction-limited images to the fiber, and arcsecond images to a guide camera, while correcting atmospheric dispersion down to 70 degrees from zenith. In this paper, we will describe the design process, the performance of the telescope and atmospheric dispersion compensator, and the optical/mechanical tolerances of the telescope that are optimized for low-cost.

2. Optical Design

2.1 Specifications

Table 1 shows the optical performance specifications for each LFAST unit telescope. Table 2 shows the optical prescription for an LFAST 'unit' telescope. Figure 1 shows the full optical layout, and Figure 2 shows a more detailed view of the corrector optics.

Specification	Value
f/#	f/3.33
Wavelength	400-1700 nm
Aperture Size	30" (762 mm)
FOV	4 arcmin HFOV
Maximum viewing angle from zenith	70°
Performance: On-axis @ fiber as-built	Average for 2640 Monte Carlo trials >80% encircled energy
Performance: 4 arcmin @ guide camera	1 arcsec FWHM spot size

Table 1 Optical requirements for the first LFAST unit telescope

Primary Mirror		
	R	5275.0 mm
	Substrate	BORO FLOAT
	Clear Aperture	30 inches
	Spacing to L1	2351.83 mm
Prime Focus Corrector		
L1	R1	170.22 mm
	R2	279.50 mm
	Thickness	8.0 mm
	Substrate	H-K9LGT
	Diameter	101.6 mm
	Spacing to L2	1.0 mm
L2	R1	141.69 mm
	R2	167.86 mm
	Thickness	8.0 mm
	Substrate	H-F4
	Diameter	101.6 mm
	Spacing to L3	95.40 mm
L3	R1	Infinity
	R2	185.37 mm
	Thickness	7.0 mm
	Substrate	H-K9LGT
	Diameter	76.2 mm
	Spacing to L4	5.67 mm
L4	R1	Infinity
	R2	295.5 mm
	Thickness	3.9 mm
	Substrate	H-F4
	Diameter	70.0 mm
	Spacing to Fiber Puck	167.86 mm
Fiber Puck		
	Tilt Angle	22.5 degrees
	Fiber Diameter	18 μm
	Spacing to Relay Singlet	35 mm
Relay		
Singlet	R1	Infinity
	R2	27.72 mm
	Thickness	5.0 mm
	Substrate	H-K9LGT
	Aperture	19.0 mm
Doublet	R1	43.44 mm
	R2	19.54 mm
	R3	Infinity
	Thickness 1	6.0 mm
	Thickness 2	3.0 mm
	Substrate 1	H-K9LGT
	Substrate 2	H-F4
	Aperture	19.0 mm
	Distance to Fold Mirror	26.91 mm
Fold Mirror		
	Fold Angle	25 degrees
System Properties		
	f/#	3.33
	Focal Length	2534.3 mm

Table 1 Optical prescription for the LFAST unit telescope

There are a few interesting things to note about the specifications for an LFAST unit telescope. First, there are two places where image quality is important: at the fiber injection and at the guide camera. At the fiber, only the near on-axis fields are important. The only goal at that surface is to get as much light as possible from the target in the fiber core, which allows image quality requirements for the rest of the field to be far less strict. The image quality across the whole field only matters at the guide camera, and only ~380-950 nm light can be detected by typical CMOS sensors. There are three purposes for the guide camera: to know where the telescope is pointing in the night sky, to give feedback on the coupling of the starlight into the fiber, and to give information on the telescope aberrations. The fiber will show up as a tiny 'black hole' in the center of the FOV on the guide camera which can be used for fiber coupling feedback. Being able to couple dim stars into the fiber is important, so brighter stars in the

field need to be used to triangulate their locations, leading to a wider FOV requirement. Good imaging performance allows improved guiding on dimmer stars, but the performance at this surface does not need to be diffraction limited. We expect that LFAST will be located at a site that supports arcsecond-quality seeing conditions, so we designed the relay lenses to form arcsecond full-width half maximum (FWHM) images at the guide camera to balance image quality with atmospheric effects.

Desire to cover as much of the night sky as possible and provide a broad bandpass for spectrographs led to requirements for being able to view objects down to 70° from zenith and perform over two octaves of frequency. An $18\ \mu\text{m}$ fiber with telescope of focal length $2520.12\ \text{mm}$ (derived from $f/\#$ requirement) subtends 1.47 arcseconds on the sky. At 70° elevation from zenith, atmospheric dispersion is a few arcseconds, so correction needs to be made to maintain performance across the bandpass. L4 shown in Figure 3 is used as an atmospheric dispersion compensator, which is described in more detail in Section 2.4.

Lastly, we are producing these telescopes in mass quantities, with a goal of maximum energy coupled into each telescope's fiber. As a final design performance check, we ran Monte Carlo trials for all 2,640 telescopes in the array to ensure that an average of at least 80% encircled energy is maintained. The following subsections describe each piece of the LFAST design, and the reasoning behind each one in attempt to make a cost-effective, high-performing telescope.

2.2 Primary Mirror

A substantial driver of cost and schedule in nearly any large telescope is the primary mirror[10–12]. This is often due to logistical and physical limitations of manufacturing large, custom mirrors. It takes a long time for glass to cool, and a long time to remove material to polish perfect aspheric surfaces. This makes it impractical for

LFAST to make mirrors in a similar way, since the goal is to make thousands of them. The cost of the primary mirror needs to diminish at higher manufacturing volumes for the concept of LFAST to be viable. This leads to a rather unusual design decision for meter class telescopes, with a few notable exceptions[13]: a spherical primary mirror. While spherical primary mirrors suffer from significant spherical aberration and coma, they are much easier to make via using full-sized pitch polishing laps. This method naturally produces spherical shapes, and spherical primary mirrors are more tolerant to alignment errors since they have no axis. Higher surface complexity is not generally worth the fabrication cost: even an optimized aspheric mirror would leave significant coma in the near off-axis fields requiring downstream correction, and a conic would require aspherizing in the polishing process for extra money and time. Spherical is actually an optimal primary mirror choice for a small, narrow field of view telescope meant for mass manufacturing and single object spectroscopy.

We had initially considered a Mangin mirror (reflective coating on the back surface) to extend the lifetime for mirror coatings outdoors. We decided to not pursue Mangin mirrors because they introduced additional tolerances for the primary mirror including concentricity of the front and back surfaces, wedge tolerance between the two surfaces, and refractive index homogeneity. In addition, the thermal emissivity of glass versus silver and the need to polish two surfaces to high quality made the Mangin mirror a less desirable option for the primary mirror. For these reasons, we moved forward with a traditionally front-coated primary mirror and intend to have a protective metal coating to increase lifetime.

2.3 Prime Focus Corrector

The corrector optics can be split into two categories: before the fiber injection and after the fiber injection. As was discussed in §1,

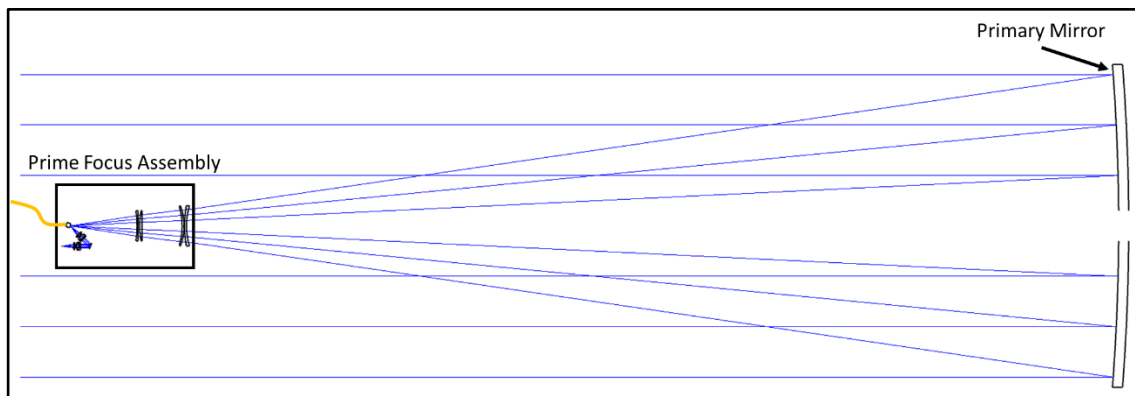


Fig. 2 2D optical layout of the unit telescope shown in Table 2.

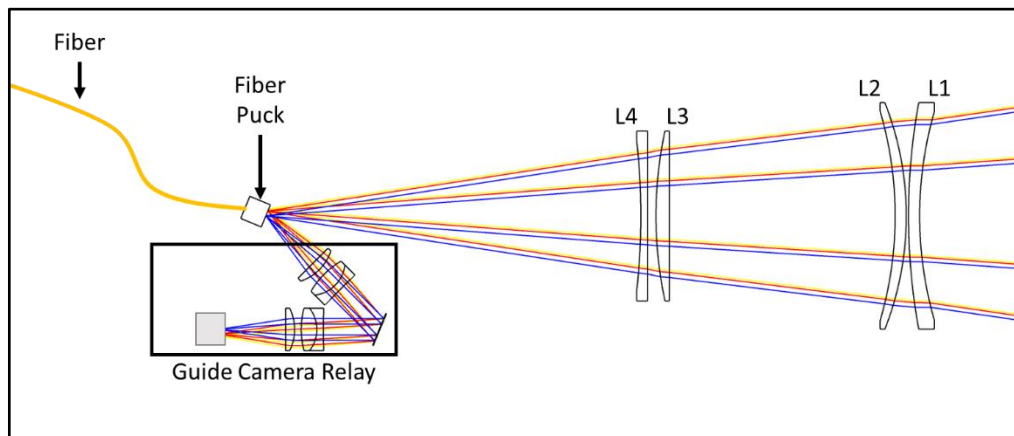


Fig. 3 Zoomed in view of the 2D layout of the prime focus corrector assembly, including corrector lenses, fiber puck, relay system, and guide camera.

the requirements at each of those image planes are quite different. At the fiber, only a central ~ 1 arcminute field of view is necessary to ensure maximum fiber coupling efficiency for the as-built telescope. At the guide camera, it is only important to obtain a field of view large enough to ensure that there are available stars for tracking.

The corrector optics were designed to maintain the focal ratio of the primary mirror, contributing minimal optical power. This allows for loosening axial alignment and manufacturing requirements for the corrector lenses. Maksutov originally demonstrated that third order spherical aberration can be perfectly corrected with a single meniscus lens close to focus, where the lens is self-achromatic[14]. This single lens cannot correct coma and leaves some residual transverse chromatic aberration. This lens is essentially L1 in the LFAST design. To correct the spherical aberration and coma from the primary mirror and keep the focal ratio constant, only two lenses are needed to give enough degrees of freedom, one of flint and one of crown to correct for chromatic aberrations. This leaves a small amount of astigmatism and Petzval curvature[15, 16]. At this point, the system is already diffraction limited on-axis, but performance degrades for off-axis fields. To give some margin for optical and mechanical tolerances and pointing errors, we require a broader range of diffraction limited imaging performance. Thus, more than two lenses are needed to extend the diffraction limited performance beyond the on-axis field. We found that two more lenses (L3 and L4) enable this correction. The corrector was designed with these concepts in mind, correcting for Seidel aberrations one by one and sequentially from L1 to L4. All lens radii and spacings were optimized to achieve diffraction limited

spot sizes within a 1 arcminute field, from $1.6 \mu\text{m}$ Airy radius at 400 nm to $6.9 \mu\text{m}$ at 1700 nm . The glass types of N-BK7 and F2 from Schott were originally chosen for their low cost, high manufacturability, and good transmission in the required bandpass. In the current design, equivalent H-K9LGT and H-F4 from CDGM will be used instead due to availability and cost, but in theory any crown-flint combination with Abbe number difference comparable to 27.7 could achieve good image quality.

2.4 Atmospheric dispersion correction

As mentioned previously, the optical system needs to meet all specifications across the bandpass, even at elevation angles close to the horizon. Across 400 to 1700 nm , nearly 4 arcseconds of atmospheric dispersion is present at 70 degrees from zenith, which means some dispersion correction is necessary for optimal coupling into the 1.47 arcsecond fiber. Common atmospheric dispersion compensator (ADC) strategies involve counter rotating prisms (Amici prisms, or CR-ADC)[17, 18], linear ADC's (LADC) using axial motion of thin wedge prisms[19], tilting low-power lenses[16], or compensating lateral ADC (CL-ADC)[20, 21] using counter-translating lenses. CR-ADCs and LADCs work extremely well and can be designed to correct secondary color down to 10s of milliarcseconds[18], but often involve complicated mechanics to achieve the desired prism motion. This level of correction is unnecessary for LFAST.

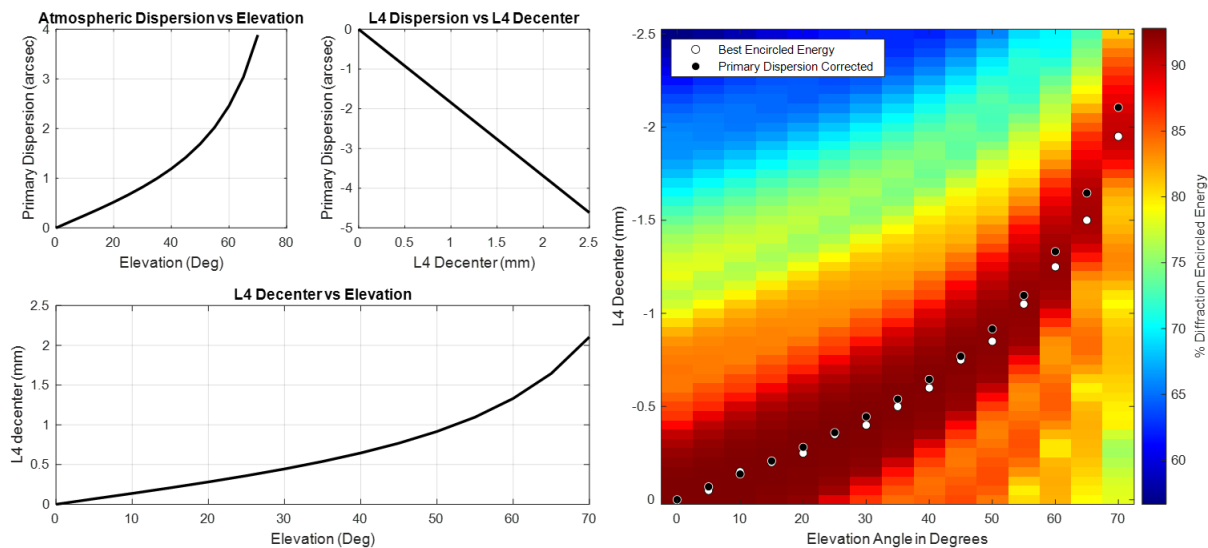


Fig. 4 Optimization of L4 decenter to correct for atmospheric dispersion. Upper left shows the primary atmospheric dispersion as a function of elevation and induced primary dispersion from L4 as a function of decenter. These curves can be mapped to the required L4 decenter to correct for primary atmospheric dispersion as a function of elevation angle (bottom left). The decenter required to correct for primary atmospheric dispersion correction, however, does not produce the best encircled energy, thus a numerical analysis was performed to find the optimal L4 decenter as a function of elevation (right).

For the thousands of telescopes in LFAST, fewer moving parts are desirable to eliminate points of failure. In addition, CR-ADCs and LADCs add additional components, causing energy losses at each interface and taking up valuable space and mass in the prime focus corrector of each telescope. The simplest solution for LFAST is the concept of CL-ADCs, as it does not add any additional components to the system. Typically, this method involves counter-translating two lenses to compensate for the tilt and astigmatism caused by translating one of the lenses. Since the only performance metric that matters is encircled energy into the fiber, perfect correction of atmospheric dispersion is unnecessary, thus some secondary spectrum can be tolerated. We designed the telescope to require translating only one lens for atmospheric dispersion correction. Using lateral translation of L4 by 2 mm also creates nearly an arcminute of image motion. Since the required time for this correction is slow, and the primary mirror is spherical, simply tilting the primary mirror to recenter the celestial target on the fiber can be done with minimal effect on the image quality.

This design utilizes L4 as the ADC component. L4 decentering can perfectly correct primary lateral color caused by the atmosphere (matching the chief ray positions of the shortest and longest wavelength in the bandpass). Figure 4 shows a plot of the primary lateral color caused by the atmosphere as a function of elevation angle [22, 23], the primary color induced by L4 as a function of decenter, and thus the L4 decenter required at each elevation angle to correct for primary lateral color. However, because the atmosphere does not have the same dispersion as the H-F4 flint glass in L4, this is not the best solution for optimum encircled energy coupled into the injection fiber. We carried out a numerical analysis to determine the actual required L4 decenter values to achieve the best encircled energy. At shallower elevation angles, these values start to diverge and expose the slight differences in dispersion of the flint glass and the atmosphere. A slight under-correction of primary lateral color due

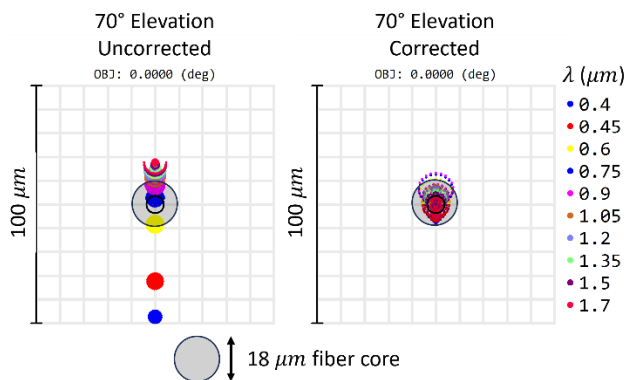


Fig. 5 Spot diagram at the lowest elevation uncorrected (left) and corrected with L4 lateral translation (right). Also shown is the 18 μm fiber core in gray.

to the atmosphere yields the best encircled energy. Figure 5 shows an example corrected spot diagram at the 70° from zenith. Encircled energy in this worst case is 90.3%, compared to the diffraction limit of 92.7%. Thus, even in this worst case, the telescope would still be seeing-limited.

2.5 Atmospheric jitter compensation

As mentioned in the previous section, translating L4 to compensate for atmospheric dispersion also significantly translates the image. In other telescopes, this would be an inconvenience, requiring extra components to compensate for the chief ray deflection and aberrations caused by misalignment of aspheric mirrors. For LFAST, we can use this property as an advantage. The atmosphere will cause seeing motion to the wavefront on the order of arcseconds. This will significantly degrade fiber coupling efficiency. For every 100 μm translation in L4, the image moves 34 μm , or about 2.8 arcseconds. This is a small percentage of the lens motion needed to

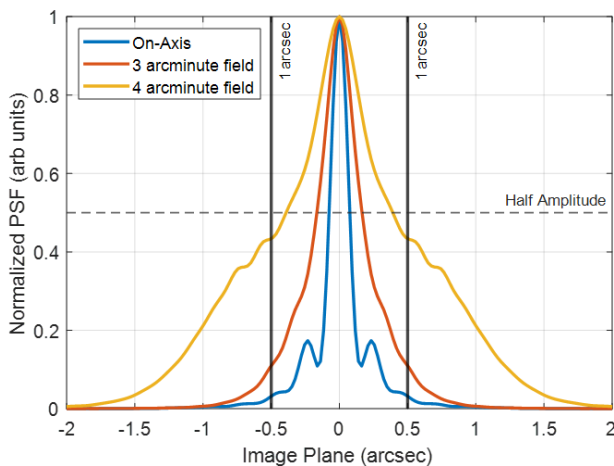


Fig. 6 Polychromatic PSFs for 3 field points at the guide camera image plane. All field points are better than 1 arcsecond FWHM.

correct for atmospheric dispersion at low elevations on the horizon (for example 1.9 mm at 70 degrees), thus this lens motion can be used to correct for image motion caused by atmospheric wavefront tip/tilt without significantly disrupting dispersion correction. Looking again at Figure 4, at each elevation if the L4 decenter is changed from optimal by 100 μm , only a few % encircled energy is lost, as opposed to more significant losses if the wavefront tilt is uncorrected and the star image is not centered on the fiber. Implementing a rapid corrective movement on L4 allows LFAST to obtain improved performance with the compensation of image motion due to seeing and mount shake.

2.6 Fiber feed and relay optics

Each telescope will need feedback to determine whether light is properly coupled into the fiber or not, as well as a wide field for guiding. The LFAST telescope primary mirror is small, and thus has limited light collecting ability for the short exposure times required for guiding. A wider field of view improves the chance of bright stars existing in the guide camera field of view for off-axis guiding. To achieve this large field, the fiber will be potted inside a small fold mirror at the image plane, which is relayed 1:1 onto a camera sensor with a relay lens and another fold mirror, as shown in Figure 3. This avoids losses from using a beam splitter and maintains a mechanically compact layout. The requirements on the relay require a larger field of view, but a narrower bandpass. The relay was optimized for wavelengths 500-800 nm, over a 4-arcminute half field of view. This gives a 97% chance of at least one 16th magnitude star in the field of view, which we can capture with a signal to noise ratio of ~30 using a 10 second exposure [24, 25]. The relay is made of two copies of a simple lens assembly, a plano-convex lens and a doublet. Again, these lenses were originally made with N-BK7 and F2 but were switched to the CDGM equivalents described in Section 2.3. The relay was also redesigned to balance the imaging performance across the broader field. Figure 6 shows the polychromatic point spread functions (PSFs) at the guide camera sensor plane.

3 Tolerancing

Our initial design [8] tolerancing was done with a small number of trials, but this telescope is designed to be built 2640 times, so a more encompassing Monte Carlo trial was executed to gain a perspective on how the telescope array as a whole may perform. Previously, a standard irregularity tolerance was used to specify the primary mirror, but this does not suffice for a meter-class mirror. For this new design, tolerancing was split into two pieces: the corrector and the primary mirror. For mirrors of this size, it becomes difficult to specify with a single root-mean-square (RMS) or peak to valley irregularity value

(e.g., $\lambda/4$ or $\lambda/8$). Wavefront slope is what truly impacts image quality, but slope cannot be described by a single depth RMS value, as it is dependent on spatial scale. A structure function is used to define the mirror requirements instead. The following sections tolerance the two key pieces of the telescope separately and attempts to balance the errors introduced by the mirror, the corrector, and the atmosphere.

3.1 Prime Focus Corrector

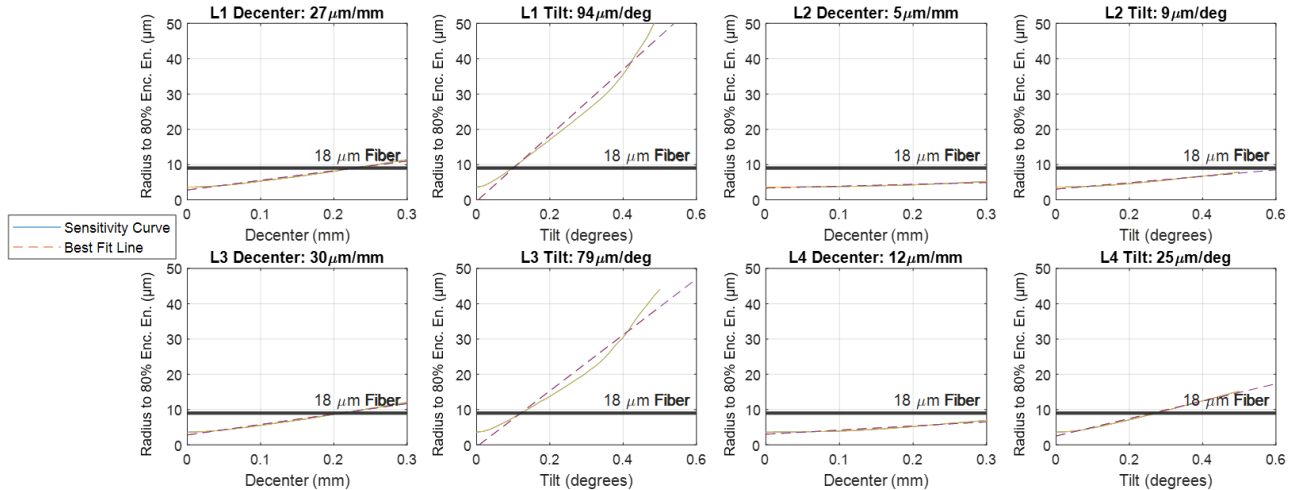
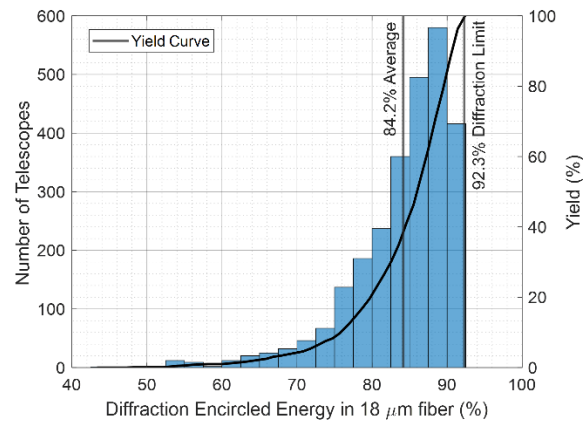


Fig. 7 Sensitivity curves and best fit lines shown for decenter and tilt of each corrector lens. Sensitivity values are shown as $\mu\text{m}/\text{mm}$ for decenter or $\mu\text{m}/\text{deg}$ for tilt. These values indicate the increase in radius to 80% encircled energy per unit perturbation

Tolerances			
Primary Mirror	R	\pm	75 mm
L1-L4	R	\pm	10 fringe
L1-L4	Center Thickness	\pm	150 μm
L1-L4	Irregularity	\pm	1 fringe
L1-L4	Wedge (ETD)	\pm	50 μm
L2/L4	Element Decenter	\pm	100 μm
L1/L3	Element Decenter	\pm	50 μm
L1-L4	Element Tilt	\pm	3 arcmin
L1-L4	Refractive Index	\pm	0.001 a.u.
L1-L4	Abbe Number	\pm	0.8 %
PFC Assembly	Tilt	\pm	3 arcmin
	Dcenter	\pm	3 mm

(a)



(b)

Fig. 8 Final tolerances for the prime focus corrector (left). L1 and L3 have slightly more sensitivity than L2 and L4, thus the decenter tolerance is tighter for L1 and L3. Irregularity, wedge, radius error, center thickness, and material properties are all within standard tolerances for a variety of manufacturers. Mechanical tolerances are within achievable tolerances for a lens barrel. The yield curve and histogram (right) are shown for 2640 Monte Carlo trials using these tolerances. The average performance is 84.2% encircled energy, and the number of telescopes is shown in 2.5% bin widths.

One of the key characteristics of LFAST is mass manufacturability at low cost. This largely depends on the optical and mechanical tolerances of the system to maintain high quality performance. LFAST needs to produce components in large quantities, therefore any components that require high-precision machining or alignment are undesirable. All components and optics should be easily scalable both in the manufacturing as well as the assembly. Care was taken to loosen tolerances where possible to expedite production of LFAST telescopes at a low cost.

Because the primary mirror is spherical, and the prime focus corrector was designed to maintain the focal ratio of the primary mirror, axial errors have minimal impact on wavefront error (WFE). As a result, image degradation due to errors such as lens spacing, lens thickness, surface radii, and even refractive index, are mitigated with the assumption that primary mirror piston is a compensator for

defocus.

Figure 7 shows mechanical tolerances and sensitivity curves for non-axial errors found for decenter/tilt of L1-L4. L1 and L3 are the most mechanically sensitive components, while L2 and L4 are looser. This information allowed us to better tighten tolerances where they are most effective as compared to the previous design[8]. We began with 0.1 mm decenter tolerances on L2 and L4, 0.05 mm on L1 and L3, and 3 arcminutes (0.05 degrees) of tilt on all lenses, or

approximately 0.1 mm edge thickness difference (ETD) at 100 mm diameter. Figure 8a shows how this is combined together with all other tolerances for Monte Carlo trials. All axial tolerances are very loose ($\pm 150 \mu\text{m}$), and were set to the standard loosest requirement per many optical manufacturers tolerancing charts[26–29].

This tolerancing does not include aberrations on the primary mirror, but rather isolates properties of the corrector that are loose or sensitive. As expected, any axial errors due to surface power or lens spacing/thickness are easily compensated for with $\pm 25 \text{ mm}$ of primary mirror piston. The most sensitive parameters are non-axial errors: lens decenter, lens wedge, and element tilt, although these are still well within commercial machining tolerances. All tolerances chosen are within "commercial" or "standard" tolerances given by a variety of optics manufacturers, and should be achievable with commercial machining and alignment tolerances for a lens barrel[30].

Figure 8b shows the yield for 2640 telescopes using uniform distributions of the tolerances shown in Figure 8a, demonstrating that 80% of the telescopes meet the 80% encircled energy requirement, and the average performance exceeds 80%.

3.2 Primary Mirror

All other surfaces in the telescope design have a single surface irregularity specification in number of fringes, which is a depth value. Common irregularity in pitch polished lenses takes the form of low order Zernike polynomials. However, for large surfaces, this specification is often not good enough, as mid-spatial frequencies become more present and impactful to the surface slope errors. For high performance systems, especially ELTs, a slope specification is needed to define surface deviations at a variety of spatial scales. LFAST aims to use 1" thick, 30" diameter BOROFLOAT® mirrors. This is a standard thickness for BOROFLOAT® glass, which reduces the cost of procurement. Due to the small aspect ratio of the mirror (30 to 1), it is likely that mid-spatial frequencies may show up in the

polishing process due to local bending of the mirror. As the spatial scale of surface errors shrinks but the amplitude does not, the RMS slope increases[31]. Because optical performance (wavefront error) is truly dependent on surface slope error, surface error amplitude requirements are directly dependent on spatial scale. A peak to valley specification suffers from the same problem[32]. At scale smaller than $\lambda/20$, light will react to the surface as if it is perfectly smooth.

The GMT mirrors have been specified using a structure function[33–36], which is a measure of the wavefront error as a function of spatial scale. It is defined as the mean square wavefront difference between random points in the aperture as a function of their separation. It is used since wavefront error due to atmosphere turbulence is also commonly described by a structure function[37, 38]. Turbulence often fundamentally limits the image quality of a telescope that does not use adaptive optics, like LFAST. It is expected that the location of LFAST may have seeing as good as 1 arcseconds FWHM, which will create a baseline best case encircled energy. Figure 9 shows this effect by convolving the polychromatic point

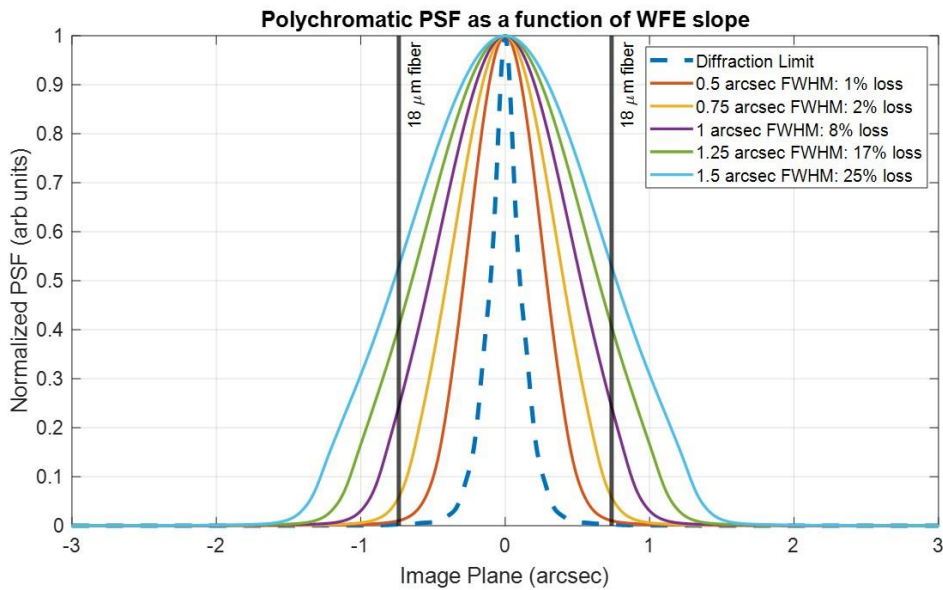


Fig. 9 Point Spread Function as a function of seeing. Loss of encircled energy increases rapidly as the FWHM approaches the fiber diameter.

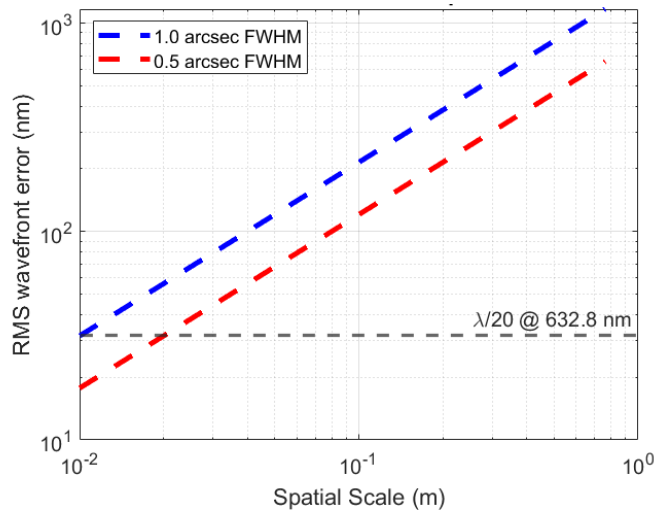


Fig. 10 Structure function requirement for LFAST. 1 arcsec is the expected atmospheric seeing conditions, and 0.5 arcsec is the mirror requirement goal.

spread function (PSF) of the telescope with a Gaussian of various arcsecond FWHM (or $2\sqrt{2\ln(2)\sigma}$).

At 1 arcsecond FWHM, we can expect approximately an 8% loss in encircled energy. This can be similarly applied to requirements for the primary mirror to define a requirement for the structure function. We showed in the previous section that the tolerancing of the PFC accounts for on average 8% loss compared to the diffraction limit. Using a tighter requirement on the primary mirror would thus make the telescope seeing limited. A 0.5 arcsecond FWHM requirement on the primary mirror would roughly balance the error contributions from the primary mirror, the corrector optics, and atmospheric seeing. Figure 10 shows the resulting structure function requirement for 1 arcsecond FWHM (the same as expected from the atmosphere), and a goal of 0.5 arcsec FWHM, measured at the interferometer test wavelength, 632.8 nm. The LFAST primary mirrors will have 24 Peltier devices around the edge of the mirror to control low order Zernike deformations[7]. As with the GMT mirrors, eventually, the diffraction limit is reached and a better surface will not make a better image, thus the requirements can be loosened at spatial scales that correspond to required wavefront error smaller than $\lambda/20$.

3.3 Testing

It is important to establish lab testing regimens to ensure that both the primary mirror and the PFC will meet performance requirements before testing them on-sky. For the spherical primary mirror, the measurement is trivial: a phase-shifting interferometer with the mirror center of curvature aligned with the interferometer focus for a null test configuration. The collected data is then used to calculate the structure function and compare to requirements in Figure 10. Testing the PFC is more difficult.

The PFC compensates for the spherical aberrations present in the spherical primary mirror when used at infinite conjugates. In a blackbox, it appears as an optic with a large amount of spherical aberration, and a small amount of power. If the PFC on its own was tested in double pass with a flat reference mirror, there is enough power and spherical aberration present that the fringes would alias, rendering the wavefront unmeasurable. To test the entire PFC assembly separately from the primary mirror, we have developed a null corrector made of two 3" H-K9LGT lenses to correct the on-axis aberrations introduced by the PFC. The PFC will be tested with a 2" diameter collimated beam from a Fizeau interferometer. Figure 11 shows the layout of the null lens and PFC test in double pass.

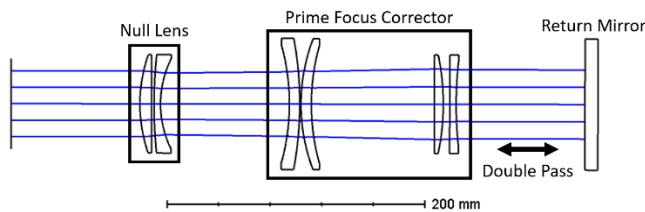


Fig. 11 Null Lens, Prime Focus Corrector, and return mirror set up in a double-pass configuration. The returning beam has only 0.0033 waves of wavefront error.

This double-pass Fizeau interferometer setup produces a $\lambda/300$ null. From the yield data in Figure 8b, about 80% of systems pass the 80% encircled energy requirement. The Monte Carlo trials indicated that the wavefront error associated with this cutoff is 0.5 waves RMS. This wavefront error will be doubled due to double-pass but will only be tested with half of the full aperture (2" test beam versus 4" L1) so we have set 0.5 waves RMS as the pass or fail requirement for the as-built PFC assembly under the double pass measurement.

4 Next Steps and Conclusion

We have presented a design for a 30" aperture telescope which is optimized to be economically produced in high volumes, as required

by the LFAST concept. The design is significantly improved in the aspect of higher volume manufacturing compared to the initial design that was built in 2022. The design is made with only spherical surfaces, even for the primary mirror. The design also includes the ability to correct atmospheric dispersion down to 70° by translating one of the corrector elements (L4) in sync with primary mirror tilt. Small motions of the same element will also be used to stabilize atmospheric wavefront tip/tilt, made possible by the all-spherical design. We have verified that tolerances are 'standard' or 'commercial' for all elements in the corrector, and that alignment requirements can be easily achieved with standard machining and lens centering procedures. Through Monte Carlo trials, over 80% of the 2640 telescopes meets the 80% encircled energy requirement.

We are currently testing electronics, guiding, and tracking for a single unit telescope, constructed in 2022 and 2023, using the same structure and mechanics to be used for the 20-unit telescope. We are concurrently in the process of manufacturing 30" mirrors, procuring lenses and lens barrels, and beginning construction on the steel frame structure for the construction of the 20-unit telescope in 2024.

ACKNOWLEDGEMENT

REFERENCES

1. Fanson J, Bernstein R, Ashby D, Bigelow B, Brossus G, Burgert W, Demers R, Fischer B, Figueroa F, Groark F, others (2022) Overview and status of the Giant Magellan Telescope project. In: Ground-based and Airborne Telescopes IX. SPIE, pp 454–473
2. Tamai R, Koehler B, Cirsuolo M, Biancat-Marchet F, Tuti M, Herrera J-CG, Ramsay S (2022) Status of the ESO's ELT construction. In: Ground-based and Airborne Telescopes IX. SPIE, pp 437–453
3. Liu F (2022) Thirty Meter Telescope (TMT) project status. In: Ground-based and Airborne Telescopes IX. SPIE, p 121821B
4. Hardegree-Ullman KK, Apai D, Bergsten GJ, Pascucci I, López-Morales M (2023) Bioverse: A Comprehensive Assessment of the Capabilities of Extremely Large Telescopes to Probe Earth-like O₂ Levels in Nearby Transiting Habitable-zone Exoplanets. *The Astronomical Journal* 165:267
5. van Belle GT, Meinel AB, Meinel MP (2004) The scaling relationship between telescope cost and aperture size for very large telescopes. In: Ground-based telescopes. Spie, pp 563–570
6. Meinel AB (1979) Cost Scaling Laws Applicable To Very Large Optical Telescopes. In: Crawford DL (ed) *Instrumentation in Astronomy III*. SPIE, pp 2–7
7. Angel R, Bender C, Berkson J, Didato N, Ford J, Gray P, Jannuzi B, Ketelsen D, Kim D, Lopez GC, others (2022) LFAST, the Large Fiber Array Spectroscopic Telescope. In: Ground-based and Airborne Telescopes IX. SPIE, pp 631–643
8. Berkson J, Angel R, Bender C, Young A, Gray P (2022) The Large Fiber Array Spectroscopic Telescope: optical design of the unit telescope. In: Ground-based and Airborne Telescopes IX. SPIE, pp 1013–1021

9. Bender CF, Angel JR, Berkson J, Gray P, Halverson S, Kang H, Kim D, Monson A, Oh CJ, Rademacher M, others (2022) The Large Fiber Array Spectroscopic Telescope: fiber feed and spectrometer conceptual design. In: *Ground-based and Airborne Instrumentation for Astronomy IX*. SPIE, pp 1490–1497
10. Johns M (2006) The giant magellan telescope (GMT). In: *Ground-based and Airborne Telescopes*. SPIE, pp 762–776
11. Nelson J, Sanders GH (2008) The status of the Thirty Meter Telescope project. In: *Ground-based and Airborne Telescopes II*. SPIE, pp 504–521
12. Gilmozzi R, Spyromilio J (2008) The 42m european elt: status. In: *Ground-based and Airborne Telescopes II*. SPIE, pp 494–503
13. Jungquist RK (1999) Optical design of the Hobby-Eberly Telescope four-mirror spherical aberration corrector. In: *Current Developments in Optical Design and Optical Engineering VIII*. SPIE, pp 2–16
14. Maksutov D (1944) New catadioptric meniscus systems. *JOSA* 34:270–284
15. Jones DJ, James WE (1992) Prime focus correctors for the spherical mirror. *Applied optics* 31:4384–4388
16. Jones DJ (1994) Wide-field prime focus corrector for the Anglo-Australian telescope. *Applied optics* 33:7362–7366
17. Goncharov AV, Devaney N, Dainty C (2007) Atmospheric dispersion compensation for extremely large telescopes. *Opt Express* 15:1534–1542. <https://doi.org/10.1364/OE.15.001534>
18. Rakich A (2021) A New Type of Atmospheric Dispersion Corrector Suitable for Wide-Field High-Resolution Imaging and Spectroscopy on Large Telescopes. *Applied Sciences* 11:6261
19. Avila G, Rupprecht G, Beckers JM (1997) Atmospheric dispersion correction for the FORS Focal Reducers at the ESO VLT. In: *Optical Telescopes of Today and Tomorrow*. SPIE, pp 1135–1143
20. Saunders W, Gillingham PR (2016) Optical designs for the Maunakea Spectroscopic Explorer telescope. In: *Ground-based and Airborne Telescopes VI*. SPIE, pp 1157–1168
21. Saunders W, Gillingham P, Smith G, Kent S, Doel P (2014) Prime focus wide-field corrector designs with lossless atmospheric dispersion correction. In: *Advances in Optical and Mechanical Technologies for Telescopes and Instrumentation*. SPIE, pp 519–528
22. Hohenkerk C, Sinclair A (1985) Nao technical note 63. HM Nautical Almanac Office
23. Seidelmann PK (1992) Explanatory supplement to the astronomical almanac. University Science Books
24. Bahcall NA, Soneira RM (1983) The spatial correlation function of rich clusters of galaxies. *Astrophysical Journal, Part 1 (ISSN 0004-637X)*, vol 270, July 1, 1983, p 20-38 270:20–38
25. Trumpler RJ, Weaver HF (1953) *Statistical astronomy*. Univ of California Press
26. Schwertz K, Burge JH (2012) *Field guide to optomechanical design and analysis*. SPIE Press
27. Edmund Optics (2023) *Precision Tolerances for Spherical Lenses*
28. LaCroix Precision Optics (2023) *Optical Manufacturing Tolerance Chart*
29. Optimax Systems, Inc (2023) *Manufacturing Tolerance Chart*
30. Lamontagne F (2017) *Optomechanical Tolerancing and Error Budgets*. *Handbook of Optomechanical Engineering* 207–268
31. Harvey JE (2021) The surface PSD and image degradation due to mid-spatial-frequency errors. In: *Tribute to James C. Wyant: The Extraordinaire in Optical Metrology and Optics Education*. SPIE, pp 160–173
32. Evans CJ (2009) PVr—a robust amplitude parameter for optical surface specification. *Optical Engineering* 48:043605–043605
33. Martin B, Hill JM, Angel R (1991) *The New Ground-Based Optical Telescopes*. *Physics Today* 44:22–30
34. Martin H, Burge J, Cuerden B, Davison W, Kingsley J, Kittrell W, Lutz R, Miller S, Zhao C, Zobrist T (2008) Progress in manufacturing the first 8.4 m off-axis segment for the Giant Magellan Telescope. In: *Advanced Optical and Mechanical Technologies in Telescopes and Instrumentation*. SPIE, pp 103–114
35. Martin H, Allen R, Burge J, Kim D, Kingsley J, Tuell M, West S, Zhao C, Zobrist T (2010) Fabrication and testing of the first 8.4-m off-axis segment for the Giant Magellan Telescope. In: *Modern Technologies in Space-and Ground-based Telescopes and Instrumentation*. SPIE, pp 84–96
36. Martin H, Allen R, Burge J, Kim D, Kingsley J, Law K, Lutz R, Strittmatter P, Su P, Tuell M, others (2012) Production of 8.4 m segments for the Giant Magellan Telescope. In: *Modern Technologies in Space-and Ground-based Telescopes and Instrumentation II*. SPIE, pp 801–815
37. Rao C, Jiang W, Ling N (2000) Spatial and temporal characterization of phase fluctuations in non-Kolmogorov atmospheric turbulence. *Journal of Modern Optics* 47:1111–1126
38. Consortini A, Ronchi L (1972) Choice of the model of atmospheric turbulence. *Applied Optics* 11:1205–1211

APPENDIX B

Binocular fringe projection profilometry for the metrology of meter-scale optical surfaces

Joel Berkson, Justin Hyatt, Hyukmo Kang, Sotero Ordones, Henry Quach,
Daewook Kim

Journal article published at

Optics Continuum, Vol. 2, No. 4, 15 Apr 2023



Binocular fringe projection profilometry for the metrology of meter-scale optical surfaces

JOEL BERKSON,^{1,2} JUSTIN HYATT,^{2,*} HYUKMO KANG,¹  SOTERO ORDONES,¹  HENRY QUACH,¹ AND DAEWOOK KIM^{1,2} 

¹James C. Wyant College of Optical Sciences, University of Arizona, 1630 E. University Blvd., Tucson, AZ 85721, USA

²Department of Astronomy and Steward Observatory, University of Arizona, 933 N Cherry Ave., Tucson, AZ 85721, USA

*justinh@arizona.edu

Abstract: Demand for better quality, larger quantity, and size of astronomical telescopes from visible to radio frequencies is increasing. More rapid, efficient, and adaptable manufacturing processes are needed to support the needs of growing science and engineering communities in these fields. To aid the development and execution of these new processes, a flexible, accurate, and low-cost metrology system is needed. This paper outlines a variety of fringe projection profilometry (FPP) that has demonstrated high accuracy over large areas, making it a critical tool for manufacturing steel molds for forming primary reflectors and shape verification of the reflectors themselves used for radio astronomy.

© 2023 Optica Publishing Group under the terms of the [Optica Open Access Publishing Agreement](#)

1. Introduction

In applications such as radio astronomy and optical component manufacturing, reflecting and refracting surfaces need to have very accurate shapes, yet often have surface roughness that makes them non-specular to visible wavelengths, either as the final product or in an intermediate stage of manufacturing. This presents a significant measurement challenge, since scattering reduces coherence and specularly. For example, surfaces used in high frequency radio astronomy have a common accuracy requirement of $\lambda/25$ [1] (often tens of microns for millimeter-scale wavelengths) but still need to scatter visible and near infrared wavelengths to avoid unintentional heating from focused sunlight [2]. Measurement of these surfaces is crucial to the performance of the final antenna [3–5], but metrology methods that rely on specular surfaces are futile in this application.

Current measurement options for large antenna segments either require physical probing of the surface or measurement of the locations of physical fiducials. Coordinate Measuring Machines (CMM) have traditionally been used to measure surface shapes by touching the surface with a probe at multiple points [6] and extracting 3D points using encoders. This method is performed on a point-by-point basis, so oftentimes taking high spatial resolution measurements aren't possible in a reasonable amount of time, as each sampled point takes a few seconds to acquire. Laser trackers have also been heavily used in the manufacturing of individual panels and shape verification of the final constructed antenna [7–10]. Laser trackers require physical placement of retro-reflector fiducials, meaning the fiducials need to be continuously relocated in order to sample a 3D point. Therefore, rapid high spatial resolution measurements are not possible with this method either.

Photogrammetry has also been used for some of these applications [6,11,12]. Photogrammetry involves capturing many images of precision fiducials that are placed on the surface, and triangulating the fiducials to produce 3D points. This method has shown high accuracy, but also requires manual placement of fiducials [13], significantly slowing the measurement process. In

this type of system, pixel utilization is low: only pixels that see the fiducial pattern are used to triangulate object locations.

Structured light scanning systems are similar to photogrammetry, but output much higher spatially sampled scans by utilizing a light source to produce fiducials and observing the reflected and/or scattered image with a camera in order to extract more information about the surface via triangulation [14–16]. This makes it a great candidate concept for rapid metrology of large, diffuse surfaces like radio telescope panels. Recent decades have produced vast amount of research into 3D scanning techniques using structured light, particularly Fringe Projection Profilometry (FPP) [17]. FPP is a sub-category of structured light measurement systems that specifically focuses on projecting a periodic pattern onto an object in order to rapidly extract feature information by observing the deformed pattern. There are many variations of FPP. Some research in this field focuses on optimizing system calibration methods [18,19]. Others focus more on the hardware, using different types of projectors or numbers of cameras [20]. There is also significant research into reduction of the non-linear effect of the phase shifting algorithms [21–24]. Much of the research in this field is focused on improving the measurement speed by using more efficient phase shifting algorithms that require fewer pattern acquisitions [25–27], and converting phase directly to depth based on calibration of a camera and a projector [28]. However, in general there is little focus on scaling up the concepts to measure large surfaces with extremely high accuracy.

This paper outlines a novel variation of FPP that vastly improves accuracy and precision within a reasonable measurement time, while still producing high spatial sampling, and nearly eliminating non-linearity phase-shifting errors. The concept is easily scalable and simple to calibrate, making it a useful technique for measuring radio telescope panels and other large, continuous surfaces that have high accuracy requirements.

2. Background

2.1. Fringe projection profilometry

FPP systems often involve projecting a series of N phase-shifted sinusoidal patterns onto an object and taking images of the distorted pattern with a camera [26]. The captured pattern typically takes the form of Eq. (1) for vertically oriented fringes:

$$I_n(x, y) = a(x, y) + b(x, y) \cos \left[u_0 x + \frac{2\pi n}{N} + \phi_{obj}(x, y) \right] \quad (1)$$

where u_0 is the fringe frequency, n is the current phase step, N is the total number of phase steps, and $\phi_{obj}(x, y)$ is the phase of the object observed by a camera's 2D detector plane, which contains information about the object shape. $a(x, y)$ and $b(x, y)$ are the background intensity and the fringe modulation, respectively. Projecting this series of N patterns onto an object and capturing images with a camera encodes that object with contours of equal phase (ϕ_{obj}). The wrapped phase $\phi_{obj,wrapped}$ in Eq. (1) can be recovered with the N -step Phase Shifting Algorithm [25]:

$$\phi_{obj,wrapped}(x, y) = \arctan \left(\frac{\sum_{n=0}^{N-1} I_n(x, y) \sin(\frac{2\pi n}{N})}{\sum_{n=0}^{N-1} I_n(x, y) \cos(\frac{2\pi n}{N})} \right) \quad (2)$$

where $I_n(x, y)$ is the 2D irradiance pattern captured on the camera detector for each phase step n . This equation recovers the wrapped phase in modulo 2π steps, which can then be unwrapped with a spatial phase unwrapping method [29].

Most FPP systems then use a variety of phase-to-height mapping method to produce 3D measurements, based on the calibrated geometry of the camera and projector, or a calibration surface [30]. Oftentimes the projector and camera is treated as a stereo-pair, where the projector acts as an inverse camera, and the phase contours are used as epipolar geometry constraints

to determine matching features [26]. Either way, both of these methods require some form of calibration of the projector, which can be challenging to do accurately and quickly. This often requires additional calibration for gamma distortion, the nonlinear brightness response of displays [31,32]. In addition, this method relies on the temporal stability of projector illumination.

Some have added an additional camera to the system and leveraged multiple benefits [20]. With two cameras, the projector can simply act as a fiducial generator to assist stereo camera triangulation. Strategies to calibrate the intrinsic and extrinsic parameters of two cameras is very well-established [33]. In this case, the projector can be used to encode contours of equal phase using phase shifting in one direction, and feature matching based on the same epipolar geometry method as the projector-camera systems.

2.2. Stereo vision

The metrology method described in this paper is based on the simple concept of Stereo Vision (SV) [34]. SV computes 3D coordinates of objects based on the binocular disparity between the images of an object from two different perspectives. If the intrinsic properties of the cameras are known (i.e. focal length, distortion, principle point) and the extrinsic properties of the camera pair are known (i.e. relative rotation and translation difference between each camera), a 3D object could theoretically be perfectly reconstructed. However, diffraction, camera noise, and calibration errors of intrinsic and extrinsic parameters result in an uncertainty in measured coordinates. These errors culminate into an expected depth resolution limit of a SV system, which depends on the geometry of the camera perspectives relative to the object to be measured, and the method used to match object features. The equation for the depth resolution of a SV system is well-established in the field of computer vision [35]:

$$\delta z = \frac{z^2}{bf} \Delta p \quad (3)$$

where b is the camera baseline distance, z is the object distance from the baseline, f is the focal length of the cameras, and Δp is the disparity error in number of pixels multiplied by the physical pixel size, coming from the feature matching uncertainties in the system. These parameters can be easily adjusted to give predicted resolution in the tens of microns for surfaces sizes on the order of a square meter using current image sensor technology (pixel size and total array size limitations), assuming disparity error is on the order of a pixel. This resolution starts to degrade for systems that attempt to cover a larger area. If a larger area needs to be measured, one could decrease the focal length, but this hurts depth resolution inversely. One could simply move the cameras further away, but the distance from the object hurts depth resolution quadratically. One could also extend the camera baseline distance, but this can cause depth of focus limitations, making calibration of extrinsic parameters difficult and creating poor spatial resolution in one dimension. Therefore the only way to significantly improve the depth resolution while keeping hardware configuration constant is to decrease the pixel disparity error.

3. Precision stereo matching

If the stereo matching precision can be improved to subpixel matching accuracy, then the theoretical depth resolution experiences the same linear improvement, assuming perfect calibration. As described in Section 2.2, using a set of phase shifted sinusoidal fringe patterns encodes the object with contours of equal phase. Adding another set of phase shifted patterns oriented in the horizontal direction encodes the object with a unique phase pair combination at every point on the 3D object, imaged onto a camera's 2D detector plane: $\phi_h(x, y)$ and $\phi_v(x, y)$, for horizontal and vertical phase, respectively, with x and y denoting the vertical and horizontal locations on the detector plane. Figure 1 shows an example set of projected fringes, the wrapped phase for

each direction, and then unwrapped phase. We use a spatial phase unwrapping technique based on a reliability sorting method [29] to recover the continuous phase in the horizontal and vertical phase directions, for both cameras.

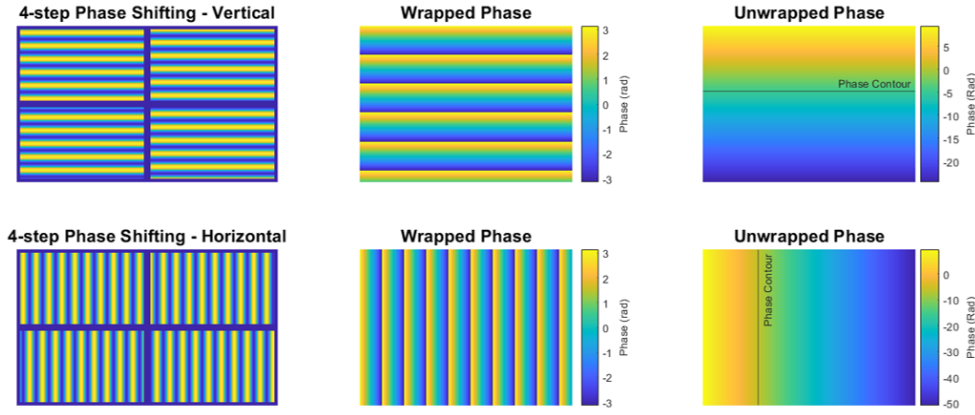


Fig. 1. Phase-shifted sinusoidal patterns encodes contours of equal phase. Only four steps are shown for simplicity. Using Eq. (2) produces the wrapped phase maps. The reliability sorting method by noncontinuous path method [29] is used to unwrap the phase. The result is a continuous phase distribution. Using this phase shifted pattern in two orthogonal directions then produces two phase distributions, which encodes every point with a unique phase pair combination.

Pixels on camera 1 can be matched to pixels based on the phase pair that has the minimum difference [36], and these matched pairs of pixels are triangulated to reconstruct a set of 3D points representing the object being measured.

However, this method does not fully utilize the information encoded on the object. The projector encodes the object with a continuous phase distribution, and those continuous distributions are measured with a discretely sampled detector array from each camera's perspective. It is highly unlikely that there is any one pixel on camera 1 that exactly samples the same area on the object as any pixel on camera 2. That means there is no pixel on camera 1 that has a phase pair that exactly matches the phase pair of a pixel on camera 2. Existing research has shown that subpixel phase matching can improve calibration via bundle adjustment using thousands of matched points and a variety of subpixel matching methods [37–40]. We aim to use subpixel phase matching to create a 3D point from every pixel that projects onto the object, and interpolate it until the subpixel matching location is as precise as possible. In order to accomplish this, we can assume that there likely exists a subpixel location on camera 2 that nearly exactly matches the phase pair of a pixel on camera 1. Much higher feature matching precision can be obtained by matching the phase pair of a *pixel* on camera 1 to a corresponding phase pair subpixel *location* on camera 2 via interpolation. One could simply interpolate the entire phase map by a large factor, but the image size, and therefore the search algorithm time for finding matching phase pairs, scales by n^2 . This would make processing times far too long on an average computer, on the order of hours. One could also fit each phase distribution to a surface map and solve the matching phase pair locations analytically, but would require an extremely high number of terms in order to preserve high frequency surface information. Instead, we search the image first for a rough match, and use a windowed interpolation strategy to iteratively search smaller interpolated windows, greatly reducing computation time while still producing subpixel matching precision, without losing spatial resolution. The steps of this process are described in-depth below and visualized in Fig. 2.

1. Start with a pixel on camera 1, which has phase pair $\phi_{h,1}(n, m)$ and $\phi_{v,1}(n, m)$, where n and m are denoting a pixel in the n^{th} row and m^{th} column on the detector plane.
2. The first interpolated window on camera 2 is identified with its center at (x_0, y_0) on camera 2 by finding the location that has the minimum root sum squares (RSS) phase difference from the current (n, m) pixel on camera 1:

$$\left([\varphi_{h,2}(x, y) - \varphi_{h,1}(n, m)]^2 + [\varphi_{v,2}(x, y) - \varphi_{v,1}(n, m)]^2 \right)^{\frac{1}{2}} = \min \quad (4)$$

where (x, y) denotes the pixel locations across the entire image.

3. Create a local 5×5 window centered on the matched pixel (x_0, y_0) for each vertical and horizontal phase distribution on camera 2, and linearly interpolate the window $5 \times$, producing a 25×25 frame. This is the 0^{th} interpolated layer.
4. Step 2 is then repeated, but now finding the optimal pixel location on the 0^{th} interpolated layer only. We then search for $\mathbf{r}_0^* = (x_0^*, y_0^*)$ on layer 0 where we obtain the best matched phase, in other words:

$$\left([\varphi_{h,2}(x^*, y^*) - \varphi_{h,1}(n, m)]^2 + [\varphi_{v,2}(x^*, y^*) - \varphi_{v,1}(n, m)]^2 \right)^{\frac{1}{2}} = \min \quad (5)$$

where $(x^*, y^*) \in \mathcal{N}$ is denoting the location on the small neighborhood of 25×25 (sub)pixels in the 0^{th} layer.

5. Create a second interpolated layer taking the 5×5 pixel window around $\mathbf{r}_0^* = (x_0^*, y_0^*)$ and then interpolate it to build another 25×25 -(sub)pixel grid as the second layer \mathcal{N}_2 .
6. Repeat step 5 and 6 until the following convergence criterion is met:

$$\|\mathbf{r}_{l+1}^* - \mathbf{r}_l^*\|_2 < 0.01 \text{ pixel} \quad (6)$$

where $l = 0, 1, \dots$ is the super-resolution layer. Thus, \mathbf{r}_l^* indicates the best center location for the l -th interpolated layer. The number of iterations it takes to meet this criterion varies from 1 to 5, depending on the amount of overlapping projected area on the object of the pixel on camera 1 with a corresponding pixel in camera 2.

7. Repeat the entire process for each pixel on camera 1.

Effects such as projector nonlinear brightness, temporal and spatial brightness fluctuations and lens distortion errors are eliminated since phase is not used directly to determine depth, but is simply a fiducial to assist determining parallax of stereo vision [41]. Applying this process to each pixel results in highly accurate subpixel feature matching, which leads to high depth resolution, high spatially sampled 3D point clouds representing the surface figure.

3.1. Calibration

To demonstrate the predicted accuracy of this technique over large areas, we assembled an example system to cover an area of 1 m^2 . We used two 20 megapixel FLIR Blackfly USB3 cameras with Sony IMX183 sensors and 12 mm focal length lenses. For the projector, we used a 1080P Optoma GT1080HDR Short Throw Gaming Projector, which allows pattern projection over a large area from a short working distance. The sensor pixel size was $2.4 \mu\text{m}$, the baseline distance was 2.5 meters and the object distance was 1 meter (Fig. 3). Based on Eq. (3), this should produce a depth resolution of $80 \mu\text{m}$ assuming a one pixel disparity error, however the performance should be significantly improved by using interpolated stereo matching. The two

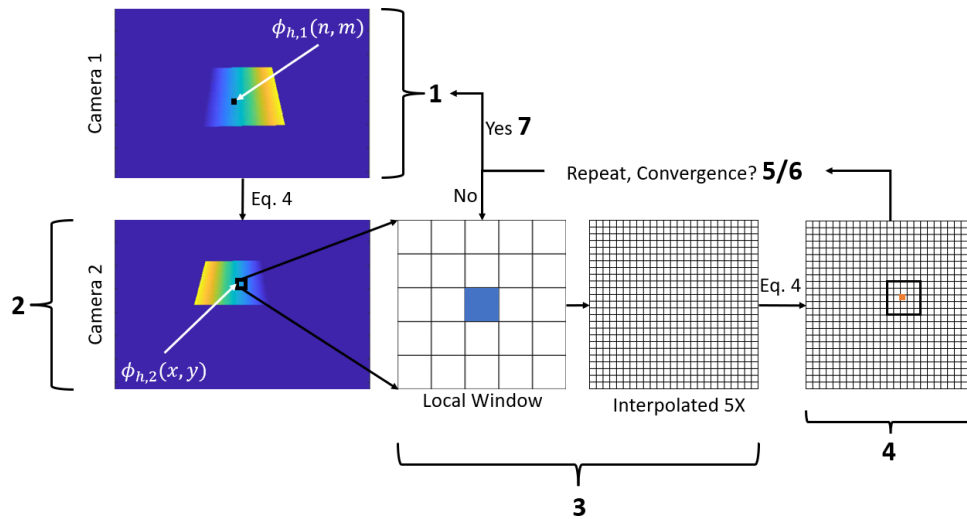


Fig. 2. Precision stereo matching process shown for the horizontal phase only, for simplicity. Actual algorithm used vertical and horizontal phase. With the vertical direction included in the matching process, there is a small window where the best matched phase pair must exist.

cameras were calibrated using MATLAB’s Camera Calibrator for the intrinsic parameters and the Stereo Camera Calibrator App for extrinsic parameters, calibrating only for radial distortion, since these well-made cameras should have negligible tangential distortion. This software uses Zhang’s well-known method [33]. We used 19 images of a 22x23 black and white checkerboard with 15 mm squares in a variety of locations and orientations within the field of view. The calibration involved covering the entire field of view of both cameras, near the planned working distance of the measurement surface. Figure 4 shows the camera layout with sampled locations of the calibration target as well as the corresponding reprojection error.

The mean reprojection error shown in Fig. 4 of the calibration process was 0.16 pixels. While this may seem like the limiting factor in accuracy based on Eq. (3), it is only the limiting factor in calibration. Errors in calibration due to the calibration board itself (such as board flatness, gravity deformation, and sharpness of checkerboard corners) as well as noise in the corner finding algorithm limits the calibrated reprojection error. It has been shown in other research that measurements of real objects are required to evaluate the actual accuracy of a stereo-camera calibration [42]. For this reason we will focus on measuring real objects in Section 4.

It is important to note that this is just one embodiment of the system. In theory any combination of camera types (pixel size, array size, focal length) can be used in combination with any projector. The only requirements to obtain a 3D point on the surface is that both cameras see the same area on the object, and the projector also covers that area.

3.2. Data acquisition and processing

We employ an 11-step phase shifting algorithm in both orthogonal directions, making a total of 22 captured images for each camera, 44 images in total. Using 11 phase steps helps to reduce noise in the final measured phase maps [43,44]. Equation (2) is used to recover the wrapped phase, and the spatial phase unwrapping method based on reliability sorting from Herraez et. al. [29] is used to recover the unwrapped phase maps for each camera.

The technique in Section 2 is then used to match each pixel on camera 1 to a location on camera 2, producing a set of matched feature points. Each set of matched points is then triangulated using the calibrated intrinsic and extrinsic parameters to produce the final 3D object [45].

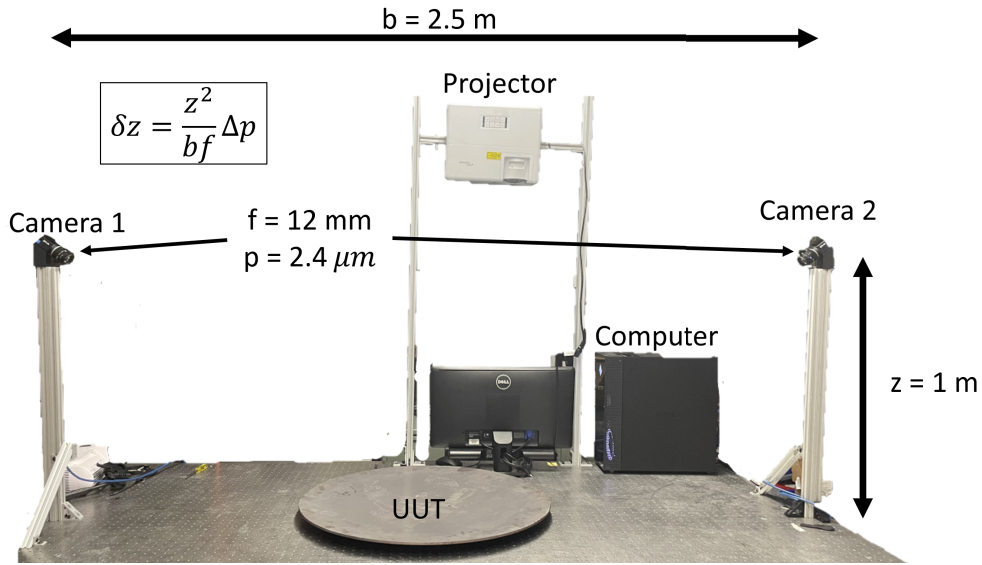


Fig. 3. Actual system layout of cameras, projector, computer and unit under test (UUT). Note the rough placement of the projector. The only requirement is that the projector completely covers the UUT with fringes. The measurement is only made by stereo matching, so only the cameras require a stable mounting scheme. This configuration produces an expected depth resolution of $80 \mu\text{m}$ assuming one pixel of disparity error, but we expect the interpolated phase matching method to significantly reduce this.

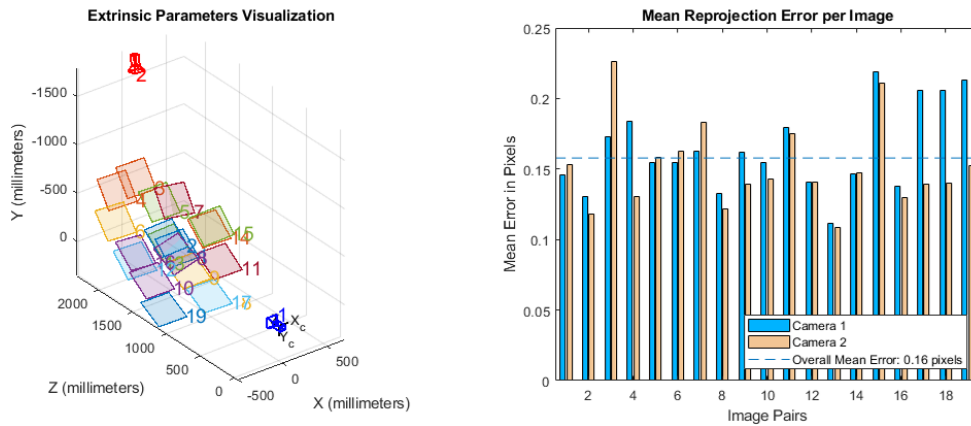


Fig. 4. Layout of extrinsic parameters and calibration target locations (left) and their corresponding reprojection errors for each camera (right).

4. Demonstrations

4.1. Flatness accuracy

One of the challenges of claiming high resolution measurements is verifying it with a known test object. We expect the system to produce depth resolution of $80 \mu\text{m}$ for a disparity error of 1 pixel, so a good candidate test surface would ideally have a much higher accuracy. One of the industry standards for a high performing structured light system is the ATOS 5 produced by GOM. It lists a max-permissible error (MPE) of $38 \mu\text{m}$ and a typical certification result for VDI-2634

of $26\ \mu\text{m}$ over a 0.75m square measurement area [46]. Granite surface plates commonly have surface flatness in this range. We measured a 9×12 " Grade B granite surface plate, with specified root-mean-square (RMS) flatness accuracy of $5.1\ \mu\text{m}$. Figure 5 shows some sample images of the projected fringes as seen from each camera, as well as an example wrapped and unwrapped phase for vertical fringes as seen from Camera 1.

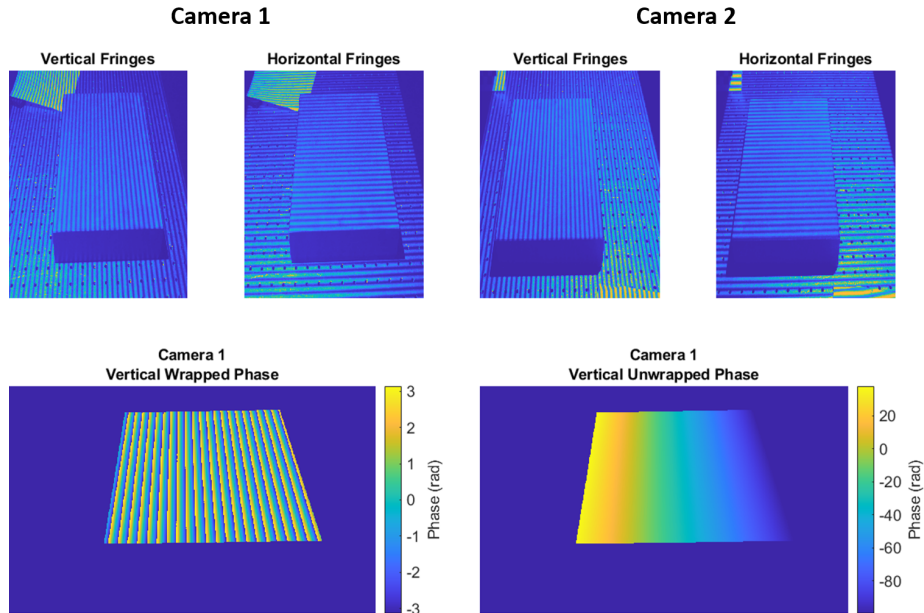


Fig. 5. Shown are images of the first phase step for horizontal and vertical fringes, seen from both cameras (top). Also shown is a masked image of just the granite surface, with the wrapped phase shown (bottom left) and the unwrapped phase (bottom right). Shown is only the wrapped and unwrapped phase for one fringe direction and for one camera, for simplicity.

Figure 6 shows the actual granite surface plate that was measured along with the final measurement using the interpolated stereo matching method, along with the final measured point cloud with plane fit subtracted, which has 1.29 million points and a $5.2\ \mu\text{m}$ RMS error. Note that much of the error in Fig. 6 is high spatial frequency, not low order error, demonstrating the overall shape accuracy of this system. Compared to the theoretical depth resolution of $80\ \mu\text{m}$ assuming one pixel of disparity error, this measurement would imply that the system is capable of subpixel matching up to at least $80\ \mu\text{m}/5.2\ \mu\text{m} = 1/15$ pixels. While this measurement is not the same as the certifications used in VDI-2634 for the ATOS 5, it does provide some validation that the overall measured shape of a continuous surface is accurate. The time from beginning of the fringe image acquisition to interpolated reconstructed surface is less than 5 minutes. Most of the measurement time is attributed to image acquisition, requiring 3 second exposures between phase steps due to the large measurement area and the relatively low-brightness of the off-the-shelf projector. The ATOS 5 system advertises up to 0.2 second acquisition times, using a custom high-powered LED or laser projector, but the total processing time is not listed. It is important to note that our developed solution is not designed to produce extremely high speed measurements.

4.2. Highly specular machined surfaces

We also applied this measurement method to measuring the low-order shape residual of a prototype secondary reflector panel designed for the next-generation Very Large Array (ngVLA). The surface was machined on a CNC mill. The surface aperture is hexagonal, 750 mm in the

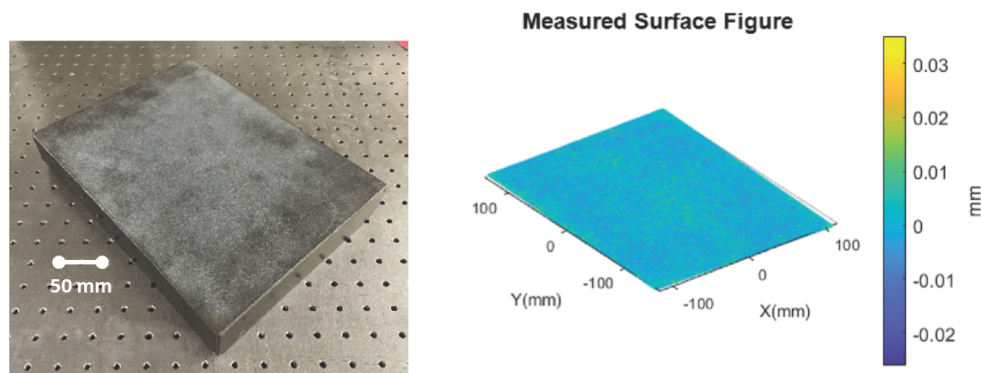


Fig. 6. Grade B granite surface flat (left) and the measured flat top surface (right). RMS fit error to a plane is $5.1 \mu\text{m}$.

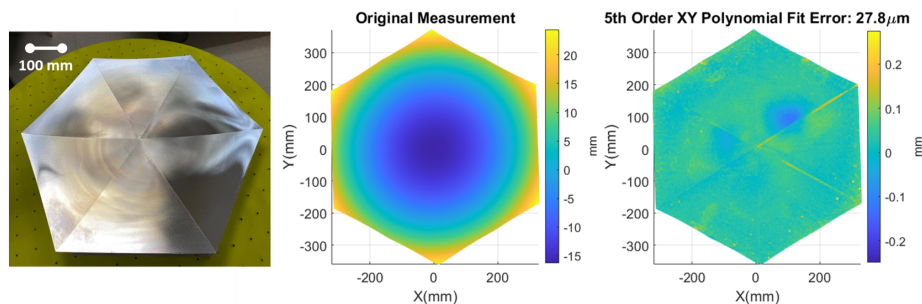


Fig. 7. Image of hexagonal prototype panel (left), its measurement (middle) and 5th order XY polynomial residuals (right). After subtracting low order shape up to 5th order, errors due to surface machining and support structure are revealed.

longest dimension. The prescribed low-order shape was not made available, so this example is used to visualize mid- and high-spatial frequency errors in the surface. The surface was fit to a 5th order XY polynomial and this polynomial was subtracted from the point cloud in order to visualize the higher frequency errors in the surface. The residual has an RMS of $27.8 \mu\text{m}$, which meets the panels accuracy requirement of $40 \mu\text{m}$ RMS, assuming the 5th order shape is correct. The measurement data (shown in Fig. 7) illustrates the capability of this method to measure beyond the overall low-order shape of a surface, which is often the extent of information provided by other methods like CMMs or laser trackers. In addition, no surface treatment is required, even though the surface has a strong specular component. There is still a small diffuse component, so simply increasing the exposure time to capture more light scattered from the surface from the projector is sufficient. The projector was positioned so that specular reflections from the surface did not enter the camera aperture. Total measurement time is increased due to the required long exposure, but for the application of radio telescope panels, it is still a very small portion of the total manufacturing time and will not become a bottleneck of the process. Small scale structures of tooling marks on the surfaces are easily resolved using this interpolated matching method, which gives insight into how the reflector may perform while focusing high frequency radio waves. This information provides valuable feedback to the effects of different panel manufacturing processes.

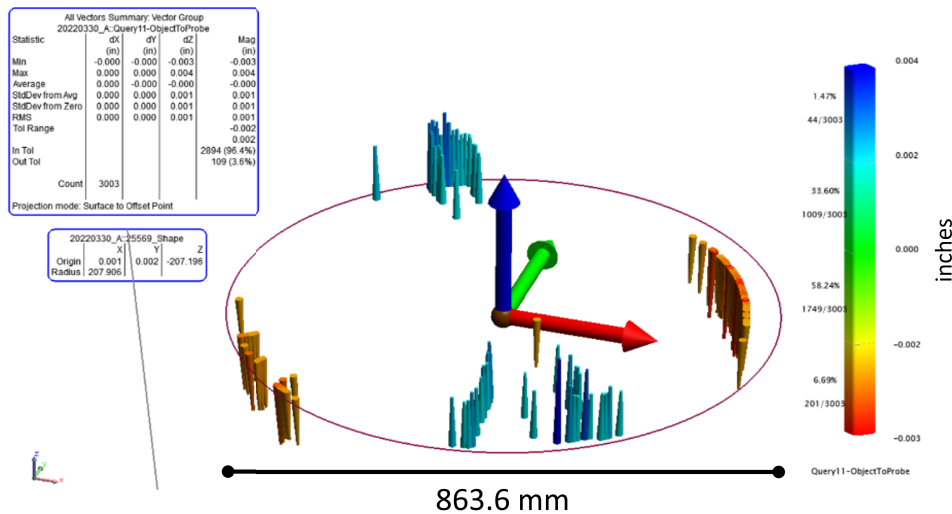


Fig. 8. Shown is a screenshot of the laser tracker measurement report. The black circle represents the outer boundary of the steel mold surface. The table in the top left shows a summary of the measurement results compared to the ideal 5.275 m radius sphere. The red and blue spikes show the measured points with the largest deviation from the ideal sphere, blue being too low and red being too high. Best fit radius reported was $R = 5.281$ m. The blue and red spikes indicate astigmatism in the surface of about $0.007''$, or $175 \mu\text{m}$, peak to valley.

4.3. Laser tracker comparison

We also applied this measurement method to verifying the accuracy of a convex steel dish designed as a negative for thermally forming concave glass mirror substrates. The surface is spherical and was originally specified for a radius of curvature of 5.275 m and a circular aperture 863.6 mm in diameter. The mold was measured with a laser tracker by a third party company, data report shown below in Fig. 8. The laser tracker has $0.001''$ resolution, or $25.4 \mu\text{m}$.

The mold was also measured with the FPP method described in this paper and the system shown in Fig. 3. With the best fit sphere removed from the measurement data ($R = 5.292$ m), astigmatism is revealed along with some higher order structure. Compared to the laser tracker measurement, the difference in measured radii is only 0.21%. The fringe projection measurement shows a peak to valley astigmatism of $183 \mu\text{m}$, on the same order of magnitude as the laser tracker measurement, $175 \mu\text{m}$. Overall, there is much agreement between the well-established metrology method (laser tracker) and the proposed FPP method, especially considering that the laser tracker only reads-out with $25 \mu\text{m}$ resolution. Removing a 2^{nd} order XY polynomial fit (power and astigmatism) reveals an underlying grid structure, which matches the configuration of steel ribs welded onto the back of the dish, which is the main source of the surface RMS error, after astigmatism. This measurement (Fig. 9) illustrates the capability of this method to measure beyond overall low-order shape of a surface, revealing other causes of error that is not resolved by the laser tracker measurement, and would not be resolved by a CMM or fiducial-based photogrammetry either.

4.4. Large-scale surfaces

We scaled up the system further to measure a $1.8 \text{ m} \times 1.8 \text{ m}$ deformable mold that was designed to shape freeform heliostat mirrors and radio telescope panel segments (Fig. 10). In order to deform the surface to approach the ideal shape, there are many linear actuators that can be adjusted, but a

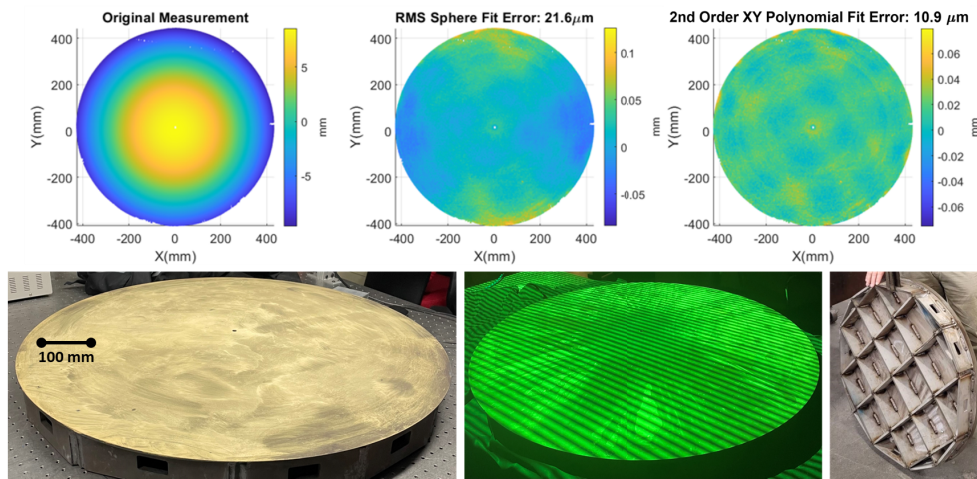


Fig. 9. Measurements of 863.6 mm steel mold. Shown above is the original measurement (upper left), the sphere fit error (upper middle), the 2nd order XY polynomial fit error (upper right), and images of the measured surface (lower left), projected fringe pattern, and the support structure underneath the surface (lower right). After subtracting low order shape, the underlying rib structure is seen 'printing through' the surface.

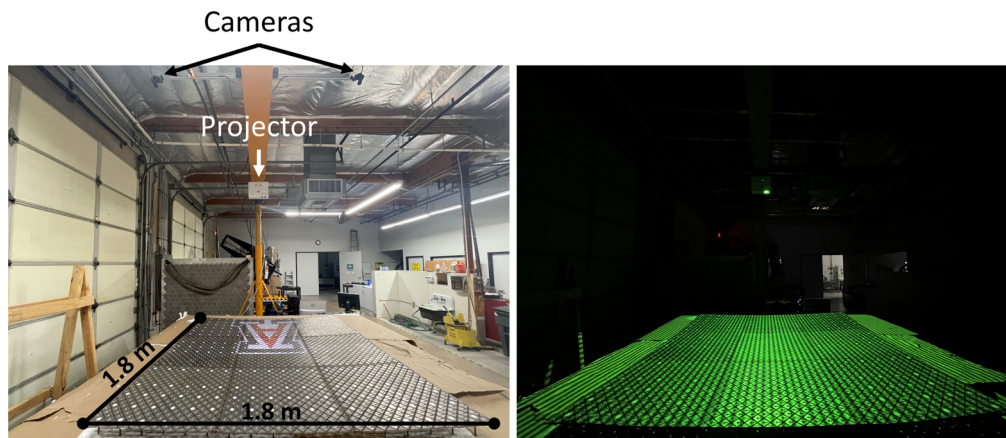


Fig. 10. Layout of measurement system for 1.8 x 1.8 m adjustable mold (left) and an image of the projected fringes on the surface (right). Camera baseline is 2 m, and distance to the surface is 2.5 m.

measurement of the surface is needed in order to provide feedback. The surface is complicated, with hundreds of square tiles connected with thin blade flexures. At this size, the surface is too large for nearly all portable or permanent CMMs. The same cameras and lenses as in the previous measurement examples were used, but with a 2 m baseline distance and a camera to UUT distance of about 2.5 m.

Here, the modulation (difference between maximum and minimum brightness at each pixel through the data series of phase shifted fringes) of the phase was used to mask 3D points that were not on the surface. The ideal surface for the adjustable mold is an off-axis hyperboloidal segment, which was subtracted from the measured map to give a residual map. This residual map is crucial feedback for driving the linear actuators that control the mold surface shape and

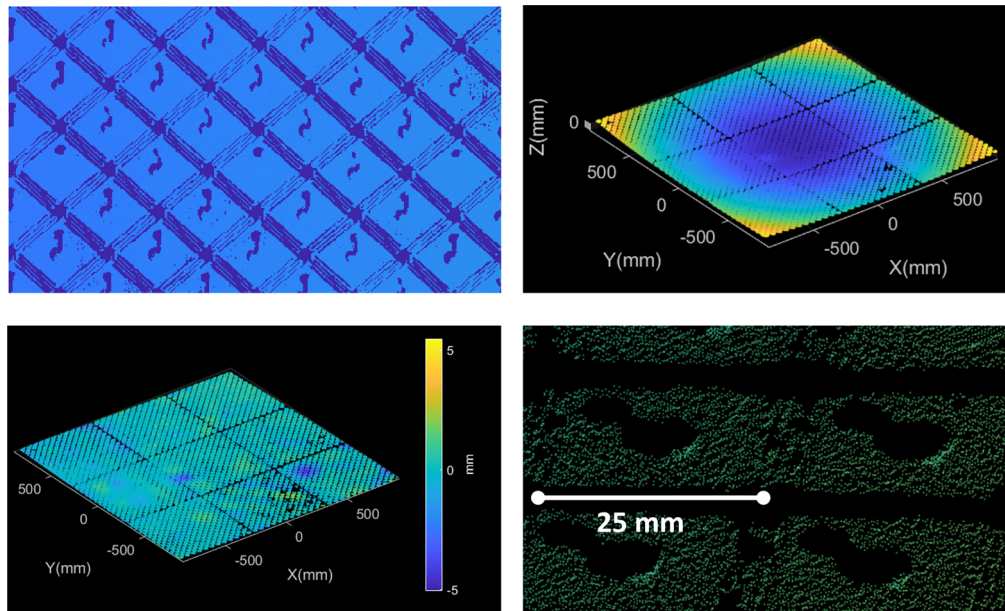


Fig. 11. Example image used to mask camera images taken of the mold surface (top left) using a modulation threshold to identify pixels that are on the mold surface. 3D map of the raw data with 4.6 million measured points (top right) and a 3D map of the residual with the ideal shape subtracted. Bottom right image is a zoomed in view of the measurement to demonstrate the point density over each 25 x 25 mm square tile.

develop this method for shaping metal and glass with a deformable mold. Measurement data from the surface is shown in Fig. 11.

4.5. Discussion

This method provides a variety of advantages over other types of 3D surface profiling systems. The accuracy over a 9"x12" granite flat is higher than commercial FPP systems [20,46], which often specifies accuracy on the order of 0.025 mm, and is comparable or better than the metrology methods used to measure rough surfaces as discussed in Section 1 based on measurement time, accuracy, flexibility, and spatial resolution. While the total measurement and processing time is slower than other commercial FPP systems, the method described in this paper has not yet been optimized with custom hardware, in the form of brighter projectors, more processing power, and framegrabbers for faster camera readout. This FPP method can measure millions of points across a square meter, making the spatial resolution on the order of 1 mm^2 . Because CMMs and laser trackers only measure a single point at a time, a comparable spatial resolution measurement would take many weeks of constant sampling, assuming a few seconds for each sample point. An IR interferometer may have similar spatial resolution by viewing the surface with a high resolution IR camera, but measurements require a unique configuration for every type of surface shape. This FPP method is capable of measuring any surface that can be simultaneously seen by both cameras and the projector, allowing for a wide range of convex, concave, and freeform surfaces. Calibration of the system is simple and well-established, and can be done with a standard checkerboard pattern, compared to other FPP methods that may require extra steps for projector calibration. The method is also tolerant to errors in the projector. Since the projector acts simply as a fiducial generator, phase errors due to gamma brightness distortion and temporal brightness variation are common to both cameras, which have negligible effect on the ability to

match features, and ultimately allows retrieval of accurate point measurements. The hardware cost of the system is low, requiring only off-the-shelf machine vision cameras, a gaming projector, and a computer: far less than the cost of comparable CMM, laser tracker, or IR interferometer. These properties make it a valuable, flexible method for use in the development of new surface forming techniques, as shown in sections 4.2–4.4.

One drawback of this system is it is difficult to get feedback on a poor measurement or calibration, and establish a ground truth measurement. Reprojection errors in the calibration generally aren't relied upon for verifying a good calibration. Currently what is needed is measurement of a surface that is verified using some other metrology method. While low order shape accuracy verification may be simple to do for small objects by using a small granite surface flat as in Section 4.1, truly verifying the accuracy of a measurement over a larger area $>1 \text{ m}^2$ would be significantly more challenging as the size, weight and cost of reference surfaces increase. In addition, another drawback is this method is generally designed for continuous surfaces with slow curvature. If the surface has disconnected components, or a fast curvature, this method would need to be adjusted to accommodate, likely with a different phase-shifting method and error handling in the data processing, or measurements of sections of the surface separately. Due to the long baseline of the camera configuration, there is also a limit to slope variation that can be measured, shown in Fig. 12. If the surface slope becomes high, one camera may observe a section of the object at a larger angle than the other camera. This causes one pixel on one camera to represent a much larger area on the object than the corresponding pixel on the other camera (Fig. 12(b)). Eventually, the slope could become so high that one camera cannot see a patch of surface at all (Fig. 12(c)). There is likely some accuracy degradation associated with stereo vision measurement of highly sloped surfaces, but this is beyond the scope of this paper.

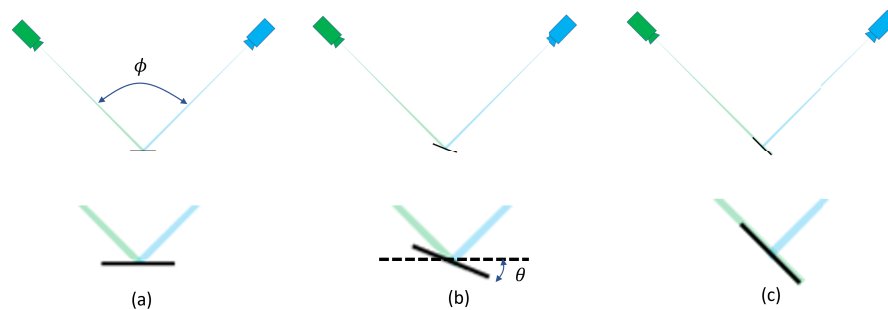


Fig. 12. Shown is an SV system measuring a small, flat patch of surface that is seen at an equal angle from each camera (a). As the slope of the surface changes, as in (b), the projected area of a pixel on one camera exceeds the projected area of the same corresponding pixel on the other camera. When the slope (θ), is equal to half of the angle between the cameras (ϕ), the measurement is not possible. This is a fundamental limitation of the SV system.

5. Conclusion

We have developed a novel high-accuracy measurement method for large, rough surfaces based on FPP with two cameras, achieving an RMS accuracy of $5.2 \mu\text{m}$. The system is simple to calibrate, is low-cost, produces densely sampled surface maps, and is relatively rapid. These properties make it an ideal measurement solution for surfaces that require high accuracy as well as visible light scattering properties, without significant time restraint requirements, namely surfaces used for radio astronomy and satellite communication. The authors hope that this method may contribute to the development of manufacturing and metrology technologies needed for future large telescopes.

Funding. National Science Foundation (2009384).

Disclosures. Author Joel Berkson has a financial connection to Fringe Metrology LLC, a company that measures freeform surfaces using some of the technologies described in this paper. Justin Hyatt has a financial connection to Paramium Technologies LLC, a company that fabricates freeform curved metal surfaces.

Data availability. Data underlying the results presented in this paper are not publicly available at this time but may be obtained from the authors upon reasonable request.

References

1. J. Cheng, *The Principles of Astronomical Telescope Design*, vol. 360 (Springer New York, 2009).
2. C. Davila-Peralta, J. Hyatt, Z. Hatfield, A. S. Peter, B. S. Allen, N. Nguyen, W. Ellis, D. W. Kim, J. Berkson, and E. Rodriguez, "Electromagnetic thermoforming to manufacture reflective panels for radio telescopes and downlinks," in *2021 IEEE Aerospace Conference (50100)*, (IEEE, 2021), pp. 1–15.
3. J. W. Baars and H. J. Kärcher, *Radio Telescope Reflectors*, vol. 447 (Springer, 2018).
4. G. Valsecchi, J. Eden, G. Grisoni, C. van't Klooster, and L. Fanchi, "High precision electroformed nickel panel technology for sub-millimeter radio telescope antennas," in *IEEE Antennas and Propagation Society International Symposium. Digest. Held in conjunction with: USNC/CNC/URSI North American Radio Sci. Meeting (Cat. No. 03CH37450)*, vol. 1 (IEEE, 2003), pp. 124–127.
5. P.-S. Kildal, "Some reflector and feed antenna inventions that made a difference: Fundamentals and examples from radio telescopes, satellite communications and radio links," 2013 Africon pp. 1–3 (2013).
6. D. M. Gale, M. L. Álvarez, L. C. Cuevas, A. Leon-Huerta, E. A. Reyes, O. I. Hernández, D. C. Santos, E. H. Ríos, E. T. Sosa, C. T. Torres, and M. V. Alonso, "Coordinate metrology of a primary surface composite panel from the large millimeter telescope," in *Advances in Optical and Mechanical Technologies for Telescopes and Instrumentation II*, vol. 9912 (International Society for Optics and Photonics, 2016), p. 991211.
7. Y. Zhang, D. Yang, Y. Li, G. Zhou, A. Li, G. Li, and Z. Zhang, "A new efficient laser angle metrology system for maintaining the large radio telescope active reflecting antenna," in *Ground-based and Airborne Telescopes III*, vol. 7733 (SPIE, 2010), pp. 1261–1268.
8. M. Wang, D. Li, and Y. Zhao, "Iterative alignment of reflector panels for large-scale compact test range in non-metrology environment based on laser tracker," *Meas. Sci. Technol.* **31**(4), 045002 (2020).
9. W. T. Estler, K. Edmundson, G. Peggs, and D. Parker, "Large-scale metrology—an update," *CIRP Ann.* **51**(2), 587–609 (2002).
10. R. Enriquez and C. E. Sampieri, "Surface metrology using laser trackers," in *Eighth International Symposium on Laser Metrology*, vol. 5776 (SPIE, 2005), pp. 568–575.
11. T. Schenk, "Introduction to photogrammetry," The Ohio State University, Columbus 106, 1 (2005).
12. R. Subrahmanyam, "Photogrammetric measurement of the gravity deformation in a cassegrain antenna," *IEEE Trans. Antennas Propag.* **53**(8), 2590–2596 (2005).
13. M. Rimpler, S. Daftry, A. Tscharf, R. Pretenthaler, C. Hoppe, G. Mayer, and H. Bischof, "Automated end-to-end workflow for precise and geo-accurate reconstructions using fiducial markers," *ISPRS Annals Photogramm. Remote Sens. Spatial Inf. Sci.* **II-3**, 135–142 (2014).
14. S. Zhang, "High-speed 3d shape measurement with structured light methods: A review," *Opt. Lasers Eng.* **106**, 119–131 (2018).
15. S. Van der Jeught and J. J. Dirckx, "Real-time structured light profilometry: a review," *Opt. Lasers Eng.* **87**, 18–31 (2016).
16. S. Zhang, *Handbook of 3D Machine Vision: Optical Metrology and Imaging* (CRC press, 2013).
17. S. S. Gorthi and P. Rastogi, "Fringe projection techniques: whither we are?" *Opt. Lasers Eng.* **48**(2), 133–140 (2010).
18. Y. Yongkai, Z. Zonghua, L. Xiaoli, and P. Xiang, "Review of the system model and calibration for fringe projection profilometry," *Infrared Laser Eng.* **49**(3), 303008 (2020).
19. S. Feng, C. Zuo, L. Zhang, T. Tao, Y. Hu, W. Yin, J. Qian, and Q. Chen, "Calibration of fringe projection profilometry: A comparative review," *Opt. Lasers Eng.* **143**, 106622 (2021).
20. Y. Hu, Q. Chen, S. Feng, and C. Zuo, "Microscopic fringe projection profilometry: a review," *Opt. Lasers Eng.* **135**, 106192 (2020).
21. Z. Lei, C. Wang, and C. Zhou, "Multi-frequency inverse-phase fringe projection profilometry for nonlinear phase error compensation," *Opt. Lasers Eng.* **66**, 249–257 (2015).
22. J. M. Huntley and C. Coggrave, "Optimization of a shape measurement system based on spatial light modulators," in *Laser Metrology and Inspection*, vol. 3823 (SPIE, 1999), pp. 104–114.
23. S. Zhang and P. S. Huang, "Phase error compensation for a 3-d shape measurement system based on the phase-shifting method," *Opt. Eng.* **46**(6), 063601 (2007).
24. P. S. Huang, Q. J. Hu, and F.-P. Chiang, "Double three-step phase-shifting algorithm," *Appl. Opt.* **41**(22), 4503–4509 (2002).
25. C. Zuo, S. Feng, L. Huang, T. Tao, W. Yin, and Q. Chen, "Phase shifting algorithms for fringe projection profilometry: A review," *Opt. Lasers Eng.* **109**, 23–59 (2018).
26. S. Zhang, "Absolute phase retrieval methods for digital fringe projection profilometry: a review," *Opt. Lasers Eng.* **107**, 28–37 (2018).

27. C. Zuo, L. Huang, M. Zhang, Q. Chen, and A. Asundi, "Temporal phase unwrapping algorithms for fringe projection profilometry: A comparative review," *Opt. Lasers Eng.* **85**, 84–103 (2016).
28. Z. Zhang, "Review of single-shot 3d shape measurement by phase calculation-based fringe projection techniques," *Opt. Lasers Eng.* **50**(8), 1097–1106 (2012).
29. M. A. Herráez, D. R. Burton, M. J. Lalor, and M. A. Gdeisat, "Fast two-dimensional phase-unwrapping algorithm based on sorting by reliability following a noncontinuous path," *Appl. Opt.* **41**(35), 7437–7444 (2002).
30. J. Xu and S. Zhang, "Status, challenges, and future perspectives of fringe projection profilometry," *Opt. Lasers Eng.* **135**, 106193 (2020).
31. A. Mu noz, J. L. Flores, G. Parra-Escamilla, L. A. Morales, S. Ordonez, and M. Servin, "Least-squares gamma estimation in fringe projection profilometry," *Appl. Opt.* **60**(5), 1137–1142 (2021).
32. T. Hoang, B. Pan, D. Nguyen, and Z. Wang, "Generic gamma correction for accuracy enhancement in fringe-projection profilometry," *Opt. Lett.* **35**(12), 1992–1994 (2010).
33. Z. Zhang, "A flexible new technique for camera calibration," *IEEE Trans. Pattern Anal. Machine Intell.* **22**(11), 1330–1334 (2000).
34. M. Kytö, M. Nuutinen, and P. Oittinen, "Method for measuring stereo camera depth accuracy based on stereoscopic vision," in *Three-Dimensional Imaging, Interaction, and Measurement*, vol. 7864 (SPIE, 2011), pp. 168–176.
35. D. Gallup, J.-M. Frahm, P. Mordohai, and M. Pollefeys, "Variable baseline/resolution stereo," in *2008 IEEE conference on computer vision and pattern recognition*, (IEEE, 2008), pp. 1–8.
36. R. Zhang, Y. Xiao, J. Cao, and H. Guo, "Rapid matching of stereo vision based on fringe projection profilometry," in *8th International Symposium on Advanced Optical Manufacturing and Testing Technologies: Optical Test, Measurement Technology, and Equipment*, vol. 9684 (International Society for Optics and Photonics, 2016), p. 96840K.
37. H. Zhao, Z. Wang, H. Jiang, Y. Xu, and C. Dong, "Calibration for stereo vision system based on phase matching and bundle adjustment algorithm," *Opt. Lasers Eng.* **68**, 203–213 (2015).
38. R. Yang, S. Cheng, W. Yang, and Y. Chen, "Robust and accurate surface measurement using structured light," *IEEE Trans. Instrum. Meas.* **57**(6), 1275–1280 (2008).
39. T. Fetzter, G. Reis, and D. Stricker, "Fast projector-driven structured light matching in sub-pixel accuracy using bilinear interpolation assumption," in *International Conference on Computer Analysis of Images and Patterns*, (Springer, 2021), pp. 26–36.
40. F. Zhong, R. Kumar, and C. Quan, "A cost-effective single-shot structured light system for 3d shape measurement," *IEEE Sens. J.* **19**(17), 7335–7346 (2019).
41. C. Yu, F. Ji, J. Xue, and Y. Wang, "Adaptive binocular fringe dynamic projection method for high dynamic range measurement," *Sensors* **19**(18), 4023 (2019).
42. D. Moreno and G. Taubin, "Simple, accurate, and robust projector-camera calibration," in *2012 Second International Conference on 3D Imaging, Modeling, Processing, Visualization & Transmission*, (IEEE, 2012), pp. 464–471.
43. M. Servin, J. Estrada, and J. A. Quiroga, "The general theory of phase shifting algorithms," *Opt. Express* **17**(24), 21867–21881 (2009).
44. Y. Surrel, "Design of algorithms for phase measurements by the use of phase stepping," *Appl. Opt.* **35**(1), 51–60 (1996).
45. R. Hartley and A. Zisserman, *Multiple View Geometry in Computer Vision* (Cambridge university press, 2003).
46. "Atos 5: High-speed 3D scanning: For industrial demands," <https://www.gom.com/en/products/high-precision-3d-metrology/atos-5/>. Accessed 2022-10-14.

APPENDIX C

Systematic Radio Telescope Alignment using Portable Fringe Projection
Profilometry

Joel Berkson, Justin Hyatt, Nathan Julicher, Byeongjoon Jeong, Isaac Pimienta,
Rachel Ball, Wyatt Ellis, Jason Voris, Diego Torres-Barajas, Daewook Kim

Journal article submitted to

Springer Nanomanufacturing and Metrology

Special Issue: Astronomical Optics Manufacturing and Testing

*Author information removed from submitted reprint for double-blind peer review
from Springer.*

Systematic Radio Telescope Alignment using Portable Fringe Projection Profilometry

First Author^{1,2*}, Second Author^{2,3†} and Third Author^{1,2†}

¹*Department, Organization, Street, City, 100190, State, Country.

²Department, Organization, Street, City, 10587, State, Country.

³Department, Organization, Street, City, 610101, State, Country.

*Corresponding author(s). E-mail(s): iauthor@gmail.com;

Contributing authors: iauthor@gmail.com; iiiauthor@gmail.com;

†These authors contributed equally to this work.

Abstract

In 2019, the Event Horizon Telescope (EHT) released the first ever image of a black hole event horizon. Astronomers are now aiming for higher angular resolutions of distant targets, like black holes, to understand more about the fundamental laws of gravity that govern our universe. To achieve this higher resolution and increased sensitivity, larger radio telescopes are needed to operate at higher frequencies and in larger quantities. Projects like the next-generation Very Large Array (ngVLA) and the Square-Kilometer Array (SKA) require building hundreds of telescopes with diameters greater than 10-meters over the next decade. This has a two-fold effect. Radio telescope surfaces need to be more accurate to operate at higher frequencies, and the logistics involved with maintaining a radio telescope needs to be simplified to properly support them in large quantities. Both of these problems can be solved with improved methods for surface metrology that are faster, more accurate, and have higher resolution. This leads to faster and more accurate panel alignment and therefore a more productive observatory. In this paper, we present the use of binocular fringe projection profilometry as a solution to this problem, and demonstrate it by aligning two panels on a 3-meter radio telescope dish. The measurement takes only 10 minutes, and directly delivers feedback for tip, tilt, and piston of each panel to create the ideal reflector shape.

Keywords: metrology, fringe projection profilometry, off-axis alignment, radio astronomy, radio antenna

1 Introduction

Radio astronomy is used to observe the night sky through a different lens than optical astronomy; able to see the unseen. The manufacturing paradigms are also significantly different. In radio astronomy, direct recording of radio wave phase information can be done for GHz frequencies, meaning that signals from radio telescopes separated by great distance can be correlated in post-processing to achieve angular resolution far better than optical telescopes. This is clearly demonstrated by the Event Horizon Telescope (EHT) forming images of black hole event horizons with micro-arcsecond resolution[1, 24]. The usage of longer wavelengths in radio astronomy proportionally loosens the accuracy requirements of the main reflector compared to optical counterparts. The trade-off is that much larger reflectors are required to obtain good signal-to-noise (SNR) ratio, as the radio signals are typically weaker than optical. It has been well known that optical telescopes scale cost with aperture diameter at approximately $D^{2.77}$. Fortunately, the cost of radio telescopes tend to scale at a rate closer to D^2 , increasing linearly with collecting area.[6, 17] As radio telescopes aim toward higher and higher resolutions, higher frequencies are required, and thus tighter requirements are imparted on the primary reflector. The Ruze equation describes how the surface root mean square (RMS) error of the reflector affects the antenna gain, where G_0 is the nominal gain considering a perfect reflector, ϵ is the surface RMS and λ is the wavelength, expressed in the same physical units.[22]

$$G(\epsilon) = G_0 e^{-\frac{4\pi\epsilon^2}{\lambda}} \tag{1}$$

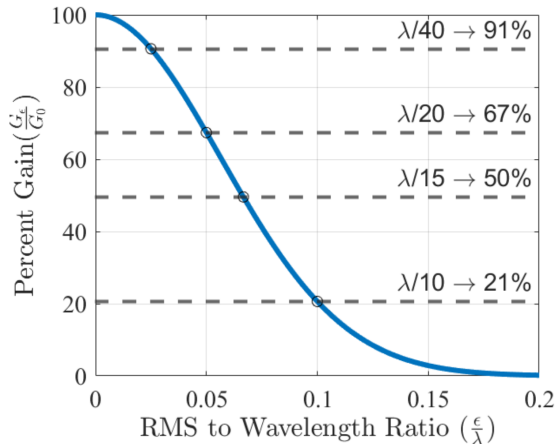


Fig. 1 Plotting the percent gain dictated by the Ruze Equation as a function of surface RMS to wavelength ratio. At $\lambda/15$, 3 dB loss, or 50%, is achieved.

Figure 1 shows the antenna gain degradation as a function of the RMS to wavelength ratio. A common bare minimum performance goal is to achieve a 3 dB loss (50%), which correlates to $\approx \lambda/15$. For example, the EHT observes at 230 GHz, a

1.3 mm wavelength. Thus to preserve antenna gain, the surface must meet $\approx 85 \mu m$ RMS. This RMS value includes the error stack-up from the individual panel accuracy, gravity deformations, temperature gradients, wind-shake, and panel misalignment.[5] Panel alignment and adjustment is a critical process to deploying a radio telescope to meet optimal gain. Manufacturing cost associated with making accurately-shaped panels is wasted if not properly aligned. If the status of panel to panel alignment and panel deformation is not known, then adjustments cannot occur.

Common methods to measure panel alignment and shape have historically included photogrammetry[9, 16, 26, 29], holography[4, 12, 25, 28] and laser trackers or laser trusses[8, 15, 29, 34]. Oftentimes, a combination of methods is used.[3, 23, 29, 32] All of these methods deliver the information on the surface accuracy of a dish, but they have many fundamental limitations and drawbacks. The spatial sampling of photogrammetry and laser trackers is limited to the number of fiducials or manually scanned points. The manual nature of these methods makes them time consuming and expensive, requiring large teams of researchers to execute the metrology. The University of Arizona recently tuned the alignment of dish panels in a 12 m diameter radio telescope using photogrammetry. It required a team of 3 (scientists and engineers) to work for two weeks. The accuracy of these methods also degrades with working distance, so as aperture size increases, the depth resolution decreases. For extremely large apertures observing with millimeter wavelengths, holography has been the default method to measure reflector deformations. Holography utilizes a smaller dish (that is assumed to be perfect) pointed at a satellite beacon (typically a geosynchronous satellite to avoid the need for tracking) as a reference signal. The antenna under test then raster scans across the source to sample the beam.[21, 36] Correlations with the reference signal are used to recover the absolute phase errors and inverse Fourier transforms are used to recover the aperture wavefront error, which feeds back to required surface adjustments to make corrections. While holography is known to have great sensitivity, it is limited in logistics. Specialized cryogenic detectors designed to match the frequency of the geosynchronous satellite beacon are required to take measurements. Also due to the use of geosynchronous satellites, only one elevation angle can be tested, meaning gravitational deformations at other elevation angles remain unknown. The measurements are time consuming due to the need to raster scan the entire telescope to sample the beam, and good environmental conditions are required for successful measurements. The algorithms to determine adjustments on the primary reflector vary largely from telescope to telescope depending on the size, on-axis versus off-axis configuration, as well as the presence of secondary or tertiary reflectors. Many future plans for large radio telescopes involve multiple off-axis reflectors.[13, 19, 30, 31]

It is clear that no matter what current metrology method is used on a radio antenna dish, there are drawbacks in cost, time, logistics, and data quality. Oftentimes, the use of multiple methods is required. In 2022, our research group developed a metrology technique based on binocular fringe projection profilometry for measuring radio telescope panels in a laboratory setting to assist our research into rapid fabrication of radio telescope panels[7]. As a demonstration of the panel forming technique, our research team is constructing a 2.4 x 3.2 meter radio telescope using our own fabricated panels,

known as the Student Radio Telescope (SRT)[10]. The problem of aligning the panels has driven the team to adapt the previously-developed panel metrology method to be portable, function outdoors, measure discontinuous objects, and cover large areas with high resolution. As a demonstration, we will show in this paper how the system can be used to deliver alignment feedback information for two adjacent panels on the SRT. The telescope is currently under construction for the purpose of public outreach. Figure 2 shows a 3D rendering of the SRT.

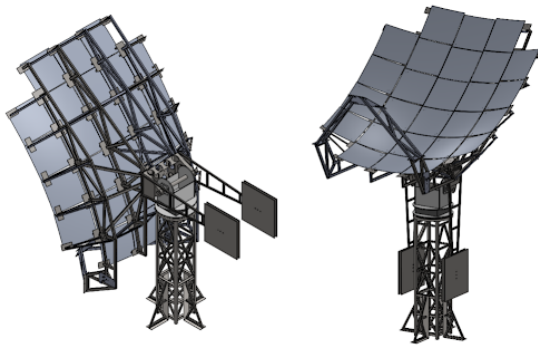


Fig. 2 3D rendering of the Student Radio Telescope. The telescope will be made up of 26, 500 mm x 500 mm panels, each with a different shape due to the off-axis paraboloid design.

2 Background

Before installing and aligning panels on a radio telescope, panels are manufactured and measured in a factory. Typically, Coordinate Measuring Machines (CMMs) are used to perform metrology on these surfaces to ensure they meet the required accuracy. However, as panels approach one or even two-meter size, CMMs become more costly and data collection becomes very slow. In 2022, our team developed a technique to measure panels and panel molds with a modification to fringe projection profilometry (FPP)[7]. The method uses two calibrated cameras (using Zhang’s method[37]) as a stereo pair, and a DLP projector. Figure 3 shows the current system based in the lab for measuring the mold and the panels. The projector displays a series of phase-stepped fringe patterns in vertical and horizontal directions onto a unit under test (UUT). The N-step phase shifting algorithm[39] is used to recover the wrapped phase of the patterns. The phase is then unwrapped using a spatial phase unwrapping method [27]. The resulting horizontal and vertical phase combination is unique for every projector pixel, and as a result, the series of patterns encodes the UUT with unique phase pairs. These phase pairs are used as fiducials to find matching points in the images captured by the two cameras. The calibrated intrinsic and extrinsic parameters of the stereo pair are used to triangulate the set of matching points to produce a 3D point cloud relative to the perspective of camera 1[11]. The nature of this method allows nearly every pixel that falls on the object to be converted into a 3D point.

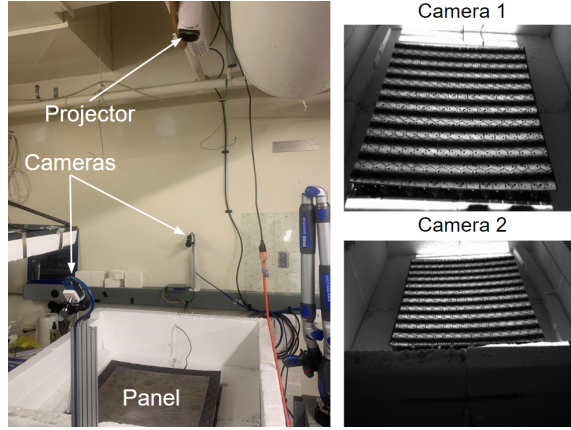


Fig. 3 Binocular FPP system in a laboratory setting. The system is used for measuring a flexible mold and measuring the panels that are thermally formed to it.

3 Methods

3.1 Binocular Fringe Projection Profilometry with Hierarchical Unwrapping

The previously described method does not work for discontinuous surfaces, as the spatial phase unwrapping for a single frequency only produces relative phase, not absolute phase. As a result, there is an integer multiple of 2π phase ambiguity between discontinuous objects, for example, two adjacent panels in a radio telescope, when using a spatial phase unwrapping method. To ensure reliable and absolute phase unwrapping, we have implemented a temporal phase unwrapping technique known as hierarchical, or multi-frequency, phase unwrapping[14]. The method uses an initial low frequency fringe period such that less than one period covers the entire span of the projected area, and thus has no 2π phase ambiguity. Consecutively higher and higher frequencies are used, with the lower frequency used to unwrap the next highest frequency, as in Eq. 2.

$$k_n(x, y) = \text{Round}\left(\frac{\frac{\lambda_{n-1}}{\lambda_n} \phi_{n-1}(x, y) - \phi_n(x, y)}{2\pi}\right) \quad (2)$$

$$\Phi_n(x, y) = \phi_n(x, y) + 2\pi k_n(x, y) \quad (3)$$

In Eq 2, n indicates the frequency being used, from lowest to highest. $k_n(x, y)$ is the map of fringe orders used to unwrap $\phi_n(x, y)$ to create the unwrapped map, $\Phi_n(x, y)$, for fringe period λ_n . The process of Eq 2 and 3 is done iteratively until the final highest frequency, or shortest fringe period, is reached. We used 5-step phase shifts for each fringe period of 1920, 500, 100, and 10 pixels. Fringe period 1920 matches the widest screen dimension for 1080P projectors, producing no unwrapping ambiguity. In theory, only the lowest frequency and the highest frequency are needed, but in the presence

of noise and imperfect fringe patterns, using multiple frequencies helps ensure proper identification of fringe orders for unwrapping each consecutive frequency[38].

3.2 Dish Measurement with Global Reference Frame

As mentioned in the Introduction, this stereo camera FPP system returns 3D data points relative to one of the camera axes. This is sufficient to align panels to one another to make the smoothest surface, but this surface needs to focus incoming radio signals to a known position. The SRT is an off-axis paraboloidal design, with a direct feed. To ease the process of determining a global reference frame, two circular fiducials are included in the FPP measurement field of view of SRT to define the optical axis of the telescope: at the paraboloid vertex and at the desired focal point.

These two fiducials will also be identified and triangulated in the stereo camera system, returning two 3D points relative to camera 1: $P_{vertex} = (X_{vertex}, Y_{vertex}, Z_{vertex})$ and $P_{focus} = (X_{focus}, Y_{focus}, Z_{focus})$. Their centers are identified using the Hough transform[2, 35]. We perform the following coordinate transformations to orient the measured panels ($\mathbf{P}_{panel} = (\mathbf{X}_{panel}, \mathbf{Y}_{panel}, \mathbf{Z}_{panel})$) with the optical axis and paraboloidal equation, and extract the required rigid body motions for each panel for lowest RMS surface error.

1. Translate the entire map to locate P_{vertex} at the origin.

$$\begin{aligned} \mathbf{P}'_{panel} &= \mathbf{P}_{panel} - P_{vertex} \\ P'_{focus} &= P_{focus} - P_{vertex} \end{aligned} \quad (4)$$

2. Calculate Euler angles α and β of the line connecting the vertex and the focus.

$$\begin{aligned} \alpha &= \arctan\left(\frac{Z_{focus}}{X_{focus}}\right) \\ \beta &= \arctan\left(\frac{Z_{focus}}{Y_{focus}}\right) \end{aligned} \quad (5)$$

3. Calculate rotation matrix using Euler angles from the coordinates of the measured focal position

$$\mathbf{R} = \begin{bmatrix} \cos(\beta) & \sin(\alpha)\sin(\beta) & \cos(\alpha)\sin(\beta) \\ 0 & \cos(\alpha) & -\sin(\alpha) \\ -\sin(\beta) & \sin(\alpha)\cos(\beta) & \cos(\alpha)\cos(\beta) \end{bmatrix} \quad (6)$$

4. Apply rotation matrix to each panel point cloud and focus point

$$\begin{aligned} \mathbf{P}''_{panel} &= \mathbf{R}\mathbf{P}'_{panel} \\ P''_{focus} &= \mathbf{R}P'_{focus} \end{aligned} \quad (7)$$

5. Compare ideal paraboloid (radius R) to each panel

$$Z_{ideal}(X, Y) = r^2/(2R) = (X^2 + Y^2)/(2R) \quad (8)$$

$$\mathbf{Z}_{residual}(X, Y) = Z_{ideal}(\mathbf{X}''_{panel}, \mathbf{Y}''_{panel}) - \mathbf{Z}''_{panel} \quad (9)$$

6. Fit residual XYZ points of each panel to a plane

$$A\mathbf{X}''_{panel} + B\mathbf{Y}''_{panel} + C\mathbf{Z}_{residual} + D = 0 \quad (10)$$

7. Calculate piston, tip and tilt from plane-fit coefficients

$$\begin{aligned} \delta Z &= D \\ \theta &= \arctan(C/A) \\ \phi &= \arctan(C/B) \end{aligned} \quad (11)$$

The metrology process is set up to automatically deliver the required tip, tilt, and piston at the end of each measurement. Each panel has 4 actuators in each corner of the panel, separated by 400 mm, as shown in Figure 4. Eq 12 shows how to convert the tip, tilt and piston to actuator number of rotations using the angle approximation where δS is the spacing between actuators. Once of the number of mm of translation is determined, the threads per inch (TPI) of the actuators is used to convert to number of rotations.



Fig. 4 Coordinate system and actuator layout for each panel. Once tip, tilt, and piston values are extracted, they need to be converted to actual numbers of rotations on the actuators.

$$\begin{aligned} \mathbf{1} &: (0.5\theta\delta S + 0.5\phi\delta S + \delta Z) * TPI/25.4 \\ \mathbf{2} &: (-0.5\theta\delta S + 0.5\phi\delta S + \delta Z) * TPI/25.4 \\ \mathbf{3} &: (0.5\theta\delta S - 0.5\phi\delta S + \delta Z) * TPI/25.4 \\ \mathbf{4} &: (-0.5\theta\delta S - 0.5\phi\delta S + \delta Z) * TPI/25.4 \end{aligned} \quad (12)$$

4 Experimental Setup, Calibration, and Configuration

4.1 Hardware

The hardware for this system utilizes two FLIR Blackfly S USB 3 machine vision cameras with Sony IMX183 sensors (20MP 5472x3638, with $2.4 \mu\text{m}$ pixels), each with a Computar V0826-MPZ lens (8 mm focal length). Each camera is mounted to the ends of a 0.8 m length 8020 aluminum extrusion. The 8020 is mounted to a tripod for portability and pointing. With this setup, the entire 3.2 m dish can be seen from a 3-meter distance. We utilized an off-axis short-throw 1080P projector from BenQ (Model MW817ST), that can cover the entire surface from 1.5 meters away. The software to capture the images, process the fringe patterns, calculate the unwrapped phases, match the phase pairs, and triangulate the matched pairs to produce the 3D point clouds is written in MATLAB. Photos of the camera and projector hardware are shown in Figure 5.



Fig. 5 Left, one of the two FLIR Blackfly USB3 cameras with 8 mm focal length lens. Center, both cameras mounted to 8020 aluminum extrusion, mounted to a tripod. Right, BenQ 1080P short-throw projector used in this experiment.

4.2 Calibration

Calibration of the stereo camera pair was performed indoors for easier control of lighting and environmental conditions. A checkerboard calibration board made of aluminum and low-density polyethylene (LDPE) with size of 800 mm x 600 mm and square size of 30 mm was used. The calibration board was mounted to a tripod and traversed through the overlapping FOV at the 3-meter working distance for a set of 20 images. An example of one of these images is shown in Figure 6. Using the detected checkerboard corners on each sensor, each camera was calibrated individually for intrinsic parameters, then the pair was calibrated together for extrinsic parameters, keeping the intrinsic parameters fixed. The calibrated intrinsic and extrinsic parameters are shown in Table 1.

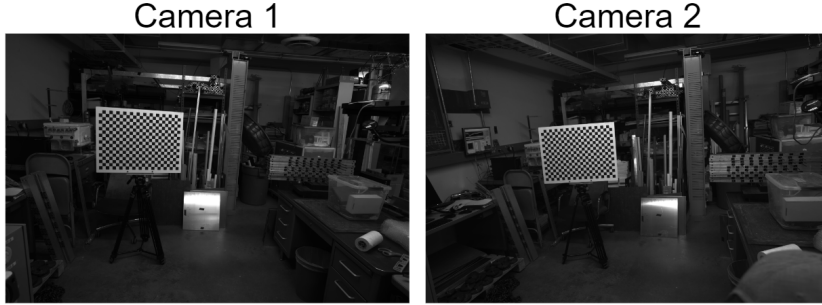


Fig. 6 An example image from the 20-image set used to calibrate the intrinsic and extrinsic parameters of the stereo camera pair. The checkerboard was moved throughout the overlapping FOV in order to properly calibrate for radial distortion.

Table 1 Calibrated stereo camera parameters.

Property	Camera 1	Camera 2
Focal Length (mm) f_x, f_y	8.25 mm, 8.25 mm	8.25 mm, 8.25 mm
Principle Point (pixels) u_x, u_y	2745, 1820	2750, 1843
Radial Distortion (r_2, r_4, r_6)	-.100, .126, -.043	-.096, .115, -.033
Extrinsic Matrix $\begin{bmatrix} \mathbf{R}_{3 \times 3} & \mathbf{t}_{3 \times 1} \\ \mathbf{0}_{1 \times 3} & 1 \end{bmatrix}$	$\begin{bmatrix} 0.926 & 0.061 & -0.373 & 801.048 \\ -0.072 & 0.997 & -0.014 & -40.332 \\ 0.371 & 0.039 & 0.928 & 170.496 \\ 0 & 0 & 0 & 1.0000 \end{bmatrix}$	

4.3 Measurement Setup

As described in Section 3.2, fiducials are placed at the paraboloid vertex and the telescope focal plane for defining the optical axis. These were roughly located using dimensions from the SRT CAD files. We used 1.0" white stickers placed in the middle of 1.5" black stickers as these fiducials for reliable contrast for circle detection with the Hough transform. Figure 7 shows the physical locations of the fiducials with respect to the rest of the telescope structure as well as the two adjacent panels to be aligned.

Measurements of the SRT are performed at night in order to increase the SNR of the projected patterns relative to ambient lighting. We also aimed for a night with low to no wind to reduce temporal errors associated with telescope structural bending or vibration. To avoid boosting noise in the images, the cameras were used with a gain of 0. To utilize the full dynamic range of the camera bit-depth, a 5-second exposure was used for each camera. As mentioned in Section 3.1, we employed 4 frequencies for the hierarchical phase unwrapping method, where we used the N-step phase shifting algorithm[39] for each frequency and each phase shifting direction (horizontal and vertical). This results in a 40-image pattern sequence (4 frequencies, 5 phase steps, 2 directions). Each pattern was captured 3 times and averaged to further eliminate noise, resulting in a 600-second (10-minute) acquisition time. Figure 8 shows an actual data acquisition in progress at night.

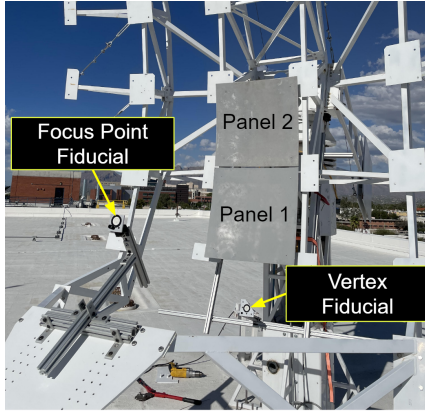


Fig. 7 Layout of the telescope structure. Two fiducials are placed where the paraboloid vertex and focus should be using 8020 extrusions. An example panel 1 and panel 2 are installed on the telescope. They are the bottom two rows of the center column of panels.

Once a measurement is made, the rigid body motions for each panel are extracted using the process described in Section 3.2, and each panel is adjusted using 4 manual actuators located in the corners of each panel. The actuators have 1 mm thread pitch and are separated by 400 mm. Thus to tilt a panel by 1 degree (17.45 mrad), opposite actuators must move $\approx 400mm * 0.01745rad = 7mm \implies \pm 3.5$ mm. After an iteration of adjusting tip, tilt, and piston is performed, the panels are then remeasured and the adjustment process is repeated until the remaining errors are satisfactory.

5 Results

Figure 9 shows an example set of horizontal and vertical phases from the perspectives of camera 1 and camera 2. Each pixel on each panel in camera 1 has a unique combination of horizontal and vertical phase. The camera 2 phases are searched for a matching phase pair for each pixel on camera 1. The resulting matched locations on each camera detector are triangulated using the calibrated parameters from Table 1. Figure 10 demonstrates the data produced by the system described in this paper. Figure 10a shows the data returned from the software in its raw format, with the locations of the cameras, paraboloid vertex, focus, and point clouds of both panels. Using steps 1-4 from 3.2 yields Figure 10b to align the optical axis of the telescope with the z-axis. Steps 5-6 are done for each panel to produce the piston, tip, and tilt error for each panel. Figure 11 shows the best fit plane to panels 1 and 2 before adjustments begin and Table 2 shows the actual starting piston, tip and tilt values.

Besides the rigid body errors, each panel has imperfections compared to the ideal shape. Figure 12 shows the residual from the ideal paraboloid for each panel with tip, tilt, and piston errors removed. Panel 1 has a 1.28 mm RMS, and Panel 2 has a 0.81 mm RMS. These are not actual panels that will be used in the telescope, but are examples used for this initial alignment test. For this experiment, the panel actuators on SRT are not capable of shape correction; however, the system delivers information

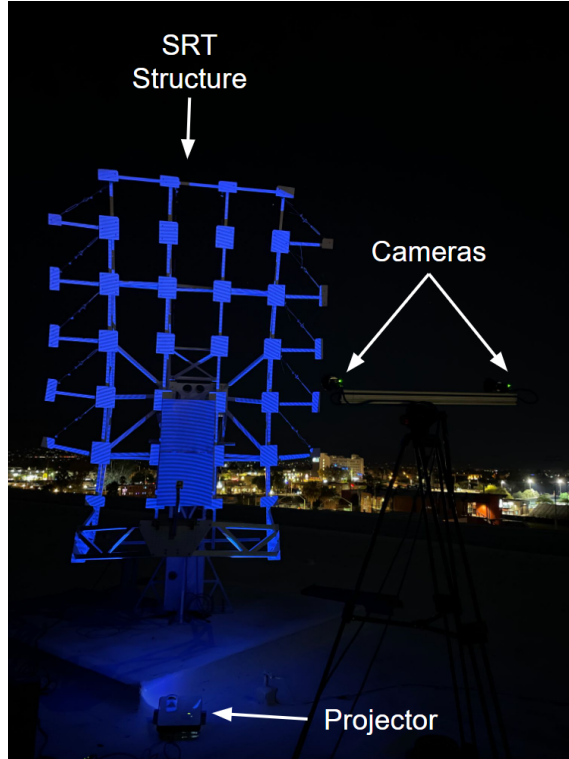


Fig. 8 Nighttime measurement setup. The projector is placed near the telescope and utilizes the short-throw to cover the entire dish. The tripod carrying both cameras is placed roughly 3 meters away from the dish and positioned such that the entire dish can be seen in the field of view of both cameras. Shown in the image is the 10-pixel period frequency projected onto the dish structure.

Table 2 Results before the first adjustment iteration.

Property	Panel 1	Panel 2
δZ	-0.70 mm	10.46 mm
θ	0.757 deg	0.80 deg
ϕ	-0.54 deg	-3.15 deg

that could be used to do so on most other large radio telescopes. The goal of the adjustment process is to make the dish surface accuracy limited by the individual panel accuracy, not the rigid body errors.

We performed 4 measurements with 3 adjustment iterations. Within 3 iterations, piston error was reduced to < 0.25 mm and tip/tilt was reduced to < 0.1 degrees. The final panel RMS including alignment errors was 1.325 mm and 0.842 mm for panel 1 and panel 2, respectively. Collectively, the two panels make a small dish with 1.12 mm

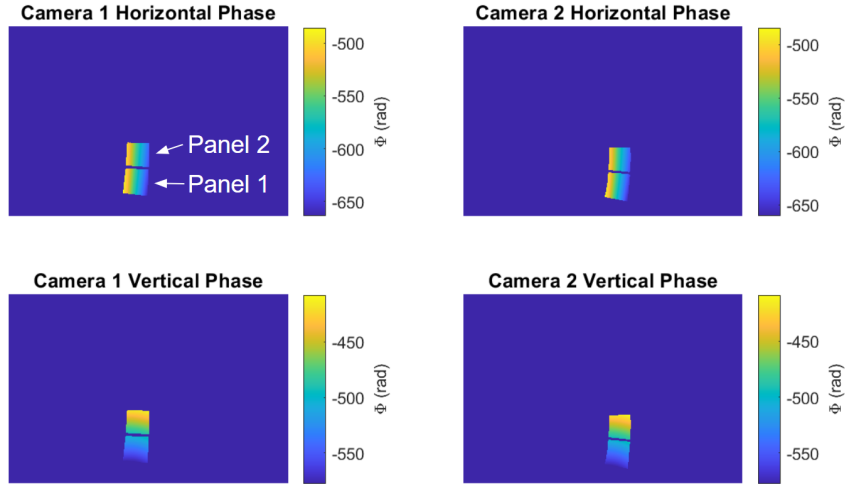


Fig. 9 Images from each camera are masked to isolate the two panels being measured. The phase unwrapping process produces four images: horizontal and vertical phase for each camera. These maps are used to find matching object locations from pixels on camera 1 to locations on camera 2.

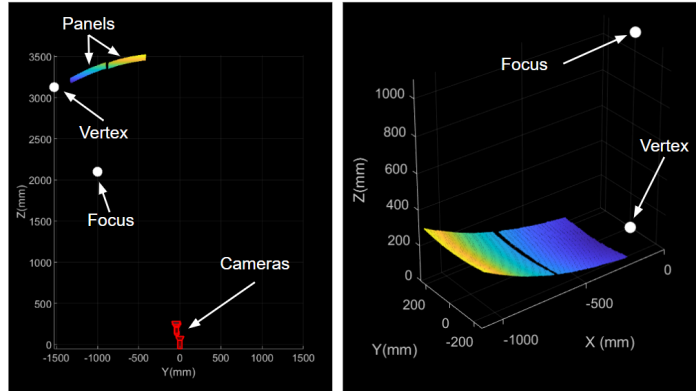


Fig. 10 Each FPP measurement results in a point cloud for each panel, and the relative location of both the vertex and the focus. Raw data is shown on the left. The triangulated 3D points are produced relative to the coordinate system defined by camera 1. Matrix rotations and translations are applied to the panel point clouds to align the optical axis with the z-axis, shown on the right. In this configuration, the panels can be directly compared to Eq. 9 to extract the residual error in the panels, as well as the rigid body alignment error.

RMS error. Looking back at the plot of the Ruze equation in Figure 1, this error would make the dish capable of observing 2 cm wavelengths (15 GHz) with less than 50% loss. Most of the error in this test is attributed to panel shape, which the actuators for this telescope are not configured to correct. Figure 13 shows how the piston and tilt errors converged through each iteration.

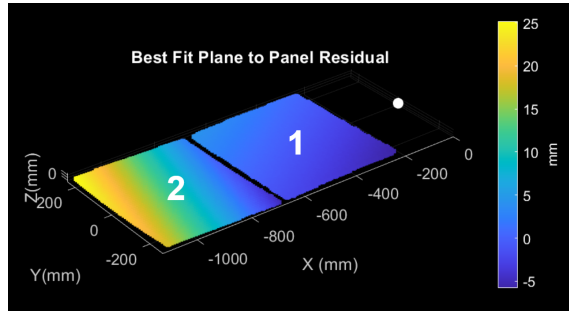


Fig. 11 Best fit planes for each panel, including piston.

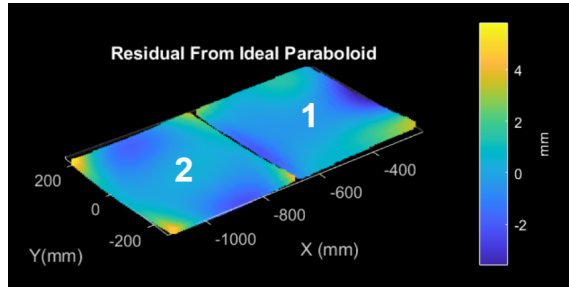


Fig. 12 In addition to finding the rigid body motion error of each panel, the system also has enough resolution to map the surface errors of each panel compared to their ideal shape. Shown here are the residual surface maps compared to the ideal paraboloid.

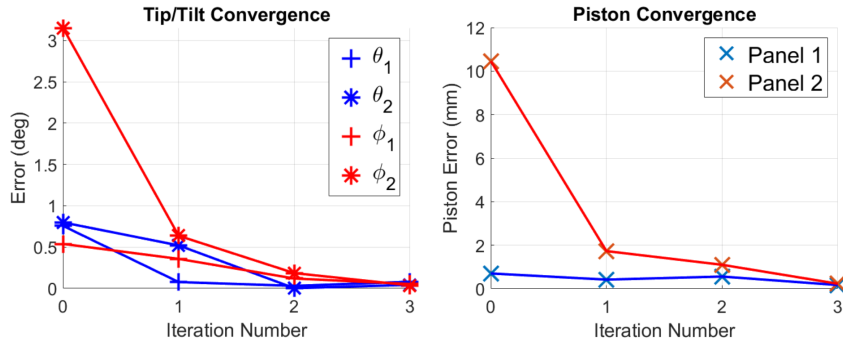


Fig. 13 Four measurements were performed, with three adjustment iterations between each measurement. Left, is the tip and tilt of each panel improving across each iteration. Right shows the piston for each panel also improving. Panel 1 was fortunately close to the ideal piston position before an adjustment was performed.

Table 3 Final results after 3 adjustments.

Property	Panel 1	Panel 2
δZ	-0.17 mm	0.23 mm
θ	0.081 deg	-0.044 deg
ϕ	-0.054 deg	-0.037 deg

6 Discussions and Future Work

This method provides several advantages compared to other antenna metrology methods. The major improvement results from its non-contact nature. This has a two-fold benefit: speed and logistics. The setup time is less than 10 minutes, and the measurement takes only 10 minutes. This could be reduced even further by implementing a brighter projector and decreasing the required exposure time. Due to the rapid setup time, the system could be moved from telescope to telescope for the purpose of aligning arrays with large numbers of dishes. This avoids the need to coordinate with satellites and the use of cryogenic detectors required by the holography method. This method also eliminates much of the manual labor required by photogrammetry and laser trackers, which require manual placement of stickers or retroreflectors. These methods are time consuming, labor intensive, and create safety risks for those that need to climb the dishes and place the fiducials. This method could also be installed on the telescope structure as a permanent metrology system for telescopes that have active surfaces or require regular maintenance[20]. This would also allow surface measurements to be performed at a variety of elevation angles to properly characterize gravity deformations.

Additionally, this method could be scalable to extremely large radio telescope apertures like the ngVLA 18-meter dish. Sensor size, lens focal length, and the number of cameras can be adjusted to achieve the required spatial resolution and field of view to cover the aperture of a large dish. There are some practical challenges to overcome to achieve this related to camera calibration and projector brightness. Some development is needed to calibrate a large number of cameras over a large area, with a long working distance. Methods utilizing auxiliary sensors to calibrate cameras with large baselines could be used [18, 33], but likely need some future development to adapt for more cameras. In addition, developing or sourcing a projector with enough brightness to cover this large area could be challenging, however commercial cinema projectors may be ideal. The authors hope that this method may contribute to the development of non-contact metrology technologies needed to quickly, safely, and reliably commission future large telescopes.

References

- [1] Angeli GZ, Bernstein R, Walls B, et al (2018) Systems engineering for the giant magellan telescope. In: Modeling, Systems Engineering, and Project Management for Astronomy VIII, SPIE, pp 203–216

- [2] Atherton TJ, Kerbyson DJ (1999) Size invariant circle detection. *Image and Vision computing* 17(11):795–803
- [3] Attoli A, Poppi S, Buffa F, et al (2023) The sardinia radio telescope metrology system. In: 2023 XXXVth General Assembly and Scientific Symposium of the International Union of Radio Science (URSI GASS), IEEE, pp 1–4
- [4] Baars J, Martin R (1996) The heinrich hertz telescope-a new instrument for submillimeter-wavelength astronomy. *Reviews in Modern Astronomy*, v 9,(1996), p 111-126 9:111–126
- [5] Baars JW, Kärcher HJ (2018) *Radio Telescope Reflectors*, vol 447. Springer
- [6] van Belle GT, Meinel AB, Meinel MP (2004) The scaling relationship between telescope cost and aperture size for very large telescopes. In: *Ground-based telescopes*, Spie, pp 563–570
- [7] Berkson J, Hyatt J, Kang H, et al (2023) Binocular fringe projection profilometry for the metrology of meter-scale optical surfaces. *Optics Continuum* 2(4):697–711
- [8] Cuevas LC, Alvarez ML, Leon-Huerta A, et al (2013) Iterative alignment of reflector segments using a laser tracker. In: *Optical Measurement Systems for Industrial Inspection VIII*, SPIE, pp 819–831
- [9] Edmundson K, Baker L (2001) Photogrammetric measurement of the arecibo primary reflector surface. *Coordinate Measurement Systems Committee Conference*
- [10] Ellis W, Kim D, Hyatt J, et al (2023) Radio telescope manufacturing with adaptive aluminum thermoforming and fringe projection metrology. In: *Astronomical Optics: Design, Manufacture, and Test of Space and Ground Systems IV*, SPIE, pp 195–198
- [11] Hartley R, Zisserman A (2003) *Multiple view geometry in computer vision*. Cambridge university press
- [12] Ingalls RP, Antebi J, Ball JA, et al (1994) Upgrading the haystack radio telescope for operation at 115 ghz. *Proceedings of the IEEE* 82(5):742–755
- [13] Jewell PR (2000) The green bank telescope. *Radio Telescopes* 4015:136–147
- [14] Kim EH, Hahn J, Kim H, et al (2009) Profilometry without phase unwrapping using multi-frequency and four-step phase-shift sinusoidal fringe projection. *Optics Express* 17(10):7818–7830
- [15] Leon-Huerta A, Alvarez ML, Rios EH, et al (2014) Experiences with global laser tracker alignment of the 32.5-m lmt primary surface. In: *Advances in Optical and Mechanical Technologies for Telescopes and Instrumentation*, SPIE, pp 1244–1256

- [16] Li R, Qin X, Konyakhin I, et al (2020) Cmos multi-matrix optoelectronic system for high speed measurement of main mirror deformation large diameter radio telescope. *IEEE Access* 8:51821–51829
- [17] Meinel AB (1979) Cost Scaling Laws Applicable To Very Large Optical Telescopes. In: Crawford DL (ed) *Instrumentation in Astronomy III*, International Society for Optics and Photonics, vol 0172. SPIE, pp 2 – 7, <https://doi.org/10.1117/12.957059>
- [18] Miyata S, Saito H, Takahashi K, et al (2017) Extrinsic camera calibration without visible corresponding points using omnidirectional cameras. *IEEE Transactions on Circuits and Systems for Video Technology* 28(9):2210–2219
- [19] Olmi L (1998) Large millimeter telescope project: overview and optical design. *Advanced Technology MMW, Radio, and Terahertz Telescopes* 3357:186–197
- [20] Parker DH, Payne JM (2002) Active surface architectures of large radio telescopes. *Proceedings of the XXVIIth URSI General Assembly in Maastricht*
- [21] Rogers AE, Barvainis R, Charpentier P, et al (1993) Corrections for the effects of a radome on antenna surface measurements made by microwave holography. *IEEE transactions on antennas and propagation* 41(1):77–84
- [22] Ruze J (1966) Antenna tolerance theory—a review. *Proceedings of the IEEE* 54(4):633–640
- [23] Schloerb FP, Souccar K, Gale DM, et al (2022) Lasers: a real time antenna metrology system for the large millimeter telescope. In: *Advances in Optical and Mechanical Technologies for Telescopes and Instrumentation V*, SPIE, pp 477–488
- [24] Selina RJ, Murphy EJ, McKinnon M, et al (2018) The next-generation very large array: A technical overview. *Ground-based and Airborne Telescopes VII* 10700:497–513
- [25] Serra G, Bolli P, Busonera G, et al (2012) The microwave holography system for the sardinia radio telescope. In: *Ground-based and Airborne Telescopes IV*, SPIE, pp 1877–1891
- [26] Shankar NU, Duraichelvan R, Ateequlla C, et al (2009) Photogrammetric measurements of a 12-metre preloaded parabolic dish antenna. *arXiv preprint arXiv:09051252*
- [27] Su X, Chen W (2004) Reliability-guided phase unwrapping algorithm: a review. *Optics and Lasers in Engineering* 42(3):245–261
- [28] Sullivan IS, Morales MF, Hazelton BJ, et al (2012) Fast holographic deconvolution: A new technique for precision radio interferometry. *The Astrophysical*

- [29] Süß M, Koch D, Paluszek H (2012) The sardinia radio telescope (srt) optical alignment. In: *Ground-based and Airborne Telescopes IV*, SPIE, pp 843–858
- [30] Theron IP, Lehmensiek R, de Villiers DI (2012) The design of the meerkat dish optics. In: *2012 International Conference on Electromagnetics in Advanced Applications*, IEEE, pp 539–542
- [31] de Villiers DI, Lehmensiek R (2023) Performance estimates of the 18-meter ngvla reflector system with main reflector rim extension. In: *2023 IEEE International Symposium on Antennas and Propagation and USNC-URSI Radio Science Meeting (USNC-URSI)*, IEEE, pp 763–764
- [32] de Villiers MS (2023) MeerKat holography measurements in the uhf, l, and s bands. *The Astronomical Journal* 165(3):78
- [33] Wang J, Guan B, Han Y, et al (2023) Sensor-aided calibration of relative extrinsic parameters for outdoor stereo vision systems. *Remote Sensing* 15(5):1300
- [34] Wang M, Li D, Zhao Y (2020) Iterative alignment of reflector panels for large-scale compact test range in non-metrology environment based on laser tracker. *Measurement Science and Technology* 31(4):045002
- [35] Yuen H, Princen J, Illingworth J, et al (1990) Comparative study of hough transform methods for circle finding. *Image and vision computing* 8(1):71–77
- [36] Zarghamee MS, Antebi J, Kan FW (1995) Optimal surface adjustment of haystack antenna. *IEEE transactions on antennas and propagation* 43(1):79–86
- [37] Zhang Z (2000) A flexible new technique for camera calibration. *IEEE Transactions on pattern analysis and machine intelligence* 22(11):1330–1334
- [38] Zuo C, Huang L, Zhang M, et al (2016) Temporal phase unwrapping algorithms for fringe projection profilometry: A comparative review. *Optics and lasers in engineering* 85:84–103
- [39] Zuo C, Feng S, Huang L, et al (2018) Phase shifting algorithms for fringe projection profilometry: A review. *Optics and Lasers in Engineering* 109:23–59

REFERENCES

- [1] Neta A Bahcall and Raymond M Soneira. The spatial correlation function of rich clusters of galaxies. *Astrophysical Journal, Part 1 (ISSN 0004-637X)*, vol. 270, July 1, 1983, p. 20-38., 270:20–38, 1983.
- [2] Robert Julius Trumpler and Harold F Weaver. *Statistical astronomy*. Univ of California Press, 1953.
- [3] Miguel Arevallilo Herráez, David R Burton, Michael J Lalor, and Munther A Gdeisat. Fast two-dimensional phase-unwrapping algorithm based on sorting by reliability following a noncontinuous path. *Applied Optics*, 41(35):7437–7444, 2002.
- [4] Aden B. Meinel. Cost Scaling Laws Applicable To Very Large Optical Telescopes. In David L. Crawford, editor, *Instrumentation in Astronomy III*, volume 0172, pages 2 – 7. International Society for Optics and Photonics, SPIE, 1979. doi: 10.1117/12.957059.
- [5] Gerard Theodore van Belle, Aden Baker Meinel, and Marjorie Pettit Meinel. The scaling relationship between telescope cost and aperture size for very large telescopes. In *Ground-based telescopes*, volume 5489, pages 563–570. Spie, 2004.
- [6] Shep Doeleman, EHT Collaboration, et al. Focus on the first event horizon telescope results. *Astrophys J Lett. April*, 2019.
- [7] John Ruze. Antenna tolerance theory—a review. *Proceedings of the IEEE*, 54(4):633–640, 1966.
- [8] Jacob WM Baars and Hans J Kärcher. *Radio Telescope Reflectors*, volume 447. Springer, 2018.
- [9] Roger P Angel, Thomas E Stalcup, et al. Glass or metal forming mold of adjustable shape, January 21 2020. US Patent 10,538,451.
- [10] Yong Liu, Zhoujie Zhu, Zijian Wang, Bin Zhu, Yilin Wang, and Yisheng Zhang. Flow and friction behaviors of 6061 aluminum alloy at elevated temperatures and hot stamping of a b-pillar. *The International Journal of Advanced Manufacturing Technology*, 96:4063–4083, 2018.

- [11] N Udaya Shankar, R Duraichelvan, CM Ateequlla, Arvind Nayak, A Krishnan, MKS Yogi, C Koteswar Rao, K Vidyasagar, Rohit Jain, Pravesh Mathur, et al. Photogrammetric measurements of a 12-metre preloaded parabolic dish antenna. *arXiv preprint arXiv:0905.1252*, 2009.
- [12] Kenneth Edmundson and Lynn Baker. Photogrammetric measurement of the arecibo primary reflector surface. *Coordinate Measurement Systems Committee Conference*, 2001.
- [13] Martin Süß, Dietmar Koch, and Heiko Paluszek. The sardinia radio telescope (srt) optical alignment. In *Ground-based and Airborne Telescopes IV*, volume 8444, pages 843–858. SPIE, 2012.
- [14] Renpu Li, Xiaojuan Qin, Igor Konyakhin, Minh Hoa Tong, Alexander Usik, Yongle Lu, Ke Di, and Yu Liu. Cmos multi-matrix optoelectronic system for high speed measurement of main mirror deformation large diameter radio telescope. *IEEE Access*, 8:51821–51829, 2020.
- [15] Ian S Sullivan, Miguel F Morales, Bryna J Hazelton, Wayne Arcus, David Barnes, Gianni Bernardi, Frank H Briggs, Judd D Bowman, John D Bunton, Roger J Cappallo, et al. Fast holographic deconvolution: A new technique for precision radio interferometry. *The Astrophysical Journal*, 759(1):17, 2012.
- [16] Richard P Ingalls, JOSEPH Antebi, John A Ball, Richard Barvainis, John F Cannon, Joseph C Carter, PAUL J Charpentier, Brian E Corey, Joseph W Crowley, KEVIN A Dudevoir, et al. Upgrading the haystack radio telescope for operation at 115 ghz. *Proceedings of the IEEE*, 82(5):742–755, 1994.
- [17] G Serra, P Bolli, G Busonera, T Pisanu, S Poppi, F Gaudiomonte, G Zacchi-rolì, J Roda, M Morsiani, and JA Lopez-Perez. The microwave holography system for the sardinia radio telescope. In *Ground-based and Airborne Telescopes IV*, volume 8444, pages 1877–1891. SPIE, 2012.
- [18] JWM Baars and RN Martin. The heinrich hertz telescope-a new instrument for submillimeter-wavelength astronomy. *Reviews in Modern Astronomy, v. 9,(1996)*, p. 111-126., 9:111–126, 1996.
- [19] Andrea Leon-Huerta, Maribel Lucero Alvarez, Emilio Hernández Rios, Lizeth Cabrera Cuevas, David Castro Santos, Carlos Tzile Torres, Josefina Lázaro Hernández, David M Gale, Gopal Narayanan, David R Smith, et al. Experiences with global laser tracker alignment of the 32.5-m lmt primary surface. In *Advances in Optical and Mechanical Technologies for Telescopes and Instrumentation*, volume 9151, pages 1244–1256. SPIE, 2014.

- [20] Mingming Wang, Dongsheng Li, and Youlei Zhao. Iterative alignment of reflector panels for large-scale compact test range in non-metrology environment based on laser tracker. *Measurement Science and Technology*, 31(4):045002, 2020.
- [21] Lizeth Cabrera Cuevas, Maribel Lucero Alvarez, Andrea Leon-Huerta, Emilio Hernandez Rios, Josefina Hernandez Lázaro, Carlos Tzile Torres, David Castro Santos, David M Gale, Grant Wilson, Gopal Narayanan, et al. Iterative alignment of reflector segments using a laser tracker. In *Optical Measurement Systems for Industrial Inspection VIII*, volume 8788, pages 819–831. SPIE, 2013.
- [22] Alessandro Attoli, Sergio Poppi, Franco Buffa, Giampaolo Serra, Antonietta Fara, Pasqualino Marongiu, Giannina Sanna, Francesco Gaudiomonte, Mauro Pili, Tonino Pisanu, et al. The sardinia radio telescope metrology system. In *2023 XXXVth General Assembly and Scientific Symposium of the International Union of Radio Science (URSI GASS)*, pages 1–4. IEEE, 2023.
- [23] Mattieu S de Villiers. Meerkat holography measurements in the uhf, l, and s bands. *The Astronomical Journal*, 165(3):78, 2023.
- [24] F Peter Schloerb, Kamal Souccar, David M Gale, Andrea León Huerta, David H Hughes, and Grant W Wilson. Lasers: a real time antenna metrology system for the large millimeter telescope. In *Advances in Optical and Mechanical Technologies for Telescopes and Instrumentation V*, volume 12188, pages 477–488. SPIE, 2022.
- [25] JRP Angel, MT Adams, TA Boroson, and RL Moore. A very large optical telescope array linked with fused silica fibers. *The Astrophysical Journal*, 218: 776–782, 1977.
- [26] Aleksander Wolszczan and Dail A Frail. A planetary system around the millisecond pulsar psr1257+ 12. *Nature*, 355(6356):145–147, 1992.
- [27] D Charbonneau. Sizing up close-in planets around sun-like stars. In *American Astronomical Society Meeting Abstracts*, volume 197, pages 62–04, 2000.
- [28] Timothy M Brown. Transmission spectra as diagnostics of extrasolar giant planet atmospheres. *The Astrophysical Journal*, 553(2):1006, 2001.
- [29] Kevin K Hardegree-Ullman, Dániel Apai, Galen J Bergsten, Ilaria Pascucci, and Mercedes López-Morales. Bioverse: A Comprehensive Assessment of the Capabilities of Extremely Large Telescopes to Probe Earth-like O₂ Levels in Nearby Transiting Habitable-zone Exoplanets. *The Astronomical Journal*, 165 (6):267, 2023. Publisher: IOP Publishing.

- [30] Roger Angel, Chad Bender, Joel Berkson, Nick Didato, John Ford, Peter Gray, Buell Jannuzi, Dean Ketelsen, Daewook Kim, Gilberto Chavez Lopez, and others. LFAST, the Large Fiber Array Spectroscopic Telescope. In *Ground-based and Airborne Telescopes IX*, volume 12182, pages 631–643. SPIE, 2022.
- [31] Matt Johns. The giant magellan telescope (GMT). In *Ground-based and Airborne Telescopes*, volume 6267, pages 762–776. SPIE, 2006.
- [32] Jerry Nelson and Gary H Sanders. The status of the Thirty Meter Telescope project. In *Ground-based and Airborne Telescopes II*, volume 7012, pages 504–521. SPIE, 2008.
- [33] Roberto Gilmozzi and Jason Spyromilio. The 42m european elt: status. In *Ground-based and Airborne Telescopes II*, volume 7012, pages 494–503. SPIE, 2008.
- [34] Robert K Jungquist. Optical design of the Hobby-Eberly Telescope four-mirror spherical aberration corrector. In *Current Developments in Optical Design and Optical Engineering VIII*, volume 3779, pages 2–16. SPIE, 1999.
- [35] Michael J Kidger. Fundamental optical design. SPIE-International Society for Optical Engineering, 2001.
- [36] DD Maksutov. New catadioptric meniscus systems. *JOSA*, 34(5):270–284, 1944. Publisher: Optica Publishing Group.
- [37] Damien J Jones and William E James. Prime focus correctors for the spherical mirror. *Applied optics*, 31(22):4384–4388, 1992. Publisher: Optica Publishing Group.
- [38] Damien J Jones. Wide-field prime focus corrector for the Anglo-Australian telescope. *Applied optics*, 33(31):7362–7366, 1994. Publisher: Optica Publishing Group.
- [39] Alexander V. Goncharov, Nicholas Devaney, and Christopher Dainty. Atmospheric dispersion compensation for extremely large telescopes. *Opt. Express*, 15(4):1534–1542, February 2007. doi: 10.1364/OE.15.001534. URL <https://opg.optica.org/oe/abstract.cfm?URI=oe-15-4-1534>. Publisher: Optica Publishing Group.
- [40] Andrew Rakich. A New Type of Atmospheric Dispersion Corrector Suitable for Wide-Field High-Resolution Imaging and Spectroscopy on Large Telescopes. *Applied Sciences*, 11(14):6261, 2021. Publisher: MDPI.

- [41] Gerardo Avila, Gero Rupprecht, and Jacques Maurice Beckers. Atmospheric dispersion correction for the FORS Focal Reducers at the ESO VLT. In *Optical Telescopes of Today and Tomorrow*, volume 2871, pages 1135–1143. SPIE, 1997.
- [42] Will Saunders, Peter Gillingham, Greg Smith, Steve Kent, and Peter Doel. Prime focus wide-field corrector designs with lossless atmospheric dispersion correction. In *Advances in Optical and Mechanical Technologies for Telescopes and Instrumentation*, volume 9151, pages 519–528. SPIE, 2014.
- [43] Will Saunders and Peter R Gillingham. Optical designs for the Maunakea Spectroscopic Explorer telescope. In *Ground-based and Airborne Telescopes VI*, volume 9906, pages 1157–1168. SPIE, 2016.
- [44] C Hohenkerk and A Sinclair. Nao technical note 63. *HM Nautical Almanac Office*, 1985.
- [45] P Kenneth Seidelmann. *Explanatory supplement to the astronomical almanac*. University Science Books, 1992.
- [46] Katie Schwertz and James H. Burge. *Field guide to optomechanical design and analysis*. SPIE Press, 2012.
- [47] Edmund Optics. Precision Tolerances for Spherical Lenses, 2023. URL <https://www.edmundoptics.com/knowledge-center/application-notes/optics/precision-tolerances-for-spherical-lenses/>.
- [48] Inc Optimax Systems. Manufacturing Tolerance Chart, 2023. URL <https://www.optimaxsi.com/charts/manufacturing-tolerance-chart/>.
- [49] LaCroix Precision Optics. Optical Manufacturing Tolerance Chart, 2023. URL <https://lacroixoptics.com/capabilities/optical-manufacturing-tolerance-chart>.
- [50] Frédéric Lamontagne. Optomechanical Tolerancing and Error Budgets. *Handbook of Optomechanical Engineering*, pages 207–268, 2017. Publisher: CRC Press.
- [51] James E Harvey. The surface PSD and image degradation due to mid-spatial-frequency errors. In *Tribute to James C. Wyant: The Extraordinaire in Optical Metrology and Optics Education*, volume 11813, pages 160–173. SPIE, 2021.
- [52] Chris J Evans. PVr—a robust amplitude parameter for optical surface specification. *Optical Engineering*, 48(4):043605–043605, 2009. Publisher: Society of Photo-Optical Instrumentation Engineers.

- [53] Buddy Martin, John M Hill, and Roger Angel. The New Ground-Based Optical Telescopes. *Physics Today*, 44(3):22–30, 1991. Publisher: American Institute of Physics.
- [54] HM Martin, JH Burge, B Cuerden, WB Davison, JS Kingsley, WC Kittrell, RD Lutz, SM Miller, C Zhao, and T Zobrist. Progress in manufacturing the first 8.4 m off-axis segment for the Giant Magellan Telescope. In *Advanced Optical and Mechanical Technologies in Telescopes and Instrumentation*, volume 7018, pages 103–114. SPIE, 2008.
- [55] HM Martin, RG Allen, JH Burge, DW Kim, JS Kingsley, MT Tuell, SC West, C Zhao, and T Zobrist. Fabrication and testing of the first 8.4-m off-axis segment for the Giant Magellan Telescope. In *Modern Technologies in Space-and Ground-based Telescopes and Instrumentation*, volume 7739, pages 84–96. SPIE, 2010.
- [56] HM Martin, RG Allen, JH Burge, DW Kim, JS Kingsley, K Law, RD Lutz, PA Strittmatter, P Su, MT Tuell, and others. Production of 8.4 m segments for the Giant Magellan Telescope. In *Modern Technologies in Space-and Ground-based Telescopes and Instrumentation II*, volume 8450, pages 801–815. SPIE, 2012.
- [57] Changhui Rao, Wenhan Jiang, and Ning Ling. Spatial and temporal characterization of phase fluctuations in non-Kolmogorov atmospheric turbulence. *Journal of Modern Optics*, 47(6):1111–1126, 2000. Publisher: Taylor & Francis.
- [58] A Consortini and L Ronchi. Choice of the model of atmospheric turbulence. *Applied Optics*, 11(5):1205–1211, 1972. Publisher: Optica Publishing Group.
- [59] Andrew J Young, Roger Angel, Chad Bender, Joel Berkson, Peter Gray, Samuel Halverson, Hyukmo Kang, Daewook Kim, Andy Monson, Chang-Jin Oh, et al. The large fiber array spectroscopic telescope: opto-mechanical design and architecture. In *Ground-based and Airborne Telescopes IX*, volume 12182, pages 1339–1351. SPIE, 2022.
- [60] Jessica DeGroote Nelson, Michael P. Mandina, and Richard Plympton. If you can't measure it, you can't make it: the importance of metrology in optics fabrication Optimax's 30 year history. In Virendra N. Mahajan and Daewook Kim, editors, *Tribute to James C. Wyant: The Extraordinaire in Optical Metrology and Optics Education*, volume 11813, page 118130H. International Society for Optics and Photonics, SPIE, 2021. doi: 10.1117/12.2571252. URL <https://doi.org/10.1117/12.2571252>.

- [61] Jingquan Cheng. *The principles of astronomical telescope design*, volume 360. Springer New York, 2009.
- [62] Christian Davila-Peralta, Justin Hyatt, Zack Hatfield, Alex St Peter, Bailey S Allen, Naomi Nguyen, Wyatt Ellis, Dae Wook Kim, Joel Berkson, and Emili Rodriguez. Electromagnetic thermoforming to manufacture reflective panels for radio telescopes and downlinks. In *2021 IEEE Aerospace Conference (50100)*, pages 1–15. IEEE, 2021.
- [63] G Valsecchi, J Eden, G Grisoni, CGM van’t Klooster, and L Fanchi. High precision electroformed nickel panel technology for sub-millimeter radio telescope antennas. In *IEEE Antennas and Propagation Society International Symposium. Digest. Held in conjunction with: USNC/CNC/URSI North American Radio Sci. Meeting (Cat. No. 03CH37450)*, volume 1, pages 124–127. IEEE, 2003.
- [64] Per-Simon Kildal. Some reflector and feed antenna inventions that made a difference: Fundamentals and examples from radio telescopes, satellite communications and radio links. *2013 Africon*, pages 1–3, 2013.
- [65] David M Gale, Maribel Lucero Álvarez, Lizeth Cabrera Cuevas, Andrea Leon-Huerta, Edgar Arizmendi Reyes, Octavio Icasio Hernández, David Castro Santos, Emilio Hernández Ríos, Esteban Tecuapetla Sosa, Carlos Tzile Torres, and Miguel Viliesid Alonso. Coordinate metrology of a primary surface composite panel from the large millimeter telescope. In *Advances in Optical and Mechanical Technologies for Telescopes and Instrumentation II*, volume 9912, page 991211. International Society for Optics and Photonics, 2016.
- [66] Yong Zhang, Dehua Yang, Yeping Li, Guohua Zhou, Aihua Li, Guoping Li, and Zhenchao Zhang. A new efficient laser angle metrology system for maintaining the large radio telescope active reflecting antenna. In *Ground-based and Airborne Telescopes III*, volume 7733, pages 1261–1268. SPIE, 2010.
- [67] William T Estler, KL Edmundson, GN Peggs, and DH Parker. Large-scale metrology—an update. *CIRP annals*, 51(2):587–609, 2002.
- [68] Rogerio Enriquez and Cesar E Sampieri. Surface metrology using laser trackers. In *Eighth International Symposium on Laser Metrology*, volume 5776, pages 568–575. SPIE, 2005.
- [69] Toni Schenk. Introduction to photogrammetry. *The Ohio State University, Columbus*, 106, 2005.

- [70] Ravi Subrahmanyam. Photogrammetric measurement of the gravity deformation in a cassegrain antenna. *IEEE Transactions on Antennas and Propagation*, 53(8):2590–2596, 2005.
- [71] Markus Rumpler, Shreyansh Daftry, Alexander Tscharf, Rudolf Pretenthaler, Christof Hoppe, Gerhard Mayer, and Horst Bischof. Automated end-to-end workflow for precise and geo-accurate reconstructions using fiducial markers. *ISPRS Annals of Photogrammetry, Remote Sensing and Spatial Information Sciences*, 3:135–142, 2014.
- [72] Joel Berkson, Zack Hatfield, Alex St Peter, Henry Quach, Emily Rodriguez, Naomi Nguyen, Wyatt Ellis, Kevin Derby, Christian Davila-Peralta, Justin Hyatt, et al. Meter-class infrared deflectometry for visibly non-specular surface metrology. In *Optical Fabrication and Testing*, pages JTU2B–3. Optica Publishing Group, 2021.
- [73] Song Zhang. High-speed 3d shape measurement with structured light methods: A review. *Optics and Lasers in Engineering*, 106:119–131, 2018.
- [74] Sam Van der Jeught and Joris JJ Dirckx. Real-time structured light profilometry: a review. *Optics and Lasers in Engineering*, 87:18–31, 2016.
- [75] Song Zhang. *Handbook of 3D machine vision: Optical metrology and imaging*. CRC press, 2013.
- [76] Sai Siva Gorthi and Pramod Rastogi. Fringe projection techniques: whither we are? *Optics and lasers in engineering*, 48(ARTICLE):133–140, 2010.
- [77] Yin Yongkai, Zhang Zonghua, Liu Xiaoli, and Peng Xiang. Review of the system model and calibration for fringe projection profilometry. *Infrared and Laser Engineering*, 49(3):0303008, 2020.
- [78] Shijie Feng, Chao Zuo, Liang Zhang, Tianyang Tao, Yan Hu, Wei Yin, Jiaming Qian, and Qian Chen. Calibration of fringe projection profilometry: A comparative review. *Optics and Lasers in Engineering*, 143:106622, 2021.
- [79] Yan Hu, Qian Chen, Shijie Feng, and Chao Zuo. Microscopic fringe projection profilometry: A review. *Optics and lasers in engineering*, 135:106192, 2020.
- [80] Zhenkun Lei, Chunli Wang, and Canlin Zhou. Multi-frequency inverse-phase fringe projection profilometry for nonlinear phase error compensation. *Optics and Lasers in Engineering*, 66:249–257, 2015.
- [81] Jonathan Mark Huntley and CR Coggrave. Optimization of a shape measurement system based on spatial light modulators. In *Laser Metrology and Inspection*, volume 3823, pages 104–114. SPIE, 1999.

- [82] Song Zhang and Peisen S Huang. Phase error compensation for a 3-d shape measurement system based on the phase-shifting method. *Optical Engineering*, 46(6):063601, 2007.
- [83] Peisen S Huang, Qingying J Hu, and Fu-Pen Chiang. Double three-step phase-shifting algorithm. *Applied optics*, 41(22):4503–4509, 2002.
- [84] Chao Zuo, Shijie Feng, Lei Huang, Tianyang Tao, Wei Yin, and Qian Chen. Phase shifting algorithms for fringe projection profilometry: A review. *Optics and Lasers in Engineering*, 109:23–59, 2018.
- [85] Song Zhang. Absolute phase retrieval methods for digital fringe projection profilometry: A review. *Optics and Lasers in Engineering*, 107:28–37, 2018.
- [86] Chao Zuo, Lei Huang, Minliang Zhang, Qian Chen, and Anand Asundi. Temporal phase unwrapping algorithms for fringe projection profilometry: A comparative review. *Optics and lasers in engineering*, 85:84–103, 2016.
- [87] ZH Zhang. Review of single-shot 3d shape measurement by phase calculation-based fringe projection techniques. *Optics and Lasers in Engineering*, 50(8): 1097–1106, 2012.
- [88] Mikko Kytö, Mikko Nuutinen, and Pirkko Oittinen. Method for measuring stereo camera depth accuracy based on stereoscopic vision. In *Three-Dimensional Imaging, Interaction, and Measurement*, volume 7864, pages 168–176. SPIE, 2011.
- [89] David Gallup, Jan-Michael Frahm, Philippos Mordohai, and Marc Pollefeys. Variable baseline/resolution stereo. In *2008 IEEE conference on computer vision and pattern recognition*, pages 1–8. IEEE, 2008.
- [90] David J Brady. *Optical imaging and spectroscopy*. John Wiley & Sons, 2009.
- [91] Jing Xu and Song Zhang. Status, challenges, and future perspectives of fringe projection profilometry. *Optics and Lasers in Engineering*, 135:106193, 2020.
- [92] Antonio Muñoz, Jorge L Flores, Geliztle Parra-Escamilla, Luis A Morales, Sotero Ordones, and Manuel Servin. Least-squares gamma estimation in fringe projection profilometry. *Applied Optics*, 60(5):1137–1142, 2021.
- [93] Thang Hoang, Bing Pan, Dung Nguyen, and Zhaoyang Wang. Generic gamma correction for accuracy enhancement in fringe-projection profilometry. *Optics letters*, 35(12):1992–1994, 2010.

- [94] Zhengyou Zhang. A flexible new technique for camera calibration. *IEEE Transactions on pattern analysis and machine intelligence*, 22(11):1330–1334, 2000.
- [95] Huijie Zhao, Zhen Wang, Hongzhi Jiang, Yang Xu, and Chao Dong. Calibration for stereo vision system based on phase matching and bundle adjustment algorithm. *Optics and Lasers in Engineering*, 68:203–213, 2015.
- [96] Rongqian Yang, Sheng Cheng, Wei Yang, and Yazhu Chen. Robust and accurate surface measurement using structured light. *IEEE Transactions on Instrumentation and Measurement*, 57(6):1275–1280, 2008.
- [97] Torben Fetzer, Gerd Reis, and Didier Stricker. Fast projector-driven structured light matching in sub-pixel accuracy using bilinear interpolation assumption. In *International Conference on Computer Analysis of Images and Patterns*, pages 26–36. Springer, 2021.
- [98] Fuqiang Zhong, Ravi Kumar, and Chenggen Quan. A cost-effective single-shot structured light system for 3d shape measurement. *IEEE Sensors Journal*, 19(17):7335–7346, 2019.
- [99] Changzhi Yu, Fang Ji, Junpeng Xue, and Yajun Wang. Adaptive binocular fringe dynamic projection method for high dynamic range measurement. *Sensors*, 19(18):4023, 2019.
- [100] Daniel Moreno and Gabriel Taubin. Simple, accurate, and robust projector-camera calibration. In *2012 Second International Conference on 3D Imaging, Modeling, Processing, Visualization & Transmission*, pages 464–471. IEEE, 2012.
- [101] M Servin, JC Estrada, and J Antonio Quiroga. The general theory of phase shifting algorithms. *Optics express*, 17(24):21867–21881, 2009.
- [102] Yves Surrel. Design of algorithms for phase measurements by the use of phase stepping. *Applied optics*, 35(1):51–60, 1996.
- [103] Richard Hartley and Andrew Zisserman. *Multiple view geometry in computer vision*. Cambridge university press, 2003.
- [104] GOM. Atos 5: High-speed 3d scanning: For industrial demands. <https://www.gom.com/en/products/high-precision-3d-metrology/atos-5/>, 2022. Accessed 2022-10-14.
- [105] Paul J Besl and Neil D McKay. Method for registration of 3-d shapes. In *Sensor fusion IV: control paradigms and data structures*, volume 1611, pages 586–606. Spie, 1992.

- [106] Jing Wang, Banglei Guan, Yongsheng Han, Zhilong Su, Qifeng Yu, and Dongsheng Zhang. Sensor-aided calibration of relative extrinsic parameters for outdoor stereo vision systems. *Remote Sensing*, 15(5):1300, 2023.
- [107] Shogo Miyata, Hideo Saito, Kosuke Takahashi, Dan Mikami, Mariko Isogawa, and Akira Kojima. Extrinsic camera calibration without visible corresponding points using omnidirectional cameras. *IEEE Transactions on Circuits and Systems for Video Technology*, 28(9):2210–2219, 2017.
- [108] W Ellis, D Kim, J Hyatt, C Davila-Peralta, J Berkson, R Ball, B Jeong, R Pecha, N Julicher, I Pimienta, et al. Radio telescope manufacturing with adaptive aluminum thermoforming and fringe projection metrology. In *Astronomical Optics: Design, Manufacture, and Test of Space and Ground Systems IV*, volume 12677, pages 195–198. SPIE, 2023.
- [109] Alan EE Rogers, Richard Barvainis, PJ Charpentier, and Brian E Corey. Corrections for the effects of a radome on antenna surface measurements made by microwave holography. *IEEE transactions on antennas and propagation*, 41(1):77–84, 1993.
- [110] Mehdi S Zarghamee, Joseph Antebi, and Frank W Kan. Optimal surface adjustment of haystack antenna. *IEEE transactions on antennas and propagation*, 43(1):79–86, 1995.
- [111] Dirk IL de Villiers and Robert Lehmensiek. Performance estimates of the 18-meter ngvla reflector system with main reflector rim extension. In *2023 IEEE International Symposium on Antennas and Propagation and USNC-URSI Radio Science Meeting (USNC-URSI)*, pages 763–764. IEEE, 2023.
- [112] Luca Olmi. Large millimeter telescope project: overview and optical design. *Advanced Technology MMW, Radio, and Terahertz Telescopes*, 3357:186–197, 1998.
- [113] Philip R Jewell. The green bank telescope. *Radio Telescopes*, 4015:136–147, 2000.
- [114] Isak P Theron, Robert Lehmensiek, and Dirk IL de Villiers. The design of the meerkat dish optics. In *2012 International Conference on Electromagnetics in Advanced Applications*, pages 539–542. IEEE, 2012.
- [115] Eun-Hee Kim, Joonku Hahn, Hwi Kim, and ByoungHo Lee. Profilometry without phase unwrapping using multi-frequency and four-step phase-shift sinusoidal fringe projection. *Optics Express*, 17(10):7818–7830, 2009.

- [116] Minliang Zhang, Qian Chen, Tianyang Tao, Shijie Feng, Yan Hu, Hui Li, and Chao Zuo. Robust and efficient multi-frequency temporal phase unwrapping: optimal fringe frequency and pattern sequence selection. *Optics express*, 25(17):20381–20400, 2017.
- [117] Tim J Atherton and Darren J Kerbyson. Size invariant circle detection. *Image and Vision computing*, 17(11):795–803, 1999.
- [118] HK Yuen, John Princen, John Illingworth, and Josef Kittler. Comparative study of hough transform methods for circle finding. *Image and vision computing*, 8(1):71–77, 1990.
- [119] David H Parker and John M Payne. Active surface architectures of large radio telescopes. *Proceedings of the XXVIIth URSI General Assembly in Maastricht*, 2002.